

8-1-2016

Novel Pathways to High-Efficiency Chalcopyrite Photovoltaic Devices: A Spectroscopic Investigation of Alternative Buffer Layers and Alkali-Treated Absorbers

Michelle Mezher
University of Nevada, Las Vegas

Follow this and additional works at: <https://digitalscholarship.unlv.edu/thesesdissertations>

 Part of the [Chemistry Commons](#)

Repository Citation

Mezher, Michelle, "Novel Pathways to High-Efficiency Chalcopyrite Photovoltaic Devices: A Spectroscopic Investigation of Alternative Buffer Layers and Alkali-Treated Absorbers" (2016). *UNLV Theses, Dissertations, Professional Papers, and Capstones*. 2794.
<http://dx.doi.org/10.34917/9302951>

This Dissertation is protected by copyright and/or related rights. It has been brought to you by Digital Scholarship@UNLV with permission from the rights-holder(s). You are free to use this Dissertation in any way that is permitted by the copyright and related rights legislation that applies to your use. For other uses you need to obtain permission from the rights-holder(s) directly, unless additional rights are indicated by a Creative Commons license in the record and/or on the work itself.

This Dissertation has been accepted for inclusion in UNLV Theses, Dissertations, Professional Papers, and Capstones by an authorized administrator of Digital Scholarship@UNLV. For more information, please contact digitalscholarship@unlv.edu.

NOVEL PATHWAYS TO HIGH-EFFICIENCY CHALCOPYRITE PHOTOVOLTAIC
DEVICES: A SPECTROSCOPIC INVESTIGATION OF ALTERNATIVE BUFFER
LAYERS AND ALKALI-TREATED ABSORBERS

By

Michelle Mezher

Bachelor of Arts – Chemistry (ACS Accredited)
University of San Diego
2012

A dissertation submitted in partial fulfillment of
the requirements for the

Doctor of Philosophy – Chemistry

Department of Chemistry and Biochemistry
College of Sciences
The Graduate College

University of Nevada, Las Vegas
August 2016

Copyright 2016 by Michelle Mezher

All Rights Reserved



Dissertation Approval

The Graduate College
The University of Nevada, Las Vegas

June 3, 2016

This dissertation prepared by

Michelle Mezher

entitled

Novel Pathways to High-Efficiency Chalcopyrite Photovoltaic Devices: A Spectroscopic Investigation of Alternative Buffer Layers and Alkali-Treated Absorbers

is approved in partial fulfillment of the requirements for the degree of

Doctor of Philosophy – Chemistry
Department of Chemistry and Biochemistry

Clemens Heske, Ph.D.
Examination Committee Chair

Kathryn Hausbeck Korgan, Ph.D.
Graduate College Interim Dean

Kathleen Robins, Ph.D.
Examination Committee Member

David Hatchett, Ph.D.
Examination Committee Member

Shubhra Bansal, Ph.D.
Graduate College Faculty Representative

ABSTRACT

Novel Pathways to High-Efficiency Chalcopyrite Photovoltaic Devices:
A Spectroscopic Investigation of Alternative Buffer Layers and Alkali-treated Absorbers

By
Michelle Mezher

Dr. Clemens Heske, Examination Committee Chair
Professor of Chemistry
University of Nevada, Las Vegas

Within the past few years, breakthroughs in Cu(In,Ga)Se_2 (CIGSe) thin-film photovoltaic device efficiencies (on a laboratory scale) were achieved utilizing alkali-treated (KF) absorbers. Na incorporation in the CIGSe absorber, either diffused from the substrate or deliberately deposited, affects the surface electronic properties of the CIGSe absorber. The role of Na, however, is still not fully understood with some studies suggesting that Na also passivates defects at the grain boundaries. Replacing Na with K offered an efficiency boost resulting in KF treatments becoming the new “hot topic” in the chalcopyrite field, both in terms of understanding how the treatment changes the absorber along with studying the differences between alternative KF deposition methods. To provide insight on these issues, x-ray (XPS) and ultraviolet (UPS) photoelectron spectroscopy, inverse photoemission spectroscopy (IPES), as well as x-ray emission spectroscopy (XES) are utilized to investigate two sample sets. The first set (Chapter 4) compares the effects of both KF and NaF treatments on absorbers taken from the production line of STION and the National Renewable Energy Laboratory. The purpose here is to compare how similar alkali-treatments affect chalcopyrite devices from different sources along with comparing

the alkali-treatments themselves. The second sample set (Chapter 5) investigates effects of KF treatments when incorporated utilizing different deposition techniques.

The most recent world record efficiency for CIGSe thin-film devices was not achieved with the KF-treatment, but with the replacement of the traditional CdS buffer layer (between the absorber and transparent front electrode) with Zn(O,S), a material offering the possibility of increasing the current collection in the shorter wavelength region of the solar spectrum. To further optimize these photovoltaic devices, an understanding of the interactions between the absorber and the buffer layer is crucial. For example, record CdS/CIGSe devices have a flat conduction band alignment at the buffer/absorber interface, while, in contrast, the less efficient CdS/Cu(In,Ga)S₂ device exhibits a cliff-like conduction band offset, impeding electron transport. Thus, a determination of the conduction band offset is, among other aspects, of significant importance.

When using Zn(O,S) as the buffer layer, it should be noted that the bandgap of a Zn(O,S) alloy exhibits a strong bowing effect as the O:S ratio varies. With the ability to change the O:S ratio and alter the bandgap, it is thus important to understand the chemical and electronic structure of the Zn(O,S)/CIGSe interface in high-efficiency devices through *direct* and *independent* analysis of the heterojunction formation, the valence band, and the conduction band. This is the first non-destructive analysis of the interface using XPS, UPS, IPES, and XES investigating samples with varying buffer layer thickness. A comprehensive and all-experimental depiction of the electronic level alignment (Chapter 6) and chemical interactions (Chapter 7) at the interface will be presented.

ACKNOWLEDGEMENTS

First and foremost, I would like to thank my advisor and mentor, Dr. Clemens Heske. I will always be extremely grateful that you have provided me with the amazing opportunity of pursuing a deeper knowledge in chemistry/physics and spectroscopy. You have been patient and kind and instilled within me the drive to always understand why and not take things at face-value. You have taught me to articulate my thoughts more clearly and guided me to become a better scientist throughout my graduate years. Thank you.

Drs. Lothar Weinhardt, Moni Blum, and Marcus Bär – I am very thankful for the guidance and lessons you have offered me at the beamline, through e-mail, and in the labs at UNLV and HZB. I count myself lucky to have been taught by scientists top in their field.

Drs. Kim Horsley and Doug Duncan – Your friendships both inside and outside the lab have really made living in Vegas better after moving away from everyone I knew. From our gif conversations, rock climbing adventures, and love of ayce sushi, these friendships will have a lasting impact on my life. I look forward to you guys moving to San Diego ;).

I will always be grateful for past and present group members that have shared in the love/hate relationship of lab maintenance and providing valuable friendships and memorable discussions – Drs. Timo Hofmann, Samantha Rosenberg, Dirk Hauschild, Manuela Wallesch, and Kyle Bowen; Lynette Kogler, James Carter, Kyle Aleshire, Chase Aldridge, Ryan Bugni, and Sarah Alexander.

Dr. Moni Blum, Dr. Dagmar Kreikemeyer-Lorenzo, and Andi Benkert – Beamtime buddies! I will miss our night-shift yoga sessions at the beamline, learning “the cup song”, pitch perfect, and all of our fun adventures together!

Drs. Regan Wilks, David Starr, and Jan Alsmeier, Evelyn Handick, and Leo Köhler – You guys have made my time and experience in Berlin so much fun. Thank you for helping me with the process of moving to Berlin, showing me the culture, teaching me in lab, and accepting me as part of the Bär group. Regan – I’m waiting for the next time we hang out and drink some delicious beer! Dublin would be a good place ☺.

I’m thankful for collaborators on the F-PACE project, Dr. Kannan Ramanathan, Dr. Lorelle Mansfield, Dr. Rebekah Garriss, and Dr. Chris Muzzillo, that have provided me with fun samples to measure and their guidance throughout the project and during HOPE.

I’m thankful for Eric Knight and all his help keeping the lab running, Wanli Yang for maintaining the beamline, Mark Miyamoto and Debbie Masters for your skills and helping me with all the fun administrative tasks, and of course my committee (past and present), Dr. Kathy Robins, Dr. David Hatchett, Dr. Rama Venkat, Dr. Shubhra Bansal, and Dr. Dennis Lindle for putting in your time and offering your guidance throughout my graduate years.

My family, Mom and Dad – I can never put into words how much I appreciate all the hard work and sacrifices you have made to make sure Andrew and I received a good education. You have lived your lives always setting good examples for Andrew and myself. Thank you for all your support. Andrew – Our competitive streak of always needing to outdo each other academically has led to this exact moment: Look at me. I’m the real doctor now.

Jeff George (“Professional Scientist”) – For the past four years you have been a constant support in all aspects of my life. Thank you for always being the optimism to my pessimism and encouraging me to be my best.

My aerial family at SHINE and PFS, thank you for keeping me sane and providing valuable and memorable friendships. In addition, thank you for making sure I didn't fall and die when suspended in the air or playing on the apparatuses. I think that's also important 😊.

Last, but definitely not least, my favorite furry companion, Raja – Meow.

No man can reveal to you aught but that which already lies half asleep in the dawning of your knowledge.

The teacher who walks in the shadow of the temple, among his followers, gives not of his wisdom but rather of his faith and his lovingness.

If he is indeed wise he does not bid you enter the house of his wisdom, but rather leads you to the threshold of your own mind.

— Kahlil Gibran, *The Prophet*

DEDICATION

In memory of Dennis Lindle, Jiddo Khalil, Khalo Zouzou, and Charles Ghawi

For my family in Lebanon

TABLE OF CONTENTS

ABSTRACT	iii
ACKNOWLEDGEMENTS	v
DEDICATION	vii
LIST OF TABLES	x
LIST OF FIGURES	xi
CHAPTER 1 INTRODUCTION	1
 CHAPTER 2 STRUCTURE OF THE CIGSe THIN-FILM SOLAR CELL	
2.1 Formation of a p-n Junction.....	5
2.2 CIGSe Substrate and Absorber Structure	6
2.2.1 CIGSe substrate and back-contact	6
2.2.2 CIGSe absorber	8
2.2.3 Alkali-incorporation in CIGSe	10
2.3 Buffer Layers.....	12
2.3.1 CdS	12
2.3.2 Zn(O,OH,S)	12
2.3.3 Electronic band-alignments	14
2.4 Window Layers.....	16
 CHAPTER 3 SPECTROSCOPIC TECHNIQUES	
3.1 Introduction	18
3.2 Lab-based Spectroscopies	19
3.2.1 X-ray Photoelectron Spectroscopy (XPS)	19
3.2.2 X-ray-excited Auger Electron Spectroscopy (AES)	21
3.2.3 Ultra-violet Photoelectron Spectroscopy (UPS)	21
3.2.4 Inverse Photoemission Spectroscopy (IPES)	23
3.2.5 Combining UPS and IPES	23
3.2.6 Surface Sensitivity	24
3.2.7 Peak Fitting	26
3.3 Sample Preparation and Measurement Parameters	27
3.4 Synchrotron-Based Soft X-ray Spectroscopy	31
3.4.1 X-ray Emission (XES)	31
3.4.2 Beamline Description	33
 CHAPTER 4 CHEMICAL AND ELECTRONIC SURFACE PROPERTIES OF ALKALI-TREATED CIG(S)Se ABSORBERS: COMPARISON OF INDUSTRY (STION) TO NATIONAL LAB (NREL) ABSORBERS	

	4.1 Introduction	35
	4.2 Experimental Details	36
	4.3 Results and Discussion	38
	4.4 Conclusion	61
CHAPTER 5	KF COEVAPORATION VS. KF POST DEPOSITION TREATMENT: SPECTROSCOPIC INVESTIGATION ON THE EFFECTS OF KF FOLLOWING DIFFERENT DEPOSITION PROCESSES	
	5.1 Introduction	63
	5.2 Experimental Details	63
	5.3 Results and Discussion	65
	5.4 Conclusion	93
CHAPTER 6	ELECTRONIC STRUCTURE OF THE Zn(O,S)/CIGSe INTERFACE	
	6.1 Introduction	95
	6.2 Experimental Details	96
	6.3 Results and Discussion	98
	6.4 Conclusion	105
CHAPTER 7	SOFT X-RAY SPECTROSCOPY OF A COMPLEX HETEROJUNCTION IN HIGH-EFFICIENCY THIN-FILM PHOTOVOLTAICS: INTERMIXING AND Zn SPECIATION AT THE Zn(O,S)/CIGSe INTERFACE	
	7.1 Introduction	106
	7.2 Experimental Details	107
	7.3 Results and Discussion	108
	7.4 Conclusion	123
CHAPTER 8	SUMMARY	124
APPENDIX	LIST OF ABBREVIATIONS AND SYMBOLS	127
REFERENCES		129
CURRICULUM VITAE		141

LIST OF TABLES

Table 1:	Core level peak positions of the bare absorber, the thin (5 min) Zn(O,S)/CIGSe sample, and the thick (22.5 min) Zn(O,S)/CIGSe sample, as well as their relative shifts	102
----------	--	-----

LIST OF FIGURES

Figure 2.1:	Schematic of the band alignment p-n junction diagram and semiconductor to metal interface.	5
Figure 2.2:	SEM cross-section of a typical CIGSe solar cell fabricated at NREL. Ref. from 8.....	7
Figure 2.3:	Metal flux schematic for the three-stage coevaporation process. Taken from ref. 19.	8
Figure 2.4:	Schematics of various Na-treated CIGSe absorbers including a) diffusion from the soda-lime glass, b) Na barrier and NaF precursor, c) NaF coevaporated with CIGSe, and d) NaF PDT.	11
Figure 2.5:	Optical bandgap as a function of O:S ratio in a Zn(O,S) alloy. Taken from ref. 57	13
Figure 2.6:	Schematic of several band alignment scenarios a) flat b) spike or c) cliff configuration for the conduction band offset.	15
Figure 2.7:	Example of a CIGSe minimodule deposited onto a flexible substrate from EMPA. Ref. from 75.....	16
Figure 3.1:	Schematic of a) x-ray photoelectron spectroscopy (XPS) and b) x-ray Auger electron spectroscopy (XAES) transitions.....	20
Figure 3.2:	Schematic of a) ultra-violet photoelectron spectroscopy (UPS) and b) inverse photoemission spectroscopy (IPES) transitions.	22
Figure 3.3:	The “Universal Curve” (line that averages the experimental data points) presents the relationship of the inelastic mean free path of electrons as a function of their kinetic energy relative to vacuum level. Adapted from reference ⁸⁸	25
Figure 3.4:	Mg K α survey spectra of the Cu(In _{0.7} ,Ga _{0.3})Se ₂ absorber as a function of treatment time during a low-energy ion cleaning series. Spectra in the blue box are shown on an enlarged energy axis in Fig. 3.5.....	28

Figures 3.5:	XPS spectra of the low binding energy region before and after two low-energy ion treatment steps.	29
Figure 3.6:	UPS and IPES spectra showing the band gap edge positions (VBM and CBM) as well as the electronic surface bandgap of the CIGSe absorber as a function of treatment time	30
Figure 3.7:	Schematic of x-ray emission spectroscopy (XES) transitions. The “zero” step of the process is colored gray while the XES process is in red.....	31
Figure 3.8:	The fluorescence and Auger yields for the K subshell as a function of Atomic number. Ref. from 97, 98	32
Figure 3.9:	Schematic of Beamline 8.0.1 at the Advanced Light Source. Taken from ref. 99	34
Figure 4.1:	XPS survey spectra normalized to the $\text{In}_{5/2}$ peak area of the NREL and STION bare absorbers (black), both NaF-treated absorbers (red), both low efficiency KF-treated absorbers (blue), and both high efficiency KF-treated absorbers (pink).....	38
Figure 4.2:	XPS detailed spectra of the $\text{Cu } 2p_{3/2}$ peak normalized to the $\text{In}_{5/2}$ peak area (left) and to $\text{Cu } 2p_{3/2}$ peak height (right) of the NREL and STION bare absorbers (black), NaF-treated absorbers (red), and low and high efficiency KF-treated absorbers (blue, pink).	40
Figure 4.3:	XPS detailed spectra of the $\text{Ga } 2p_{3/2}$ peak normalized to the $\text{In}_{5/2}$ peak area (left) and to $\text{Ga } 2p_{3/2}$ peak height (right) of the NREL and STION bare absorbers (black), NaF-treated absorbers (red), and low and high efficiency KF-treated absorbers (blue, pink).	41
Figure 4.4:	XPS detailed spectra of the Ga LMM Auger peak normalized to the $\text{In } 3d_{5/2}$ peak area (left) and to Ga LMM peak height (right) of the NREL and STION bare absorbers (black), NaF-treated absorbers (red), and low and high efficiency KF-treated absorbers (blue, pink).	42
Figure 4.5:	XPS detailed spectra of the Ga 3d / In 4d region of the NREL bare absorber (top left), NaF-treated absorber (top right), and low and high efficiency KF-treated absorbers (bottom left and right).....	44

Figure 4.6:	XPS detailed spectra of the Ga 3d / In 4d region of the STION bare absorber (top left), NaF-treated absorber (top right), and low and high efficiency KF-treated absorbers (bottom left and right).....	45
Figure 4.7:	XPS detailed spectra of the Se 3d peak normalized to the In 3d _{5/2} peak area (left) and to Se 3s peak height (right) of the NREL and STION bare absorbers (black), NaF-treated absorbers (red), and low and high efficiency KF-treated absorbers (blue, pink). The S 2s peak intensity for the STION absorbers changes as a function of alkali-treatment.....	47
Figure 4.8:	XPS detailed spectra of the In 3d _{5/2} peak (left) and the In MNN (right) normalized to peak height of the NREL and STION bare absorbers (black), NaF-treated absorbers (red), and low and high efficiency KF-treated absorbers (blue, pink).	48
Figure 4.9:	XPS detailed spectra of the K 2p peak (left). A closer look at the K 2p for the NREL absorbers is shown at the right along with K references.	49
Figure 4.10:	XPS detailed spectra of the Na 1s (left) and O 1s peaks (right) normalized to the In _{5/2} peak area of the NREL and STION bare absorbers (black), NaF-treated absorbers (red), and low and high efficiency KF-treated absorbers (blue, pink).....	50
Figure 4.11:	Modified Auger Parameter plot of Na 1s and Na KLL. The ion treated data are shown in red with references (111,112) in black.....	52
Figure 4.12:	XPS detailed spectra of the F 1s (left) and F KLL (right) peaks of the NREL and STION bare absorbers (black), NaF-treated absorbers (red), and low and high efficiency KF-treated absorbers (blue, pink).....	53
Figure 4.13:	XPS spectra of the Zn 2p peaks for the NREL (left) and STION (right) bare absorbers (black), NaF-treated absorbers (red), and low and high efficiency KF-treated absorbers (blue, pink).	54
Figure 4.14:	UPS spectra taken with He II excitation of the NREL and STION bare absorbers (black), NaF-treated absorbers (red), and low and high efficiency KF-treated absorbers (blue, pink).	56
Figure 4.15:	XES emission spectra excited nonresonantly with 180 eV of the S L _{2,3} region for the STION bare (black), NaF-treated (red), and low and high	

efficiency KF-treated absorbers (blue, pink). Reference spectra are provided for comparison.	58
Figure 4.16: Relative weights of the STION bare absorber spectrum was subtracted from the alkali-treated absorber spectra and the resulting residuals are presented with reference spectra. Multiplication factors shown.	59
Figure 4.17: XES emission spectra of the K $L_{2,3}$ (left) and F K_{α} of the NREL and STION bare absorbers (black), NaF-treated absorbers (red), and low and high efficiency KF-treated absorbers (blue, pink).	60
Figure 5.1: XPS Mg K_{α} survey spectrum taken of the NREL bare and KF-treated absorbers. The ion-treated surfaces are shown in black, while the rinsed surfaces are shown in red.....	65
Figure 5.2: Detailed XPS Mg K_{α} spectra of the Cu $2p_{3/2}$ taken on the ion-treated (center) and NH_4OH treated (top) of the CKIGSe, both CIGSe, and both KF PDT absorbers. This is compared to a previous sample set, displayed on the bottom (four alkali-treated NREL absorbers, grown with the three-stage coevaporation process).....	66
Figure 5.3: Detailed XPS Mg K_{α} spectra of the Se 3d region, normalized by In $3d_{5/2}$ area (left) and peak height (right). The ion-treated spectra are shown at the bottom, and the NH_4OH treated spectra at the top. The expected locations for oxide contributions are indicated.	67
Figure 5.4: Detailed XPS Mg K_{α} spectra of the In $3d_{5/2}$ (left) and In MNN (right) regions, normalized by peak height. The ion-treated spectra are shown at the bottom, while the NH_4OH -treated spectra are at the top. The expected locations for oxide, selenide, and fluoride contributions are indicated. ..	68
Figure 5.5: Detailed XPS Mg K_{α} spectra In MNN region, normalized by peak height, for the clean and rinsed KF PDT absorbers. Three In-Se references are used to fit the peaks to show contributions from In-F, In-O, and In-Se species. The residual is shown on the bottom in purple.....	69
Figure 5.6: Detailed XPS Mg K_{α} spectra of the Ga $2p_{3/2}$ (left) and Ga LMM (right) regions, normalized by the In $3d_{5/2}$ area. The ion-treated spectra are shown at the bottom, while the NH_4OH -treated spectra are at the top. The expected locations for oxide, selenide, and fluoride contributions are indicated ...	71

- Figure 5.7: Detailed XPS Mg K_{α} spectra of the Ga 3d and In 4d region. The dotted spectra represent NH_4OH treated absorbers while the continuous line spectra represent the “clean” surfaces. Regions where Ga 3d and In 4d peaks are located are boxed..... 72
- Figure 5.8: XPS detail spectra of the Ga 3d/In 4d of the pre and post-rinse CIGSe absorber (top) and CIGSe/ SiO_2 (bottom). Fit curves for In:Ga contributions to the peak are shown along with their respective residuals (purple)..... 73
- Figure 5.9: XPS detail spectra of the Ga 3d/In 4d region of the CKIGSe absorber pre-rinse (left) and post-rinse (right). Fit curves for In:Ga contributions to the peak are shown along with their respective residuals (purple)..... 74
- Figure 5.10: XPS detail spectra of the Ga 3d/In 4d region of the pre and post-rinse KF PDT absorber (top) and KF PDT/ SiO_2 (bottom). Fit curves for In:Ga contributions to the peak are shown along with their respective residuals (purple) 76
- Figure 5.11: XPS detail spectra of the Ga 3d/In 4d region of the pre-rinse KF PDT absorber as a function of fit curves to show the process of determining a good fit. Fit curves for In:Ga (In 4d $_{5/2}$, In 4d $_{3/2}$, Ga 3d $_{5/2}$, Ga 3d $_{3/2}$) contributions to the peak are shown along with their respective residuals (purple). 78
- Figure 5.12: Detailed XPS Mg K_{α} spectra of the F 1s region, normalized by the In 3d $_{5/2}$ area. The ion-treated spectra are shown at the bottom, while the NH_4OH -treated spectra are at the top (left). The right graph is scaled to see the F 1s peaks of the NH_4OH treated absorbers (only). The expected locations for InF_3 , NaF, KF, and CF_3 contributions are indicated..... 80
- Figure 5.13: Detailed XPS Mg K_{α} spectra of the C 1s and K 2p region, normalized by the In 3d $_{5/2}$ area (left). The ion-treated spectra are shown at the bottom, while the NH_4OH -treated spectra are at the top (left). The right graph is magnified to show the K 2p peaks of the NH_4OH and ion-treated absorbers. The expected locations for Ga LMM, KF, and metallic K (K_{met}) are indicated..81
- Figure 5.14: Detailed XPS Mg K_{α} spectra of the Na 1s region, normalized by the In 3d $_{5/2}$ area. The ion-treated spectra are shown at the bottom, while the NH_4OH -treated spectra are at the top (left). The right graph is scaled to show the

Na 1s peaks of the NH_4OH -treated absorbers (only). A line was drawn to help guide the eye. On the left, the expected locations for NaF and NaO contributions are indicated. 83

Figure 5.15: Modified Auger Parameter plot of Na 1s and Na KLL. The ion-treated data are shown in red, NH_4OH treated data in blue, and references (111,112) in black. 85

Figure 5.16: Detailed XPS Mg K_α spectra of the O 1s region, normalized by the In $3d_{5/2}$ area (left) and O 1s peak height (right). The ion-treated spectra are shown at the bottom, while the NH_4OH -treated spectra are at the top. The expected locations for water, hydroxide, metal oxides, and carbonates are indicated 86

Figure 5.17: XPS detail spectra of the O 1s peak and fit (components in black, sum in red) of the pre and post-rinsed CIGSe (top) and CIGSe/ SiO_2 samples (bottom). 87

Figure 5.18: XPS detail spectra of the O 1s peak and fit (components in black, sum in red) of the pre and post-rinsed KF PDT (top) and KF PDT/ SiO_2 samples (bottom).. 88

Figure 5.19: XPS detail spectra of the O 1s peak and fit (components in black, sum in red) of the pre and post-rinsed CKIGSe sample. 89

Figure 5.20: UPS (He II) and IPES spectra of all absorbers. A Savitzky-Golay smooth line is used as a guide to the eye..... 90

Figure 5.21: UPS (He II) and IPES spectra of all absorbers. The ion-treated surfaces are shown in black, while the rinsed surfaces are shown in red..... 92

Figure 6.1: XPS detail spectra of the O 1s peak and fit (components in black, sum in red) of a) the thin (5 min) and b) the thick (22.5 min) $\text{Zn}(\text{O,S})/\text{CIGSe}$ samples. The magnified residual of each fit is also shown. 99

Figure 6.2: He I UPS (left) and IPES (right) spectra of the bare CIGSe absorber (bottom) and the thick $\text{Zn}(\text{O,S})/\text{CIGSe}$ sample (top). VBM and CBM values determined by linear extrapolations of the leading edges (red lines) are shown, together with the resulting electronic surface band gaps. Error bars are ± 0.10 and ± 0.15 eV for the VBM and CBM determination, respectively.

	A Savitzky-Golay-smoothed line is shown for the IPES spectra as a guide to the eye.	100
Figure 6.3:	Band alignment scheme of the Zn(O,S)/CIGSe interface. The band edge positions at the CIGSe and Zn(O,S) surfaces are shown on the left and right, respectively. In the center, the band alignment at the interface is shown, taking interface-induced band bending changes at the absorber surfaces and band bending in the buffer layer into account (as indicated by the ovals).	104
Figure 7.1:	XPS survey spectra of the untreated (black) and ion treated (red) Zn(O,S)/CIGSe sample series: CIGSe bare absorber (bottom), 5 min Zn(O,S) (middle), and 22.5 min Zn(O,S) (top).	109
Figure 7.2:	Modified Auger Parameter plot of Na 1s is shown before (red dot) and after different 50 eV Ar ⁺ -ion energy treatment steps (red triangles) in comparison to references (111,112) in black (error bars are ± 0.05 eV on both axes).	110
Figure 7.3:	Mg K α XPS spectra of the Se 3d peak (left) and the Ga 3d/In 4d region (right) for the CIGSe bare absorber and Zn(O,S)/CIGSe samples of varying thickness. To describe the 10 and 22.5 min spectra, the result of a fit with the CIGSe lineshape and a linear background is shown. Multiplication factors are shown in parentheses.	112
Figure 7.4:	Effective Zn(O,S) layer thickness derived from Se 3d (blue), Ga 3d (red, 5 min), In 4d (green, 5 min), Ga 3d/In 4d combined (pink, 10 min) and nominal thickness (black) as a function of Zn(O,S) CBD time. The 10 min nominal thickness and Ga 3d/In 4d data were shifted slightly to differentiate between the data points	114
Figure 7.5:	XPS detail spectra of the Ga 3d/In 4d region of the CIGSe absorber (bottom) and 5 min Zn(O,S) (top). Fit curves for In:Ga contributions to the peak are shown along with their respective residuals (purple).	115
Figure 7.6:	(Left) XPS spectra of the 22.5 min Zn(O,S) O 1s peak as a function of ion treatment time. (Right) Fits of the O 1s peak show a change in OH/OH+O ratio as a function of ion treatment.....	117

Figure 7.7:	XPS spectra of the Zn 2p _{3/2} peak (left) and S 2p/Se 3p peak (right) for the 5 and 22.5 min Zn(O,S) samples. Reference peak positions (111,112) are indicated above both peak.....	119
Figure 7.8:	(Left) S L _{2,3} and Se M _{2,3} emission of the Zn(O,S)/ClGSe interface as a function of CBD time and a ZnS reference. Multiplication factors shown in parenthesis	121
Figure 7.9:	a) Difference spectra from subtracting the 22.5 min Zn(O,S) S L _{2,3} emission from the 5 min (red) and 10 min(blue) spectra. b) Reference spectra for comparison	122

CHAPTER 1

INTRODUCTION

In 1954, the commercial solar age began with the realization that Si semiconductors exhibited photoelectric properties, leading to the development of a Si solar cell with a 6% energy conversion ¹. Over the next 60 years, continued improvements in device performance have resulted in crystalline and multi-crystalline single-junction Si photovoltaics (PV) achieving 25.6% (± 0.5) and 20.8% (± 0.5) efficiencies on a laboratory scale, respectively ². During the 1970's and 1980's, it was shown that in addition to Si, thin-film chalcogens demonstrated conversion efficiencies over 10% proving that high efficiency photovoltaic devices did not need to be Si based, but instead consist of two semiconductor layers with minimal lattice mismatch, suitable conductivity, and minimal interfacial energy barriers ³. Overtime, these devices have surpassed the efficiency of multi-crystalline Si-based devices with CdTe at 21.5% (± 0.4), and Cu(In,Ga)Se₂ (CIGSe) at 22.3% on a laboratory scale, which, however, is still well below their theoretical maximum efficiency ^{2,4}. In 1961, William Shockley and Hans J. Queisser formulated an upper theoretical limit for the conversion efficiency of a single p-n junction solar cell called, surprisingly, the Shockley-Queisser limit ⁵. By considering blackbody radiation, radiative recombination, and spectrum losses, they calculated that a single-junction solar cell (with a band-gap around 1.1 eV) has a theoretical maximum efficiency of 30% ⁵. If the device were to have a tandem structure of multiple cells, the efficiencies can surpass the Shockley-Queisser limit, with a three-junction tandem cell exhibiting a theoretical efficiency of 63% with the highest light concentration ⁶. Improving the efficiency of a

single-junction solar cell will thus in turn improve more complex photovoltaic-based technologies.

Not only do CdTe and CIGSe solar cells have room for improvement, but there is also a large disparity between lab-based cells and industry-manufactured full-scaled modules. For example, the record CIGSe module, held by MiaSole, is 15.7% (± 0.5), only about half the theoretical maximum efficiency of a single-junction CIGSe solar cell ^{2,5}. In addition to conversion efficiency, the cost of production is very important, as the only way solar energy will be competitive in the market is if it is affordable. While crystalline and multi-crystalline Si are high in module efficiency (22.9% and 18.5% respectively), they are very expensive to manufacture prompting a cheaper option, amorphous Si (a-Si), to dominate the solar market despite a low module efficiency of 12.3% (± 0.3) ². In order to make CIGSe and CdTe more competitive in the solar market, cheaper deposition methods and higher module efficiency is imperative.

In this dissertation, the impact of novel deposition parameters on both industry-manufactured and lab-based $\text{Cu}(\text{In,Ga})(\text{S,Se})_2$ (CIGSSe) and CIGSe are investigated in order to offer understanding on their impact to the chemical and electronic properties of the absorber surface/interfaces and give insight to their effect on the cell efficiency. Industry samples are from the STION production line while lab-based samples are from the National Renewable Energy Lab (NREL) in Golden, CO. This chapter, Chapter 1, gives a brief introduction and motivation for this research as well as an outline for the organization of the dissertation. Chapter 2 discusses photovoltaics and how they operate in-depth with relevant background information on thin-film CIGSe photovoltaics. Chapter

3 discusses the methods used to analyze the surface and interfaces of the CIGSe samples in order to provide a better understanding of the data analysis.

With K incorporated CIGSe devices being the “hot” topic, chapters four and five investigate the effects of alkali-treatments on chalcopyrite absorbers. Chapter four focuses on the chemical and electronic surface properties of NaF and KF treated CIG(S)Se absorbers with a focus on comparing industry grade absorbers and laboratory deposited absorbers. XPS is used to analyze changes in chemical states and how NaF and KF alter the surface. UPS gives insight to how the valence band maximum (VBM) changes with the alkali-treatments. XES offers a more bulk sensitive chemical view of the treated absorbers. Different alkali-treatments result in devices with very different conversion efficiencies.

Chapter 5 focuses on different deposition techniques of KF onto the CIGSe. A KF post deposition treatment is compared to KF that is co-evaporated while the CIGSe absorber is grown. Because the samples are rinsed before the buffer layer is deposited, the unrinsed and rinsed surfaces of these samples are compared to see how an ammonia treatment alters the surface. XPS studies and XES study the chemical changes between the samples (both rinsed and unrinsed) while UPS and IPES are used to study electronic structure differences. The different KF deposition techniques result in different conversion efficiencies of completed twin samples.

Another “hot” topic for chalcopyrites is the use of more-transparent alternative buffer layers to CdS. Chapters 6 and 7 investigate the electronic and chemical properties of Zn(O,S), the new alternative buffer layer that lead to the new CIGSSe world efficiency record of 22.3%⁴. XPS and XES are used to look at the chemical interactions at the

Zn(O,S)/CIGSe interface while XPS, UPS, and IPES are used to probe the electronic structure of the buffer/absorber interface. These findings are compared to the standard high efficiency CdS/CIGSe system. The dissertation is then brought to a close with a summary of the work in Chapter 8.

CHAPTER TWO

STRUCTURE OF THE CIGSe THIN-FILM SOLAR CELL

The following chapter provides an overview of the traditional p-n junction in solar cells and the structure and characteristics of CIGSe thin-film photovoltaics. Some of the deposition information was received from Lorelle Mansfield and Rebekah Garriss during the HOPE (Hands-On Photovoltaics Experience) workshop at NREL while creating a standard high-efficiency (18.5%) CIGSe device. Their contributions to this work are gratefully acknowledged.

2.1 – FORMATION OF A TRADITIONAL p-n JUNCTION

Photovoltaic devices convert the sun's energy into electricity by relying on the photoelectric effect, which describes the ability of matter to eject electrons when it is excited by photons. Photons, fundamental particles of light, are absorbed in the semiconductor material when their energy, $h\nu$, is equal to or greater than the energy of the bandgap, resulting in the creation of electron-hole pairs. If the photon does not have

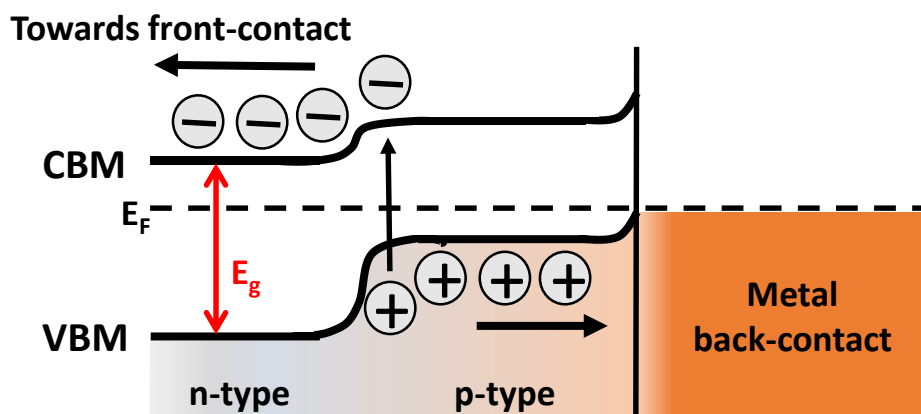


Figure 2.1: Schematic of the band alignment p-n junction diagram and semiconductor to metal interface.

enough energy, it would simply pass through the photovoltaic material as if it were transparent. In order to prevent the recombination of the electron-hole pairs, a built-in electric field in the solar cell is imperative. To create this electric field, a p-n junction is formed by contacting a material with holes as the majority carrier (p-type) to a material with electrons as the majority carrier (n-type), as seen in Figure 2.1. The p-n junction displayed in the figure is at equilibrium, represented by a flat E_F (Fermi energy) spanning the materials. E_F is the statistical average of occupied and unoccupied states and thus, for an n-type semiconductor E_F lies in the bandgap (E_g) closer to the conduction band minimum (CBM) while for a p-type semiconductor, E_F lies closer to the valence band maximum (VBM). A depletion region forms at the junction due to space charge buildup causing band-bending to occur⁷. An electric field, acting as a diode, separates the p-type and n-type region, allowing electrons to flow towards the front-contact and the holes to flow toward the back-contact. Attaching metal conductors to the p-type and n-type materials (front-contact and back-contact) allows an electrical circuit to form after attaching a load, thus capturing the electrons (electric current) and providing electricity to power the load.

2.2 – CIGSe SUBSTRATE AND ABSORBER STRUCTURE

2.2.1 – Substrate and back-contact

The majority of CIGSe solar cells are fabricated to incorporate the same basic structure represented by the Scanning Electron Microscopy (SEM) cross-section of the device in Figure 2.2⁸. The substrate of CIGSe is typically glass, however flexible substrates (eg. stainless steel, polyimide) rose in popularity due to the production of flexible modules and the feasibility of roll-to-roll processing^{9–11}. The substrate is coated with a Mo layer,

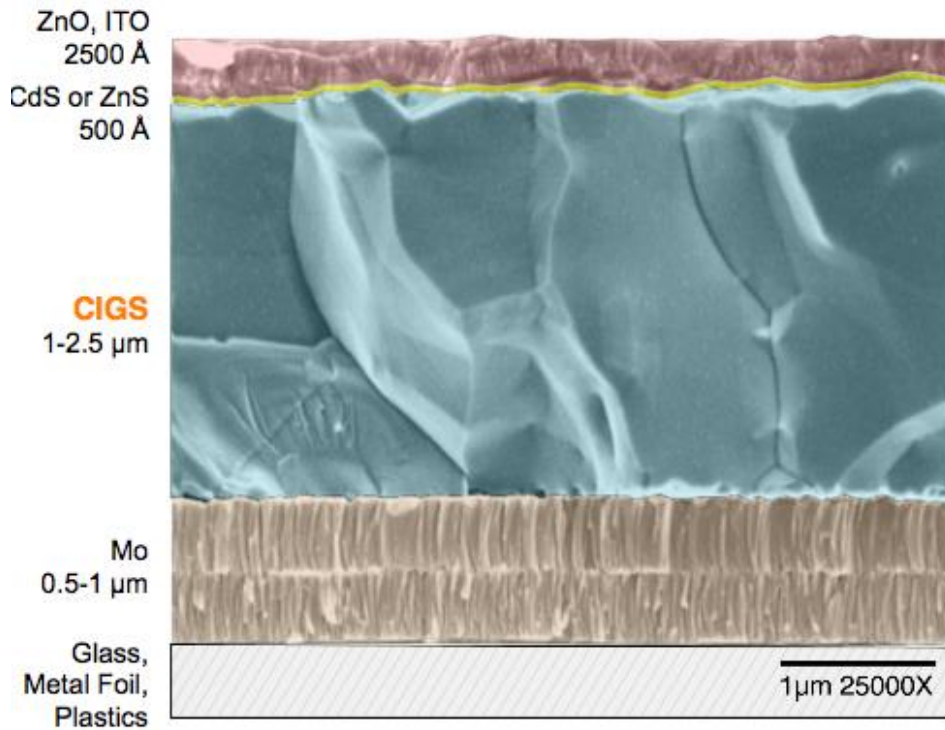


Figure 2.2: SEM cross-section of a typical CIGSe solar cell fabricated at NREL. Ref. from 8.

typically of a thickness between 0.5 and 1 μm, providing the solar cell structure with a back-contact. Ideally, an ohmic contact (the unimpeded transfer of electrons from one material to another) at the Mo/CIGSe interface is formed, contrasting a Schottky barrier, which exhibits resistive losses. In reality, MoSe₂ forms at the Mo/CIGSe interface^{12–14} and experimental data suggests that the n-type MoSe₂ forms the direct contact to the Mo metal (instead of CIGSe) causing an upward band bending to occur at that interface (shown in Figure 2.1) due to a Schottky-like contact¹⁵. In turn, the upward band bending creates an electron back-reflector, reducing recombination at the Mo/CIGSe interface^{15–}

2.2.2 – CIGSe absorber

A wide variety of deposition techniques is utilized to grow the CIGSe absorber. The most successful deposition method for research-scale solar cells is the three-stage coevaporation process¹⁸ (an example is depicted in Figure 2.3¹⁹). The first stage consists of heating the substrate to the desired temperature and then evaporating In, Ga, and Se evenly. During the second stage, the Ga and In sources are turned off (or blocked), while Se and Cu are evaporated. If the second stage is Cu-rich, the grains are large ($\sim 1\mu\text{m}$); however, if the second stage is Cu-poor, the grains are very small. During the third stage, the Cu is turned off while In, Ga, and Se are deposited until the absorber is In-terminated (the In source is left on for ~ 20 sec longer than Ga to achieve a slightly In-rich surface). Due to the low sticking coefficient of Se, the overpressure is required to minimize the effect of Se partially desorbing from the surface. In contrast, the sticking coefficients for Cu, In, and Ga are very high, causing the film composition and growth rate to be

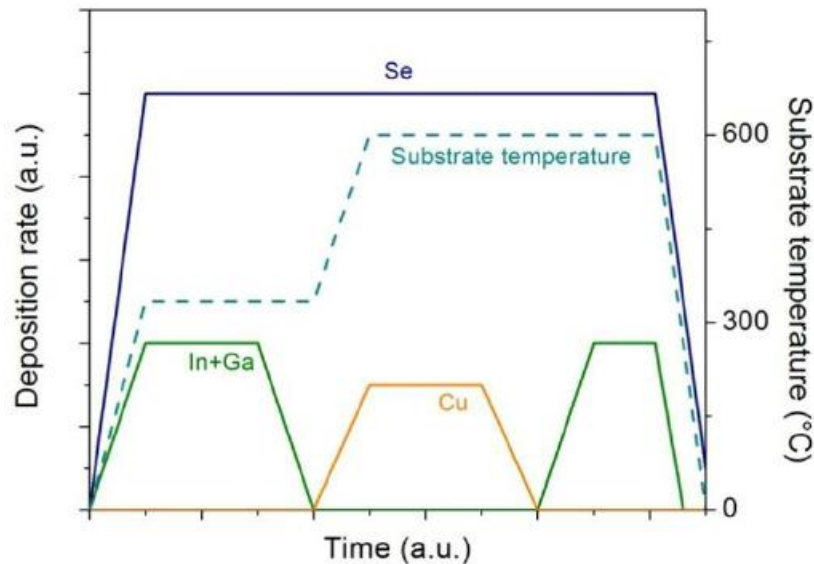


Figure 2.3: Flux schematic for an example of the three-stage coevaporation process. Taken from reference 19.

determined by the effusion rate and flux distribution of the metal precursors. Relative Ga:In ratios determine the bandgap of the film, and thus the coevaporation process is often adjusted accordingly (higher temperatures for larger Ga content) to achieve the desired bandgap (the bulk bandgap of CuInSe₂ is reported to be ~1.1 eV, while the reported bulk bandgap of CuGaSe₂ is ~1.6 eV²⁰). After the deposition process is completed, the absorber is about 2µm thick.

The three-stage coevaporation process deliberately creates gradients in the absorber²¹. If conducted as described above, the final CIGSe surface is Ga poor, while the Mo/CIGSe interface is Ga-rich and the absorber as a whole is Cu-poor with an even more Cu-poor surface. The compositional gradients in the absorber result in bandgap gradients with the widest bandgap at the surface, and the smallest at the back contact prompting some studies to suggest that the gradient bandgap is due to creating an ordered defect compound (ODC) Cu(In,Ga)₃Se₅ on the surface^{22–26}.

Theoretically, the suggested ODC layer creates an n-type surface and coupling this with the p-type bulk creates a buried p-n junction which helps minimize recombination at the absorber/buffer interface due to the wider surface bandgap^{11,22,24,26}. However, “n-type” and “p-type” are strictly bulk properties and cannot be used to describe the surface. Experimental data also shows that the ODC layer in fact does not exist and the bandgap gradient is merely due to the Cu-poor surface in contrast to the Cu-rich bulk^{23,27} revealing that the popular “buried p-n junction” idea is not accurate and the reduction in recombination is due to band bending as a result of the band gap gradient in the CIGSe absorber.

Another deposition method, favored by many industrial photovoltaic manufacturing companies due to better scalability and lower production costs, is the two-step processing deposition^{28,29}. Compositional uniformity and increased throughput make this deposition method more appealing for large-scale production. The two-step process is essentially the selenization (and/or sulfurization) of a stacked metal alloy. Evaporation, electrodeposition, and sputtering are some deposition techniques frequently used for creating the bi-layer or multi-layer stacked metal alloy²². The metal precursors are often pre-annealed to facilitate better interdiffusion in the growth of the stacked metal alloy. Selenization (and/or sulfurization) of the metal alloy occurs in a selenized atmosphere at high temperatures (400-500 °C) utilizing H₂Se or Se vapor, and typically results in absorbers with large grains and compositional uniformity²².

2.2.3 – Alkali incorporation in CIGSe

The importance of Na incorporation in CIGSe thin-film photovoltaics was realized as early as 1993 and continues to provide a motivation for fundamental research on the effects of Na in CIGSe³⁰. Schematics of various Na incorporation methods are presented in Figure 2.4. The most typical integration of Na is the use of a soda-lime glass substrate in the CIGSe device, allowing for Na diffusion through the Mo back contact into the CIGSe absorber (Figure 2.4-a). In an effort to control the Na-diffusion, a barrier is often deposited between the substrate and Mo and a deliberate NaF precursor is grown on the Mo (Figure 2.4-b)³¹. Other Na deposition methods include co-evaporation during the CIGSe deposition (Figure 2.4-c) or a post-deposition treatment (PDT) after the CIGSe absorber is grown (Figure 2.4-d). Various methods of alkali-incorporation in a CIGSe device is further explored in Chapter 5.

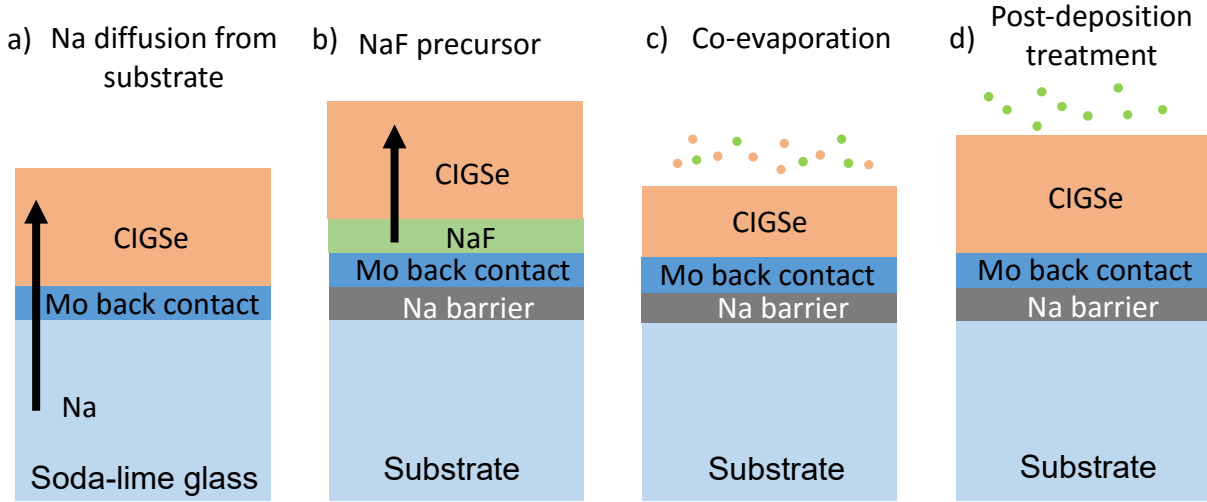


Figure 2.4: Schematics of various Na-treated CIGSe absorbers including a) diffusion from the soda-lime glass, b) Na barrier and NaF precursor, c) NaF coevaporated with CIGSe, and d) NaF PDT.

The role of Na is not fully understood and a number of studies speculate that Na sits at the grain boundaries, inducing defect passivation^{32–34}. Conclusive studies observe that Na sits primarily at the surface and affects the surface electronic properties of CIGSe absorber, altering the surface dipole and contributing to the valence band density of states and thus the buffer/absorber interface^{35–39}. With the incorporation of Na proving to be successful in CIGSe thin-film devices, the role of other alkali metals in CIGSe was studied as well^{10,34,40–43}. In 2014, EMPA raised the CIGSe-device world record efficiency (with a flexible polymer substrate) from 18.7% to 20.4% by incorporating a KF post-deposition treatment (PDT), and only a year later, ZSW increased the (glass-based) device record to 21.7%^{10,42}. A full understanding of the role of alkali incorporation is still of utmost importance for further optimization of efficiency and stability, and remains a frequent subject of study.

2.3 – BUFFER LAYERS

2.3.1 – CdS

Traditionally, a p-n junction in the CIGSe device forms at the buffer/absorber interface. Typically, n-type CdS is deposited onto the p-type CIGSe absorber to form the customary junction and normally leads to high efficiency devices^{3,8,18,44,45}. A chemical bath deposition (CBD) step deposits the CdS onto the CIGSe absorber⁴⁶. The absorber is immersed in a 65 °C solution of de-ionized (DI) H₂O, NH₄OH, CdSO₄, and CH₄N₂S (thiourea). As the CBD takes place, the immersed sample changes color (due to the index of refraction for CdS) as a function of the CdS thickness. The sample is then rinsed with DI H₂O and dried with compressed N₂. The CdS buffer layer plays two distinct roles in the CIGSe device: it acts as a protection layer, minimizing damage from the ZnO sputter deposition process (see Figure 2.2 and section 2.4), and it affects the electrical properties of the interface. With a reported bulk bandgap of 2.4 eV⁴⁷ and a thickness of 20 - 50 nm, utilizing CdS as the buffer allows for transparency and features very good optical transmission. Our group has experimentally shown interface intermixing between the CdS and CIGSe, with formation of CdSe and S in a Ga-S and/or In-S environment^{48–50}. Optimized high-efficiency CdS/CIGSe devices exhibit a flat conduction band alignment at the interface^{25,51–53} (see Section 2.3.3), allowing for unimpeded electron transport.

2.3.2 – Zn(O,OH,S)

Despite the success of utilizing CdS in high-efficiency CIGSe devices, the current CIGSe device world record of 22.3%, held by Solar Frontier K.K., utilizes a Zn-based buffer layer (their 20.9% record cell utilized Zn(O,OH,S))^{4,54}. Zn(O,OH,S) provides transmittance in the lower wavelength region of the solar spectrum that CdS does not provide. Thus,

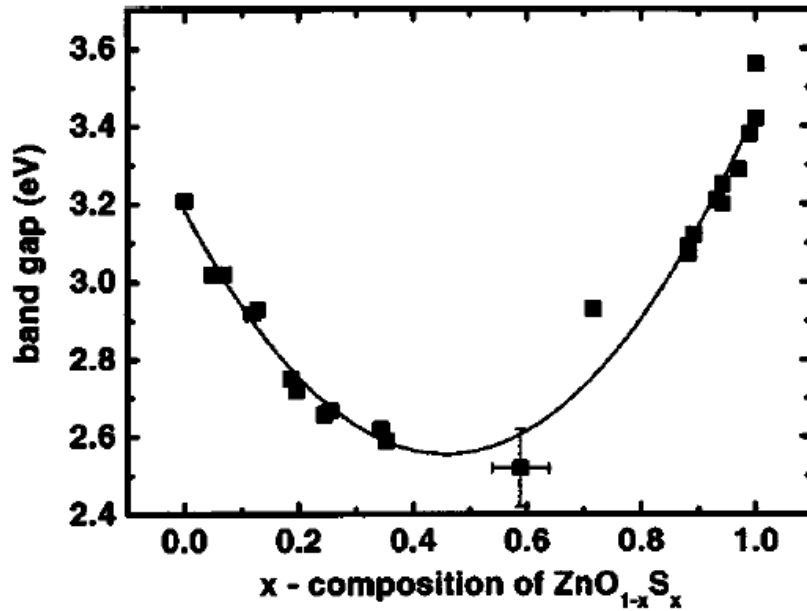


Figure 2.4: Optical bandgap as a function of O:S ratio in a Zn(O,S) alloy. Taken from 57.

Zn(O,OH,S) has potential for larger current collection and conversion efficiency. The higher transparency is due to the larger optical bandgap of Zn(O,OH,S) in relation to CdS. Although ZnO and ZnS have reported bulk bandgaps of 3.3⁵⁵ and 3.6 eV⁵⁶, respectively, the Zn(O,S) alloy exhibits a bowing effect in the optical bandgap as seen in Figure 2.4⁵⁷. The bowing effect is due to several factors, volume deformation, charge exchange, and structural relaxation⁵⁵. Deformation of the volume occurs when replacing the binary constituents (O and S) lattice constants, which in turn, deforms the band structure. The chemical-electronegativity contribution due to charge exchange in the alloy is relative to the ratio of O and S constituents, and the relaxation of the anion-cation bond lengths in the alloy contribute to the change in the structure. The smallest bandgap of the Zn(O,S) alloy is ~2.6 eV (when the O/(S+O) ratio is 0.40), which is larger than CdS by 0.2 eV, thus promising higher transparency over the entire composition range. Like CdS, Zn(O,S) is

typically grown utilizing CBD, but the recipe is changed to accommodate the different chemical properties of the constituents⁵⁸.

2.3.3 – Electronic band alignments

When a conduction band electron recombines with a valence hole at an interface, electron transport is impeded, and, in turn, the conversion efficiency of the solar cell is reduced. Understanding how the valence and conduction bands of the absorber align with the valence and conduction bands of the buffer layer at the interface is thus crucial in order to tailor the absorber and buffer layer properties to reduce recombination at the interface. Figure 2.5 shows schematics of several band alignment possibilities with the conduction band offset being a) flat, b) a spike, or c) a cliff. For all three scenarios, the left hand side (red) portrays the surface conduction band minimum (CBM) and surface valence band maximum (VBM) of a hypothetical solar cell absorber relative to the Fermi energy (E_F). The right hand side (blue) displays the surface VBM and CBM of a corresponding buffer. The center represents the interfacial band alignment, with the conduction band offset (CBO) and valence band offset (VBO) indicated by dotted lines. Ovals represent a correction for interface-induced band bending. The bands of the surface of a material will always bend (towards or away E_F) relative to the bulk of the sample to minimize the surface free energy. This includes the impact of the surface dipole, as well as long-range charge redistribution effects. This band bending will typically change when an overlayer is deposited to form the interface (i.e., essentially replacing the surface dipole with an interface dipole), unless it is hindered to do so by Fermi level pinning effects. The correction for interface-induced band bending in the band alignment picture considers such effects (if present). For a flat CBO configuration, unimpeded transport of the electron

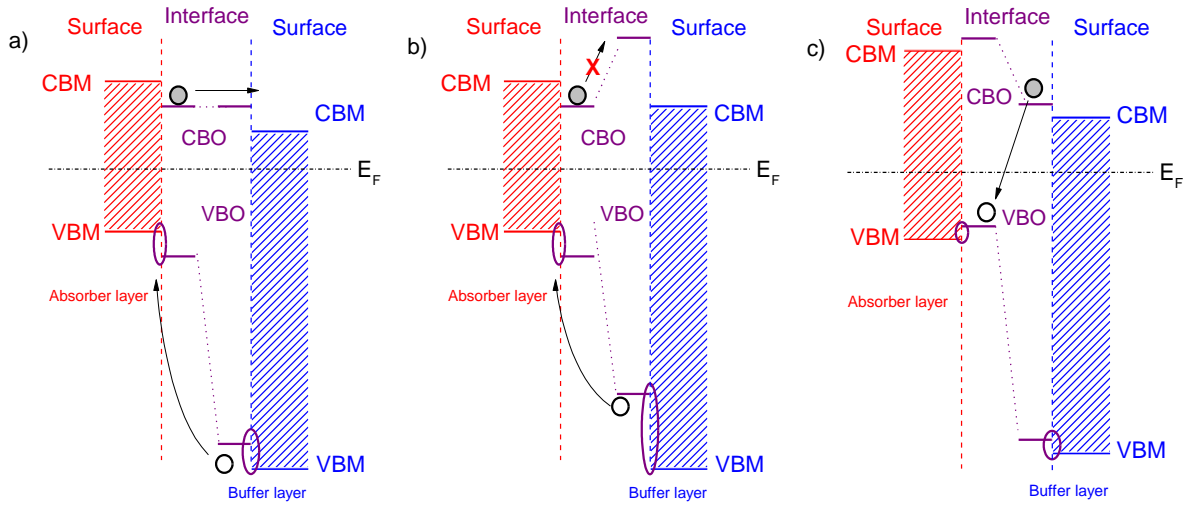


Figure 2.5: Schematic of several band alignment scenarios, a) flat, b) spike, or c) cliff configuration for the conduction band offset.

takes place whereas in the spike (b) configuration, an energy barrier inhibits electron transfer, leading to recombination. For the cliff (c) configuration, the CBO and VBO are close enough together in energy that the electron will recombine with the valence hole. High efficiency CdS/CIGSe and Zn(O,OH,S)/CIGSe devices exhibit a flat CBO at the interface^{25,52,59,60}.

The measurement of an interfacial band alignment, especially the CBO, is no trivial task due to difficulty in measuring the unoccupied states, and thus, modeling is often used. Before 1993, it was speculated that the efficiency of CdS/CuInSe₂ (CISe) devices was due to a type II “cliff” interfacial band alignment^{61–63}, supported by indirect measurements^{64,65}. However, after an experimental study utilizing synchrotron-radiation soft x-ray photoelectron spectroscopy and assumed band gaps presented a large CBO spike of 1.08 eV⁶⁶, subsequent investigations reported spike alignments (0.20 – 0.70 eV)

in the CBO^{24,67}. These studies also utilized photoelectron spectroscopy to measure the VBO of the buffer/absorber interface in chalcopyrites and assumed the CBOs based on reported bulk bandgaps. Since, modeling studies have suggested that buffer/absorber interfaces are less sensitive towards spikes than cliff arrangements^{68–71}. Our group has shown through the *independent* and *direct* measurements of both the valence band *and* conduction band that a characteristic of high efficiency CdS/CIGSe, CdS/CISe, CdS/Cu(In,Ga)(S,Se)₂, and Zn(O,S)/CIGSe is the presence of a flat conduction band alignment at the buffer/absorber interface^{25,51,52,60}. In contrast, a cliff-like CBO was measured for the less-efficient CdS/Cu(In,Ga)S₂⁵⁹.

2.4 – WINDOW LAYERS

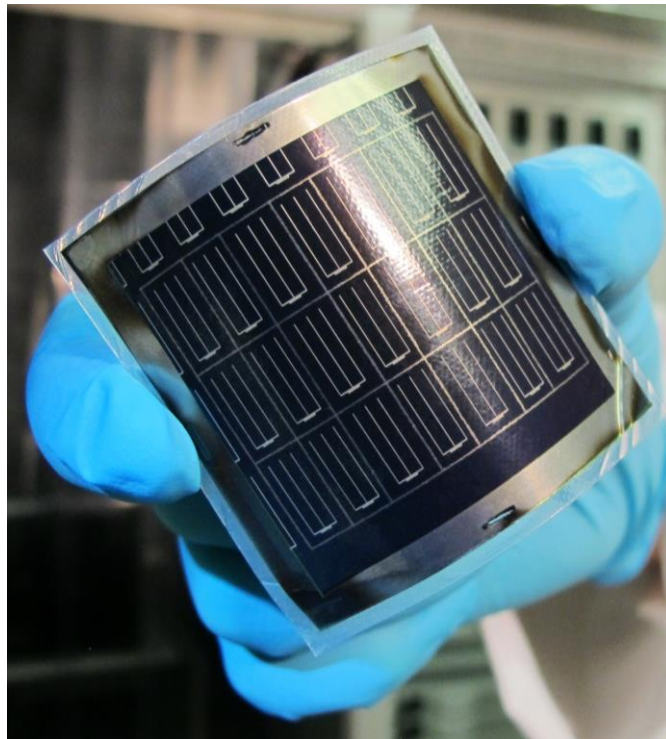


Figure 2.6: Example of a CIGSe minimodule deposited onto a flexible substrate from EMPA. Ref. from 76.

The window layer for the CdS/CIGSe device is generally a bilayer of transparent conductive oxides (TCO), most often intrinsic i-ZnO (resistive) and Al:ZnO (conductive)^{72–75}. The bilayer serves multiple roles, including the filling of pinholes to stop shunting, permitting internal reflection of photons of longer wavelengths, and acting as the front electrode^{74,75}. After the TCO deposition, Al, Ni, and a grid stencil are used to create the front-contact. The Ni offers adhesion while the Al is conductive. The design of the metal contact changes depending on the TCO and expected heat resistance to allow the best current. After the devices are tested for quality control, an anti-reflective coating is deposited. Figure 2.6 reveals a top view of a completed CIGSe minimodule on a flexible substrate from EMPA⁷⁶.

CHAPTER THREE

SPECTROSCOPY TECHNIQUES

Chapter three presents an overview of both lab-based (XPS, XAES, UPS, IPES) and synchrotron-based (XES) spectroscopy techniques that are utilized for the work published in this dissertation. Stefan Hüfner's *Photoelectron Spectroscopy*⁷⁷ and Briggs and Seah's *Practical Surface Analysis*⁷⁸ offer a more in-depth explanation of the photoelectron-based techniques and serve as the basis for the information presented in this chapter. Included in this chapter is also a brief description of the experimental set up at the Advanced Light Source (ALS), as well as sample preparation for the spectroscopy techniques listed above.

3.1 – INTRODUCTION

Photoelectron spectroscopy (PES) is a powerful technique, probing the chemical and electronic structure of surfaces and interfaces. The principle of this technique is based on the photoelectric effect: photons incident on the surface of a sample cause photoelectrons to eject, providing information on the elemental composition. While Heinrich Hertz originally discovered the photoelectric effect in 1887, Albert Einstein elucidated the theory in 1905 eventually winning him the Nobel Prize in 1921.

Fermi's golden rule provides the most widely used theoretical description of the photoelectron spectrum⁷⁹:

$$W_{i \rightarrow f} \propto \frac{2\pi}{\hbar} \left| \langle f | \hat{O} | i \rangle \right|^2 \delta(E_F - E_i - \hbar\nu) . \quad (3.1)$$

Fermi's golden rule provides the probability of a transition from a particular initial state to a particular final state via an operator that describes the electromagnetic field. The matrix

element is composed of the wavefunction of the final state ($\langle f|$), the perturbation operator describing the photon (\hat{O}), and the wavefunction of the initial state ($\langle i|$). The delta function ensures energy conservation. The concept and proper choice of initial and final states is very important in terms of understanding the underlying principles of photoelectron spectroscopy in general. For example, in x-ray photoelectron spectroscopy (XPS), the initial state is the N-electron state corresponding to the ground state, while the allowable final states each describe an N-electron configuration after the photon excitation. For example, the simplest final state is a state in which one electron is emitted after absorbing all of the energy of the photon, while the remaining N-1 electron system is unaffected. In a simplified one-electron model, this can be described as an electron in the core-level state (initial state) that is ejected into vacuum, leaving behind a core hole (final state). Thus, following Fermi's golden rule, the photoelectron spectrum is essentially dictated by the probability of an electron in the core-level being excited into the vacuum, and the resulting spectrum is a sum over all possible final states, weighted by the transition probability (which is zero if energy conservation is not obeyed).

3.2 – LAB-BASED SPECTROSCOPIES

3.2.1 – X-ray Photoelectron Spectroscopy (XPS)

XPS is a process in which photons (in the soft x-ray regime) excite electrons from the core levels into the vacuum. Their kinetic energy (KE) can be measured, offering chemical state information, predominantly of the sample surface due to the short inelastic mean free paths (IMFP) of the emitted photoelectrons⁷⁸. A schematic of the XPS process is displayed in Figure 3.1. The transition causes the system to be in a core-ionized state, and energy conservation dictates that

$$h\nu = KE + |BE| \quad (3.2)$$

with BE representing the binding energy and KE includes the work function, Φ_{sample} , of the sample. The energies are relative to the Fermi energy (E_F), achieved by grounding the sample to the detector and calibrating the energy axis following ISO standards proposed by Seah⁸⁰. XPS is powerful in terms of determining chemical environments due to the BE of the photoelectrons serving as a “fingerprint” of the photoelectron in question. Shifts in the BE also gives information on bonding environments, oxidation states, and adsorbate presence, as well as final state effects, such as (variations in) screening of the

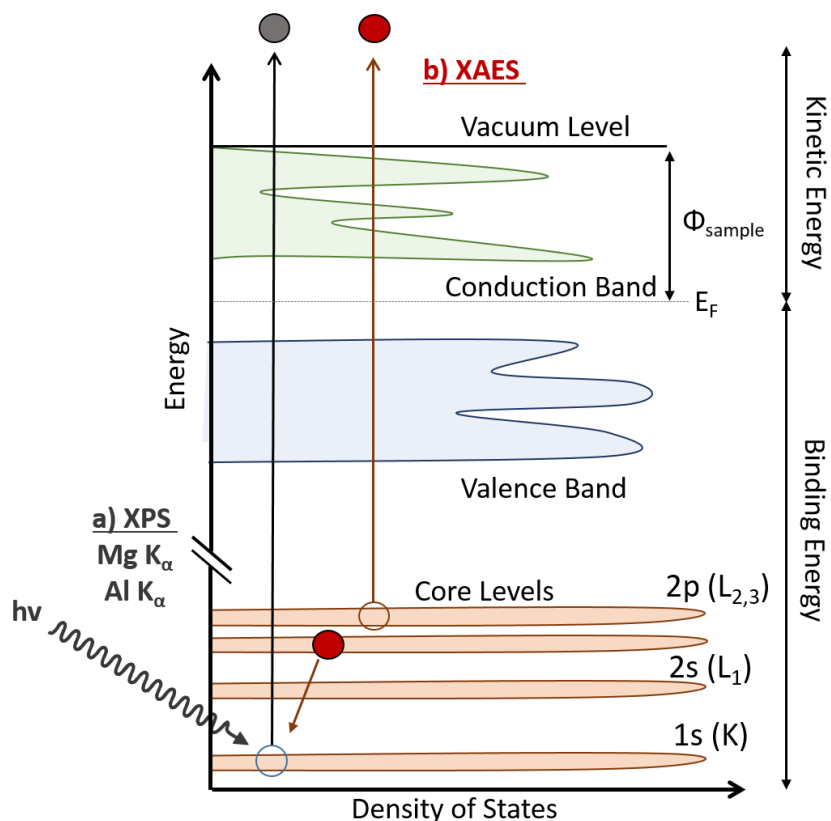


Figure 3.1: Schematic of a) X-ray photoelectron spectroscopy (XPS) and b) X-ray Auger electron spectroscopy (XAES) transitions.

hole(s) left behind in the final state. XPS spectra are usually plotted as intensity (count rate) vs. BE, since the KE of the photoelectron is dependent on the excitation energy.

3.2.2 – X-ray-excited Auger Electron Spectroscopy (XAES)

X-ray Auger electron spectroscopy (XAES) is a secondary radiationless process that takes place after a core-level is ionized. Figure 3.1 presents a schematic of this process. For example, an electron in the K shell (1s core level) is ionized, leaving behind a hole allowing an electron from an outer level, L₂ (2p_{1/2}), to relax into the hole. The energy gained can now be used to emit a characteristic photon (X-ray fluorescence) or to emit another electron in the same shell or a more shallow level (for example L₃ (2p_{3/2})), leading to Auger electron emission. The resulting notation takes into account the shells involved in the Auger process (e.g., O KL₂L₃ or O KL₃L₂). XAES is element-specific due to the localization of the core level wavefunction initially involved and, like XPS, sensitive to bonding environments, oxidation states, the presence of adsorbates, and final state effects (in this case involving *two* core or valence holes). XAES spectra are plotted as intensity (count rate) vs. KE, since the KE of the Auger emission is independent of the excitation source.

3.2.3 – Ultra-violet Photoelectron Spectroscopy (UPS)

The dispersive nature of the valence band (VB) requires a suitable excitation energy to maximize the spectral contribution of the orbital-specific derived bands. The ionization cross-section is largest when the excitation energy is similar to the orbital energy and thus, while XPS can be used to probe the valence band, ultra-violet photoelectron spectroscopy (UPS) would provide more information on this region due to the high flux of photons and narrow line-width of the radiation⁷⁸. He I (21.22 eV) and He

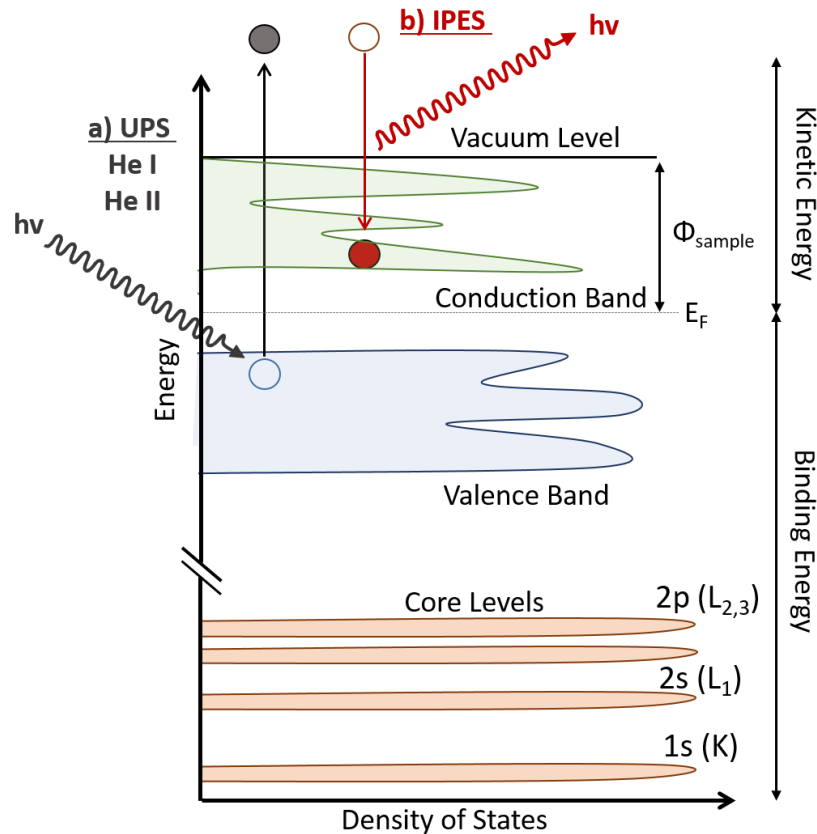


Figure 3.2: Schematic of a) ultra-violet photoelectron spectroscopy (UPS), and b) inverse photoemission spectroscopy (IPES).

He I (40.8 eV) are the most commonly used irradiation sources, however other noble gases like Neon are used as well. By using a UV source (i.e., He discharge lamp), a valence electron is excited out of the system and detected by the analyzer, as seen in Figure 3.2 (a). Following Fermi's golden rule, the spectrum is dictated by the transition probability of the valence band electron being excited to a one-electron final state at or above the vacuum level. The UPS spectra are plotted as intensity (count rate) vs. BE (relative to E_F), with the onset of the spectra describing the maximum energy in the VB. UPS spectra are calibrated using the E_F of clean Au foil.

3.2.4 – Inverse Photoemission Spectroscopy (IPES)

Inverse photoemission spectroscopy (IPES) is complimentary to XPS and UPS, yielding information on the *unoccupied* density of states above the E_F . A schematic of the process is shown in Figure 3.2 (b). A low energy electron beam hits the surface of the sample with energy E_i , allowing electrons to relax into unoccupied final states with energy E_f in the conduction band (i.e., above E_F for a semiconductor). This electron relaxation emits a photon with an energy of $E_i - E_f$, which is, in our case, detected with a Geiger-Müller detector. The detector combines a SrF_2 window and an $Ar:I_2$ gas filling, creating a bandpass filter at ~ 9.5 eV by combining the absorption onset of SrF_2 with the molecular photoionization energy of Iodine⁸¹:



By keeping the detection energy of the photon constant and changing the incoming electron energy range (8-16 eV), it is possible to measure the intensity distribution of the photons as a function of the final state energy (alternatively, it is possible to vary the detected photon energy by using a monochromator-based detection system instead of the band pass filter). The intensity distribution reflects the availability of empty electronic states above the Fermi level. Similar to UPS, the IPES spectra are plotted as intensity (count rate) vs. BE (relative to E_F), with the onset of the spectra representing the minimum energy in the conduction band (CB). The spectra are calibrated using the E_F of a clean Au foil.

3.2.5 – Combining UPS and IPES

Because UPS probes the VB and IPES probes the CB, the valence band maximum (VBM) and conduction band minimum (CBM) can be determined. This forms the basis of band

offset evaluations, and can also result in experimentally derived electronic surface bandgaps. In our group, a linear extrapolation is used to determine the VBM and CBM, which has proven in the past to be effective in taking experimental broadening, final state screening, inelastic losses, and dispersion of bands in k-space into account^{15,23,25,51,53,59,60,82–86}. Experimental broadening is, of course, present in both UPS and IPES, and thus the linear extrapolation needs to account for a broadening-induced tail. The tail depends on resolution and is a bigger issue for IPES spectra due to a poorer resolution (~0.4 eV compared to ~0.2 eV for UPS). Inelastic losses and final state screening can reduce the KE of the emitted electron, increasing the spectral intensity below the “true” VBM (and above the “true” CBM). In k-space, the energy of the bands depends on the crystal momentum of the electron, and hence the “true”, k-resolved VBM and CBM will be an upper (lower) bound of the distribution of the corresponding band, best described by a linear extrapolation.

3.2.6 – Surface Sensitivity

For XPS, UPS, XAES, and IPES, it is not the method of excitation that determines the surface sensitivity of the measurements, but rather the inelastic mean free path (IMFP) of the emitted (or incident) electrons. The longer the path of the electrons in the sample, the more likely they will inelastically scatter, and the IMFP is furthermore dependent on the kinetic energy of the electron and the sample composition (matrix). Inelastic scattering originates from many mechanisms, including electron-electron interactions, electron-photon interactions, electron-composition impurity interactions, etc⁸⁷. After the inelastic scattering process occurs, the scattered electrons might still reach the detector, but they do not contribute to the intensity at the correct final state energy for

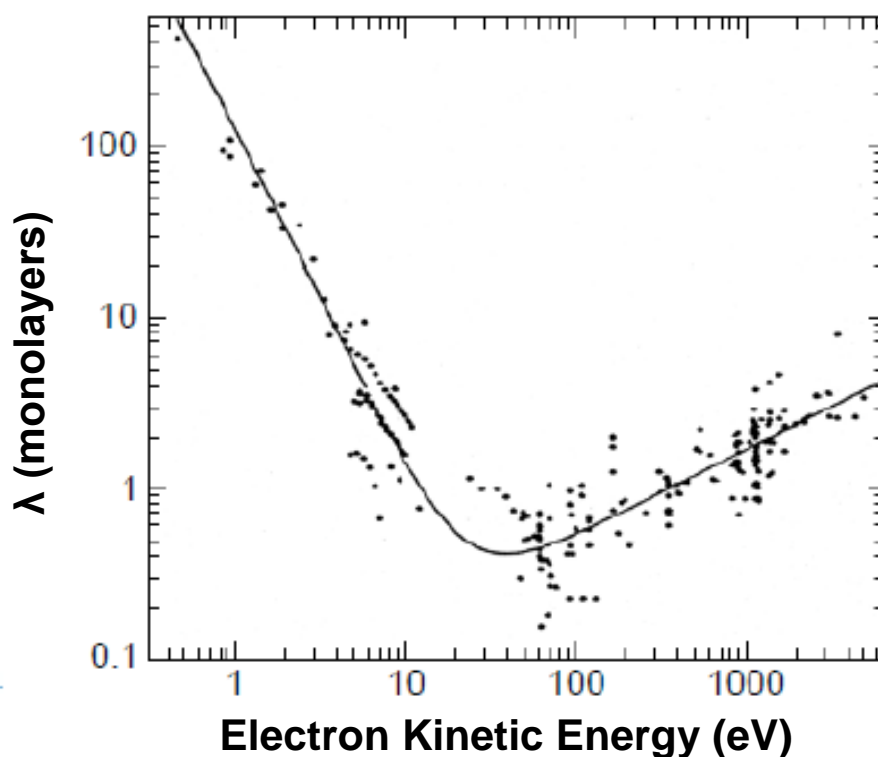


Figure 3.3: The “Universal Curve” (line that averages the experimental data points) presents the relationship of the inelastic mean free path of electrons as a function of their kinetic energy relative to the vacuum level. Adapted from reference 88.

the transition described by Fermi’s golden rule. Instead, they contribute to the background of the spectrum⁷⁸. This also holds true for IPES, where the primary detection of photons will come from electrons that have not lost energy prior to the radiation, while the background arises from photons emitted from electrons that are inelastically scattered⁸⁷. Thus, the surface sensitivity of XPS, UPS, XAES, and IPES greatly depends on the IMFPs of the electrons emitted from (relaxing into) the system. Figure 3.3 presents the “universal curve” which shows the relationship between IMFP (λ) and the KE of the photoelectron^{88,89}. The IMFP of an electron is at a minimum around a KE of 20-30 eV and

increases with a linear trend approximately \sqrt{KE} . The probability an electron travelling a distance, d , through the solid without undergoing scattering:

$$P(d) = e^{\frac{-d}{\lambda}} \quad (3.3)$$

Thus, it is an exponentially surface-weighted signal.

3.2.7 – Peak Fitting

In XPS, characteristic peaks of different orbitals can overlap (for example, Ga 3d at 20 eV and In 4d at 18 eV), often convoluting the information that could be derived from said peaks. Sophisticated software programs like FITYK⁹⁰ allow the user to fit a spectrum using various functions and create a model or fit (with a particular set of parameters) that is in close agreement with the data. However, shake off or shake up satellite peaks, multiplet splitting, etc., can cause features to appear in the spectrum that complicate fitting the background and the “true” contributions to the peak intensity of the specific element’s subshell.

Two popular methods to fit the background in an XPS spectrum include the simultaneous subtraction of a linear background (generally best for semiconductors) or, for metals, the prior removal of a Shirley background^{91,92} (possibly combined with the subtraction of an additional linear background/correction function as a simultaneous contribution during the fit). To describe the peak(s) in an XPS spectrum, symmetric Voigt functions are most appropriate for semiconductors (all fits performed in this dissertation use symmetric Voigt functions), as the function replicates contributions from both Gaussian and Lorentzian broadening. The Gaussian broadening, to first approximation, is intended to describe the experimental broadening, while the Lorentzian portion describes lifetime broadening of the core-hole. Metal XPS peaks are generally best

described by asymmetric line shapes, either an asymmetric Voigt or a Doniach-Šunjić line profile⁹³. Among other parameters, fitting the peak requires taking spin-orbit splitting and appropriately coupled values for Gaussian and Lorentzian line width contributions into account. The resulting residual (i.e., the difference between experimental data and fit) offers a function of merit for the fit.

3.3 – SAMPLE PREPARATION AND MEASUREMENT PARAMETERS

Ultra-high vacuum (UHV) is required to detect the electrons (photons for IPES) emitted from (or directed at) the sample to minimize collisions with gas particles between the sample and detector. In our group, samples are stored and prepared for measurement in an inert atmosphere environment (N₂) glovebox to minimize the amount of surface adsorbates. Once a sample is mounted onto a sample holder and electrically connected, it is introduced into the UHV system through a load-lock without any air exposure. XPS measurements are taken using Mg K_α (1253.6 eV; 1s → 2p transition) and Al K_α (1486.6 eV; 1s → 2p transition) radiation, and He I (21.22 eV; 1s² → 1s²p transition) and He II (40.81 eV; 1s → 2p transition) irradiation are used for the UPS measurements. For this dissertation, XPS and UPS measurements were taken with a SPECS PHOIBOS 150 MCD electron analyzer (fixed analyzer transmission mode), calibrated using core-level and Auger peaks of clean Ag, Cu, and Au foils (for XPS)⁷⁸, and the E_F of the Au foil (for UPS and IPES). A commercial low-energy electron gun (Staib) and a custom-built Dose-type detector with a SrF₂ window and Ar:I₂ filling⁸¹ were used for IPES experiments. The base pressure in the chamber was better than 5×10⁻¹⁰ mbar.

Because XPS and UPS are very surface sensitive, special care (the collaborators are asked to do the same) was taken to avoid any air exposure. Since the purpose of

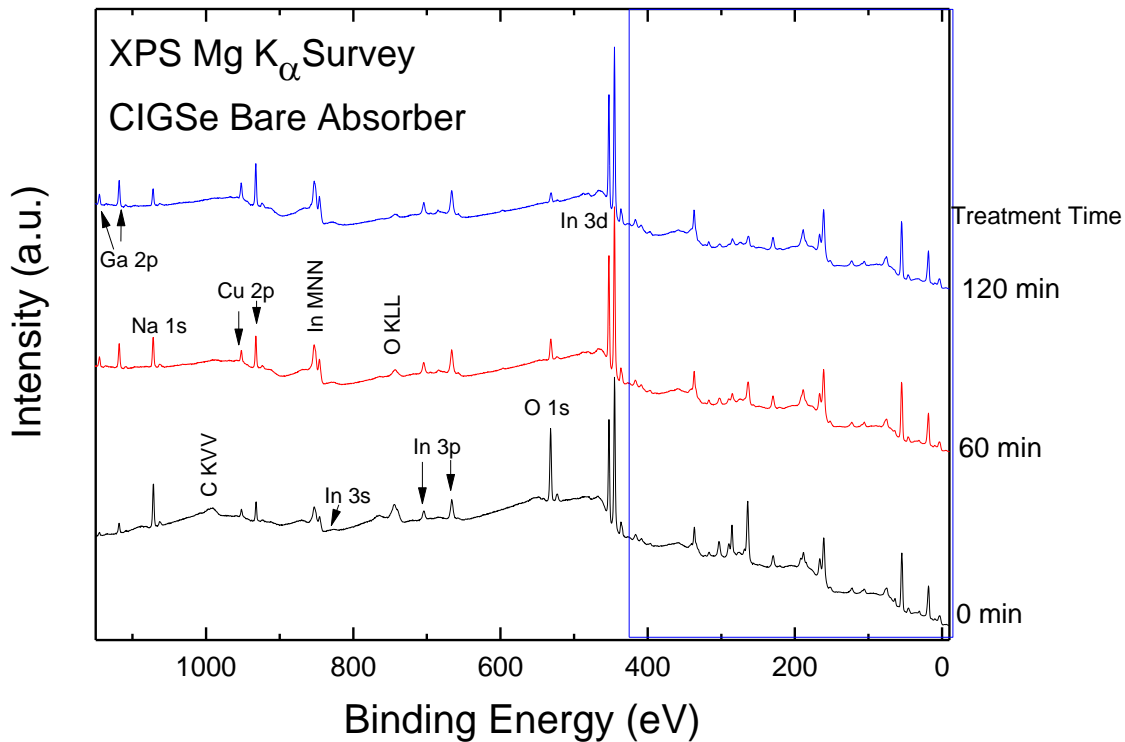
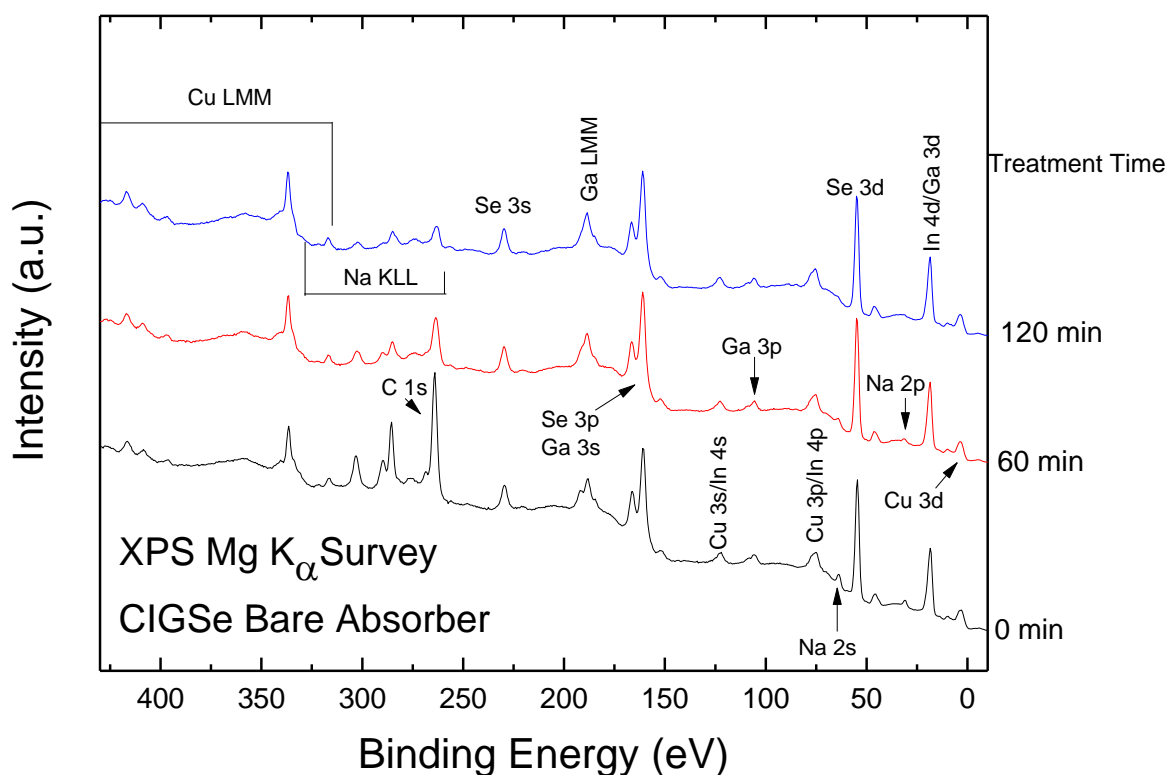


Figure 3.4: Mg K_{α} survey spectra of the $\text{Cu}(\text{In}_{0.7},\text{Ga}_{0.3})\text{Se}_2$ absorber as a function of treatment time during a low-energy ion cleaning series. Spectra in the blue box are shown on an enlarged energy axis in Fig. 3.5.

XPS, UPS, and IPES is to derive the surface electronic and chemical structure of the relevant surface/interface, surface adsorbates not only attenuate the pertinent peaks of the sample, but can also cause surface oxidation rendering the surface “not relevant”. To reduce the amount of surface adsorbates, samples were treated with a low-energy (50 eV) Ar^+ ion treatment at a low incidence angle, which has shown to be very effective in removing adsorbate (C and O) contaminants from CdS, ZnO, and chalcopyrite surfaces without creating metallic phases^{25,83}. An example illustrating ion treatments reducing surface adsorbates is shown in Figure 3.4 and 3.5. XPS measurements show surface contamination of C and O adsorbates on the bare CIGSe absorber, most notable by analyzing the C KVV, O 1s, and O KLL peaks (note the Ga LMM peaks overlap with the



Figures 3.5: XPS spectra of the low binding energy region before and after two low-energy ion treatment steps.

C 1s). The pertinent CIGSe photoemission and Auger lines (Cu, In, Ga, Se), as well as the Na lines are labeled, in addition to the adsorbate peaks associated with C and O. Two subsequent surface cleaning steps (of 60 minutes each) were taken in order to remove or reduce these adsorbate peaks. Due to the surface sensitivity of PES measurements, the C and O peaks are particularly pronounced since these atoms are located on the external surface. Consequently, all low-kinetic energy peaks (e.g., Ga 2p, Cu 2p, In MNN) are suppressed in intensity. Comparing the survey spectra taken after each ion treatment, the signal intensity of the CIGSe peaks are less attenuated, especially those at the higher BE region (lower KE), as the adsorbate peaks decrease. The Na 1s and Na KLL peaks also decrease with each treatment. Detailed spectra offer a better view of peak shifts with

the ion treatments. The band gap offset is determined by looking at relative core level peak shifts for the different layers. An adsorbate layer on the surface can cause the core level peaks to shift and hence found at peak position not representative of the “true” surface, but of the adsorbate contributions to the surface. For the untreated sample, the valence and the conduction band are dominated by the adsorbate contribution and thus shows a larger band gap, as seen in the UPS and IPES spectra in Figure 3.6. However, with each ion treatment, the Cu 3d-derived peak at $\sim 3\text{eV}$ becomes more pronounced and the valence band and conduction band exhibit reduced values which are closer to

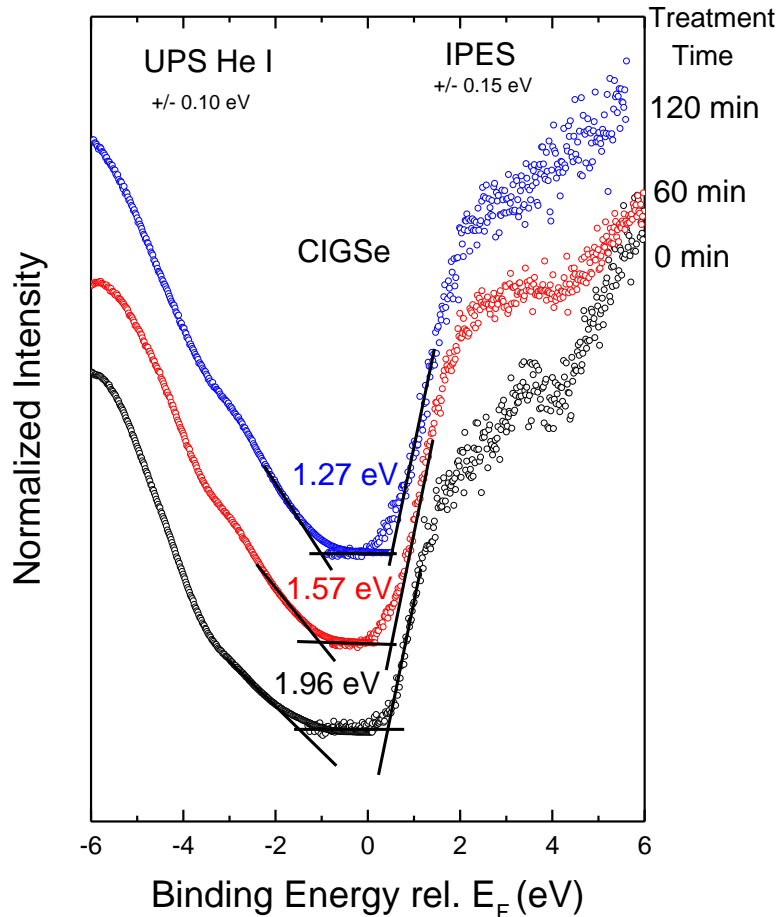


Figure 3.6: UPS and IPES spectra, showing the band edge positions (VBM and CBM) as well as the electronic surface band gap of the CIGSe absorber as a function of treatment time.

previously reported values^{25,51,52,59,60,84,86}. Note that the error bars of the techniques are not “statistically derived”. They describe a range of probabilities.

3.4 – SYNCHROTRON-BASED SOFT X-RAY SPECTROSCOPY

3.4.1 – X-ray Emission Spectroscopy (XES)

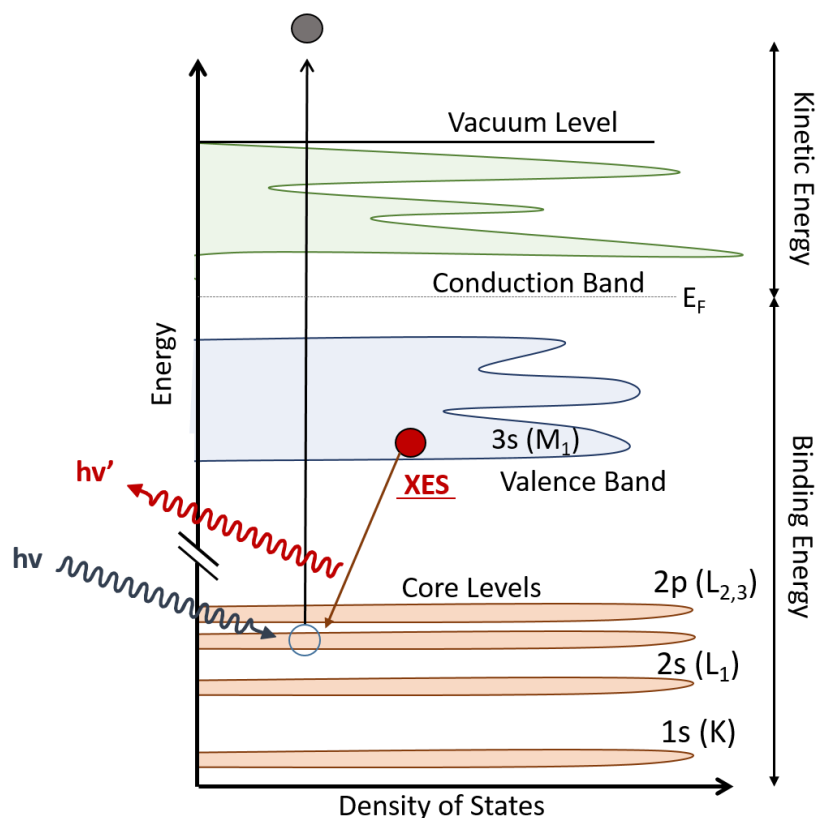


Figure 3.7: Schematic of x-ray emission spectroscopy transitions. The “zero” step of the process is colored gray while the XES process is in red.

X-ray emission spectroscopy (XES) is a photon in – photon out spectroscopy technique in which a core-hole is filled by an electron from the valence band (as a “0th step”, a photon has previously excited a core electron and removed it from the system). The XES transition emits a photon with an energy given by the energy difference between the levels

involved in the transition. A schematic of the XES process is shown in Figure 3.7. The “0th step” of the process is shown in gray, while red represents the XES process. Possible presence of core-exciton states can be distinct and discernable in a spectrum and often appear as additional states near the VBM (XES) or CBM (x-ray absorbance spectroscopy)⁹⁴. As a result, the core-exciton obscures the true VBM (CBM) and resulting bandgap approximations should be taken as a minimum value²³. The XES process is governed by the dipole selection rule ($\Delta l = \pm 1$), resulting in a spectrum where only suitable valence states will be observed. XES thus represents a measurement of the *partial* occupied density of states near the probed atom (i.e., the near the original core hole). This is in contrast to XPS and XAES, which measure the total occupied density of states.

Similar to PES, the intensity of the emitted photons in the XES process also follows

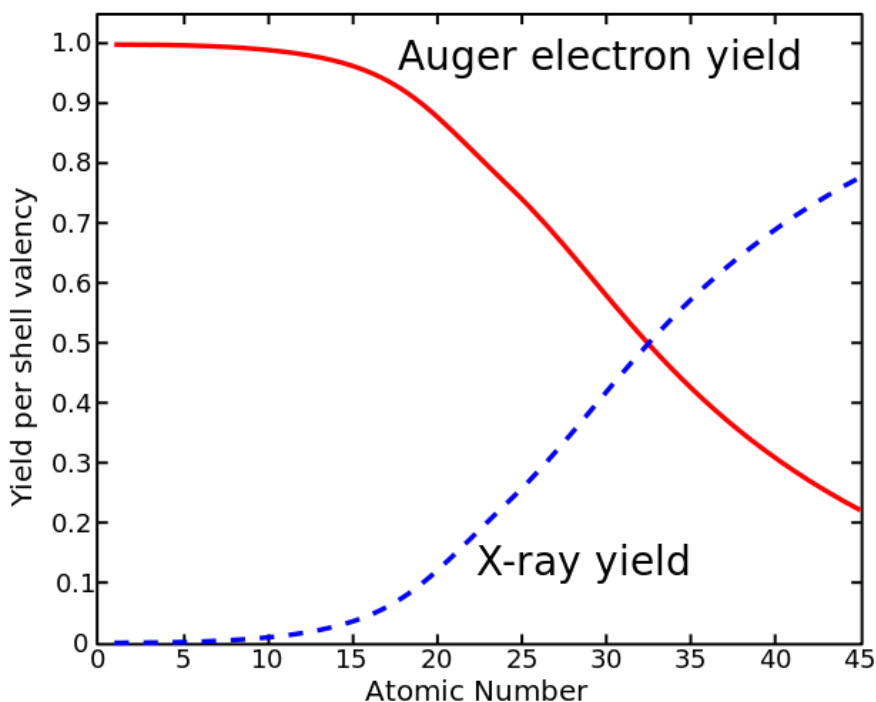


Figure 3.8: The fluorescence and Auger yields for the K subshell as a function of Atomic number Ref. from 96, 97.

Fermi's Golden rule (see equation 3.1). While the surface sensitivity of PES is governed by the IMFP of the emitted electrons, XES is governed by the attenuation lengths of the involved photons⁹⁵. Depending on the excitation energy for a XES measurement, the near-bulk to bulk region is probed, in contrast to the surface-sensitive measurements of PES. The x-ray emission process is in competition with the Auger emission process. Figure 3.8 displays the fluorescence and Auger yields for the K subshell as a function of atomic number^{96,97}. The Auger emission dominates for low atomic numbers, causing the probability of radiative decay in the soft x-ray regime to be very low^{96,98}. Only for higher atomic numbers does the fluorescence become comparable (and, eventually, dominant) to the Auger yield. At these atomic numbers, the emitted fluorescence photon will have energies in the hard x-ray regime and offer substantially reduced chemical information.

To nevertheless also gain insights in the chemical bonding and occupied valence states with soft x-ray XES, it is possible to overcome the "yield challenge" by utilizing a high flux, tunable excitation source and a high-efficiency spectrometer (as will be described in the following section). This allows for measurement times comparable to lab-based techniques like XPS and XAES.

3.4.2 – Beamline Description

XES experiments were performed on Beamline 8.0.1.1 at the Advanced Light Source (ALS), Lawrence Berkeley National Laboratory. Figure 3.9 offers a look at the set-up of Beamline 8.0.1⁹⁹. The synchrotron radiation is produced by a 5-cm period undulator (and used in the first, third, or fifth harmonic). The beamline allows an energy range of 80-1250 eV and a photon flux between 10^{11} and 6×10^{15} photons per second, depending on the resolution and energy⁹⁹. Apertures and focusing mirrors shape and direct the beam

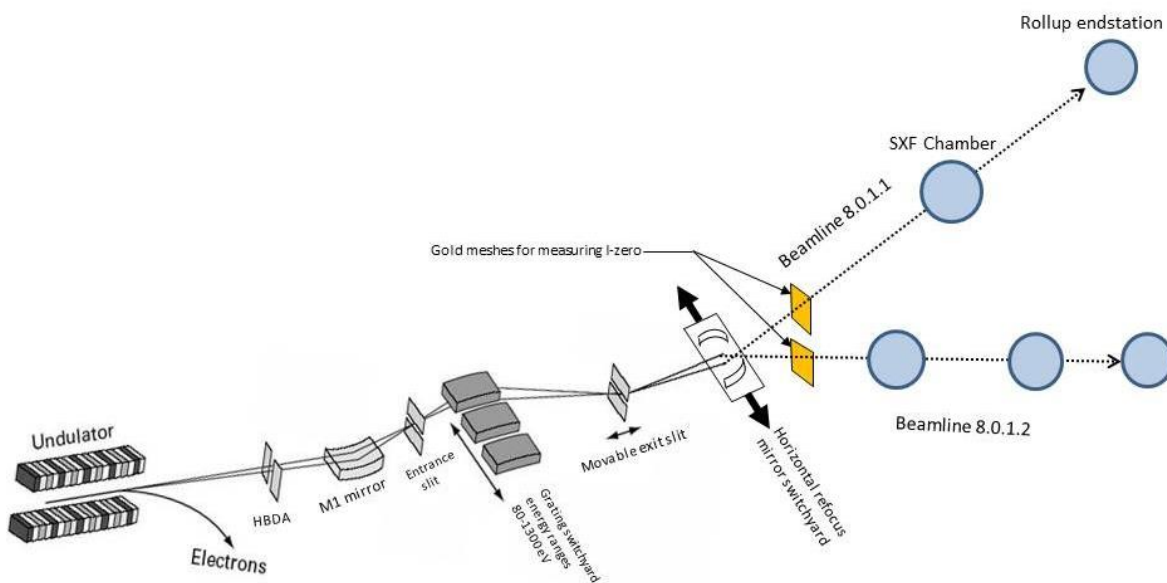


Figure 3.9: Schematic of Beamline 8.0.1 at the Advanced Light Source (ALS). Taken from ref. 99

through the entrance slit, monochromator spherical grating, and exit slit. The beam can be directed to either the permanently installed Soft X-ray Fluorescence (SXF) endstation¹⁰⁰ or the custom-built Solid and Liquid Spectroscopic Analysis (SALSA) endstation¹⁰¹. SALSA utilizes a high-efficiency variable line spacing (VLS) spectrometer, which has a spectral resolving power of $E/\Delta E > 1200$ over the energy range 120 to 650 eV. The SXF spectrometer is based on the Rowland Circle concept and has a spectral resolving power $E/\Delta E$ between 400 and 1900¹⁰². XES data in this dissertation were taken on either the SALSA or SXF endstation, which will be noted in the experimental section of each chapter.

CHAPTER FOUR

CHEMICAL AND ELECTRONIC SURFACE PROPERTIES OF ALKALI-TREATED CIG(S)Se ABSORBERS: COMPARISON OF INDUSTRY AND NATIONAL LAB THIN- FILM CHALCOPYRITE ABSORBERS

4.1 – INTRODUCTION

In November 2014, a new world record efficiency for CIGSe thin-film photovoltaics with a flexible substrate was set by EMPA, raising the efficiency from 18.7% to 20.4%¹⁰. At this time, NREL held the world record, 20%, for CIGSe deposited on a soda-lime glass substrate, and today's chalcopyrite world record is 22.3 %, achieved with Zn-based buffer layer, CIGS₂Se absorber, and a soda lime glass substrate by Solar Frontier^{4,54,103}). The reason for the large jump in conversion efficiency was attributed to alkali-post deposition treatments (PDT) which arguably, changed interfacial properties between CIGSe and CdS along with mitigating optical losses in the CdS buffer layer¹⁰. With this new record, KF treatments became the new “hot topic” in the chalcopyrite industry and only a year after the 20.4% record was set, ZSW achieved a new world record of 21.7%¹⁰⁴ (on a soda lime glass substrate). While the importance of Na incorporation into the CIGSe absorber is well known and established^{35–38}, research into the effect of KF have only emerged in the past few years.

A common finding with the KF-PDT is the depletion of Cu on the surface of the CIGSe, which in turn affects the surface electronic structure; however, this has only been reported for CIGSe deposited using the three-stage coevaporation process commonly used to create laboratory-scale research devices^{10,34,43}. Industrial companies, on the other hand, often incorporate S into the chalcopyrite absorber and do not use the three-

stage coevaporation process, instead opting for cheaper and streamlined deposition processes on both rigid and flexible substrates ^{105–107}. Because there is a need to bridge the gap between laboratory scale and industrial module efficiencies, more research is required in order to understand the role of KF in industry made chalcopyrites and its comparison to laboratory scale results.

Thus, to gain insight on the effects of KF PDTs on industry deposited CIGS_{Se} and compare them to laboratory scale CIGSe, we employ XPS and UPS (at UNLV), as well as XES (at the ALS) to investigate the chemical and electronic properties of the absorbers surface.

4.2 – EXPERIMENTAL DETAILS

Two alkali-PDT CIG(S)Se sample series were deposited, one at NREL and one at STION utilizing two different absorber deposition techniques. The NREL PDIL (process development and integration laboratory) CIGSe absorbers were deposited using the standard three-stage process ($\text{Ga}/(\text{Ga}+\text{In}) = 0.3$) on a Mo-sputtered soda lime glass substrate ¹⁸. The deposition of the STION CIGS_{Se} absorbers utilized a proprietary 2-stage sputter process. The first step involves physical vapor deposition of Cu, In, and Ga while the second step involves the sulfurization and selenization of the metals to create the CIGS_{Se} semiconductor. Note that the STION absorbers contain S while the NREL PDIL absorbers do not. The alkali (Na and K) post-deposition treatments were performed at NREL for both the STION and NREL PDIL absorbers resulting in two sample sets of a bare absorber, NaF-PDT absorber and two KF-PDT absorbers. All samples, excluding the bare absorbers, were rinsed (100 ml H₂O + 12.5 mL 28% NH₄OH reagent) for four minutes at 65 C. The samples each gave different device efficiencies with the NREL NaF-

treated absorber having the highest efficiency (18.2%) and one of the NREL PDIL KF-treated absorbers having the least (2.8%). The absorbers identification is presented as following: STION CIGSSe absorbers: “Bare-14.6%”, “NaF-14.6%”, “KF-4.5%”, and “KF-11%”. NREL CIGSe absorbers: “Bare-17.9%”, “NaF-18.2%”, KF-2.8%, and “KF-16.7%”. The numbers correspond to the efficiency of that particular sample.

The samples were briefly air-exposed, packed and vacuum-sealed under dry nitrogen before being sent to UNLV. The samples were unsealed in an inert environment, mounted, and introduced to the UHV system. XPS, UPS (UNLV), and XES (ALS) were utilized to investigate the chemical and electronic structure of both the STION and NREL sample sets. Mg K_{α} and Al K_{α} irradiation and a SPECS PHOIBOS 150 MCD electron analyzer were employed for XPS measurements and He II for the UPS measurements. The spectra were calibrated using Auger and core-level peaks of clean Cu, Ag, and Au foils (XPS)⁸⁰ and the Fermi energy of a clean Au foil (UPS).

X-ray emission spectroscopy was conducted at beamline 8.0.1 in the ALS utilizing a high-transmission variable-line grating spectrometer (VLS) on the SALSA endstation¹⁰¹ for the S $L_{2,3}$ edge. The K $L_{2,3}$ and F K_{α} were taken on the soft x-ray fluorescence (SXF) endstation¹⁰⁰ installed on beamline 8.0.1 and calibrated according to the appropriate references (CdS¹⁰⁸ for the S $L_{2,3}$ and KF for K $L_{2,3}$ and F K_{α}).

All peaks were analyzed by fitting the different spectral intensities with Voigt functions (with coupled Lorentzian and Gaussian widths) and a linear background using the Fityk peak-fitting program⁹⁰. The valence band maximum (VBM) was determined by linear extrapolation of the leading edge in the valence band (UPS) spectra¹⁰⁹. The base

pressure in the UNLV analysis chamber, VLS analysis chamber, and SXF chamber were $<5 \times 10^{-10}$ mbar, $<1 \times 10^{-9}$ mbar, and $<1 \times 10^{-9}$ mbar, respectively.

4.3 – RESULTS AND DISCUSSION

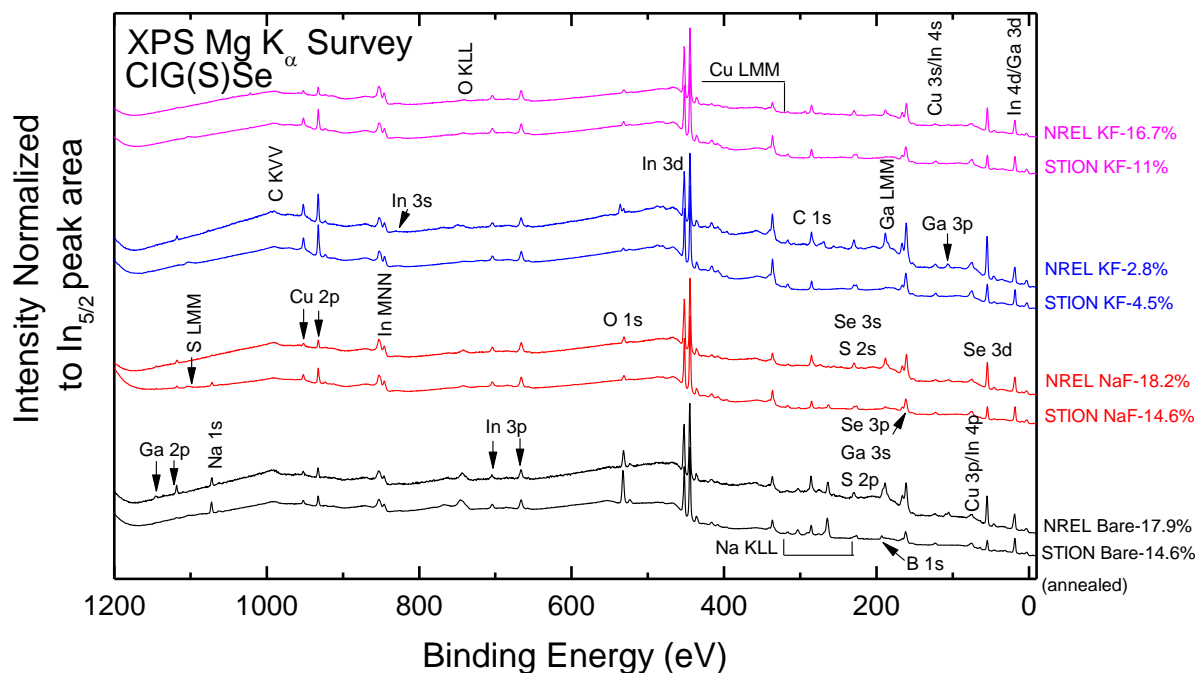


Figure 4.1: XPS survey spectra normalized to the $\text{In}_{5/2}$ peak area of the NREL and STION bare absorbers (black), both NaF-treated absorbers (red), both low efficiency KF-treated absorbers (blue), and both high efficiency KF-treated absorbers (pink).

The XPS survey spectra of the CIG(S)Se absorbers normalized to the $\text{In}_{3d_{5/2}}$ peak area (to look at respective Cu:In, Ga:In, and Se:In ratios) are presented in Figure 4.1. All the pertinent CIG(S)Se peaks are present and labeled (i.e. Cu, Ga, Se, In, S) along with peaks associated with Na and surface adsorbates (C and O). The STION annealed absorber has an unusually high O 1s and O KLL peaks in comparison to the much smaller O signal seen for all other samples while the C 1s and C KVV peaks are similar among all the samples. Substantial Na 1s and Na KLL peaks are present for both the STION and

NREL bare absorber and small Na peaks are seen for the NREL NaF rinsed sample. The Na peaks for the other samples are either not present or too small to view at the scale of the survey spectra. They will be discussed in more detail later. Because the survey spectra are normalized to the In 3d_{5/2} area, changes in the Cu:In ratio are clearly seen between the rinsed samples with the low efficiency KF-rinsed samples have the largest Cu intensities, indicating a more Cu-rich surface. The Ga signal is very weak for all the STION absorbers, suggesting a more Ga-poor surface in comparison to the NREL absorbers. The STION bare absorber has an additional peak at 193 eV, which is most likely B 1s (which will be discussed in detail). While analyzing survey spectra allows for an overview of what is occurring on the sample surfaces, detailed regions of the various core-level and Auger peaks allow for a more in depth analysis of the surfaces.

Thus, in order to gain insight on the Cu:In ratio changes between the samples, the Cu 2p_{3/2} peak in Figure 4.2 (left) is normalized to the In 3d_{5/2} area. Both low-efficiency KF samples have the most Cu-rich surface in the sample series, with the amount of Cu being comparable between the two samples. In general, the STION absorbers exhibit a more Cu-rich surface relative to the NREL absorbers. It is well known in the CIGSe community that a Cu-poor surface for the CIGSe absorbers helps lead to higher efficiency devices^{21,24,110}. Note also that while the Cu:In ratio decreases with alkali-treatment (KF-2.8% is the exception) for the NREL absorbers, the opposite is seen for the STION absorbers. In fact, the Cu:In ratio is almost doubled for the KF-11% absorber, suggesting that although both set of absorbers received the same KF-PDT, the industry absorbers do not have the same Cu depletion at the surface that has been published for research-based laboratory scaled absorbers^{10,34,43}. In Figure 4.2 (right), the Cu 2p peaks are

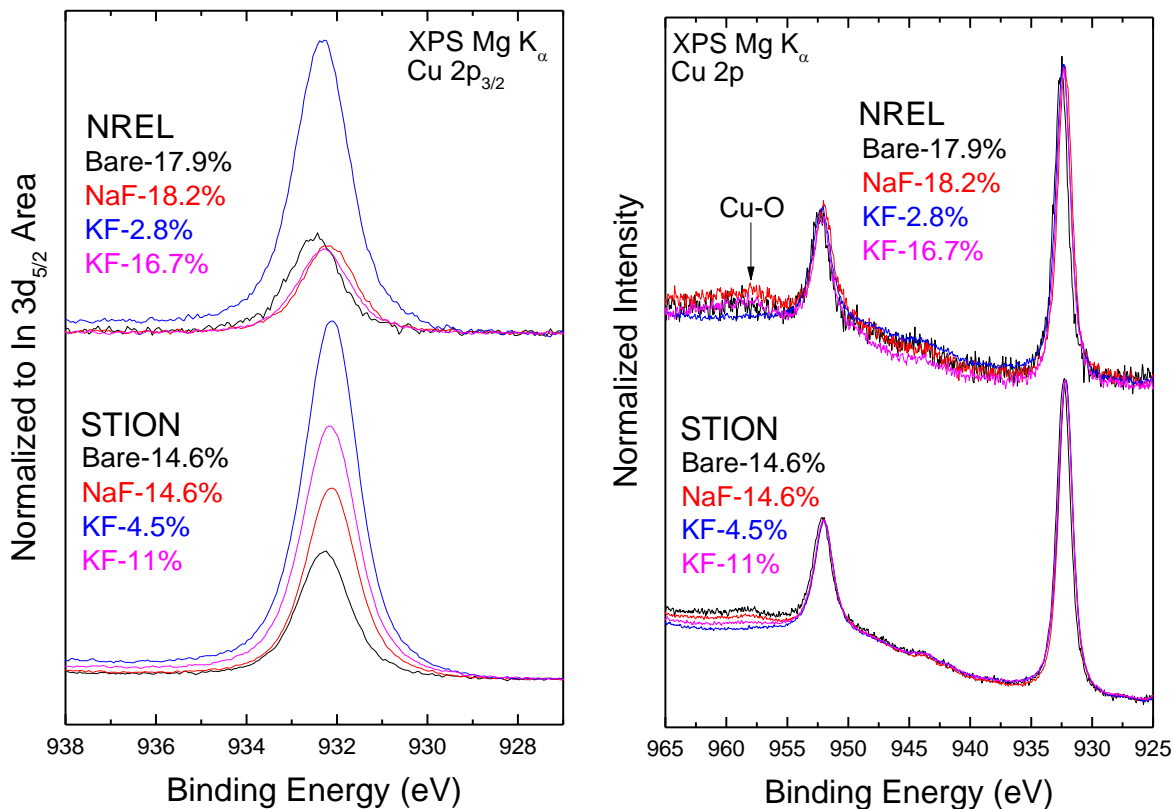


Figure 4.2: XPS detailed spectra of the Cu 2p_{3/2} peak normalized to the In_{5/2} peak area (left) and to Cu 2p_{3/2} peak height (right) of the NREL and STION bare absorbers (black), NaF-treated absorbers (red), and low and high efficiency KF-treated absorbers (blue, pink).

normalized to the main peak height in order to look at shape changes between the spectra. The component seen at ~957 eV is indicative of Cu-O bonds and it is present in all the samples except the low-efficiency KF-treated absorbers. The Cu 2p peaks of all the rinsed samples shift towards lower binding energies relative to the bare absorber of the respective sets.

The Ga intensity relative to In is investigated in Figure 4.3, left, while the shape changes of the peak are seen on the right. In general, the STION absorbers exhibit a more Ga-poor surface relative to the NREL absorbers. Both high-efficiency KF absorbers exhibit the lowest Ga:In ratio indicating the surface of these absorbers are more Ga-poor

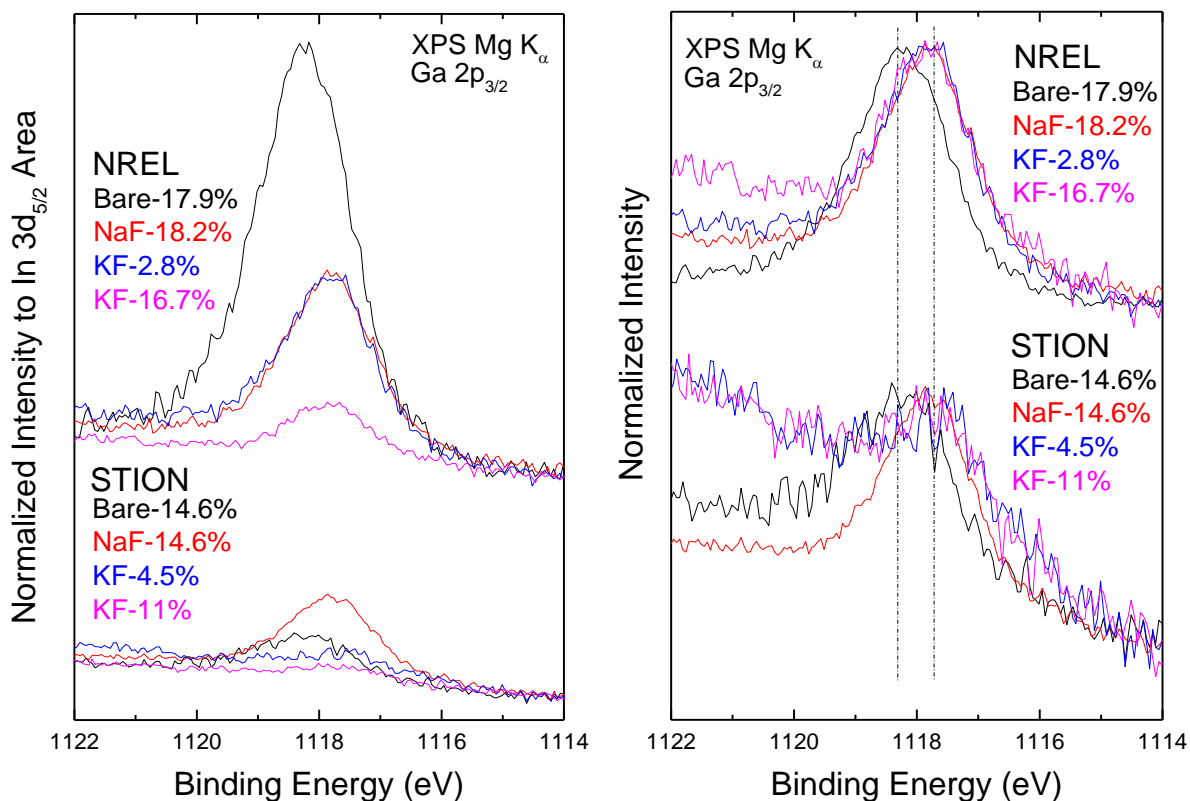


Figure 4.3: XPS detailed spectra of the Ga 2p_{3/2} peak normalized to the In_{5/2} peak area (left) and to Ga 2p_{3/2} peak height (right) of the NREL and STION bare absorbers (black), NaF-treated absorbers (red), and low and high efficiency KF-treated absorbers (blue, pink).

than the respective samples in their set. The NREL bare absorber Ga 2p_{3/2} peak is asymmetrical suggesting the presence of multiple Ga species. All the rinsed samples shift ~0.6 eV towards lower binding energies relative to their respective bare absorbers. This could signal a change in chemical environment (removal/reduction of Ga-O) and/or band bending at the surface.

To confirm that Ga-O species are present, the Ga LMM peak needs to be analyzed, as seen in Figure 4.4 (left). A third component, indicative of a Ga-O species, is visible for the NREL bare absorber at ~1063 eV (kinetic energy). It is more difficult to assess if this peak is found on the STION bare absorber due to the additional peak, not associated with

Ga LMM, at ~1060 eV. By rinsing the absorbers with an alkali-treatment, the Ga-O contaminant species was removed and/or reduced. A small shoulder is visible for both NaF absorbers indicating that the rinse did not completely remove the Ga-O species while for all the KF species, the shoulder is not detected. Further analyzing the STION bare absorber shows that the large peak at ~1060 eV is not actually part of the Ga LMM profile and this is proven by switching excitation sources and measuring the same region.

In the top of Figure 4.4 (right), the NREL bare absorber Se LMM Auger region taken with Al K_{α} is shown in blue and underneath, in black, is the same region taken Al K_{α} of the STION bare absorber. The energy axis of this graph is now in binding energy

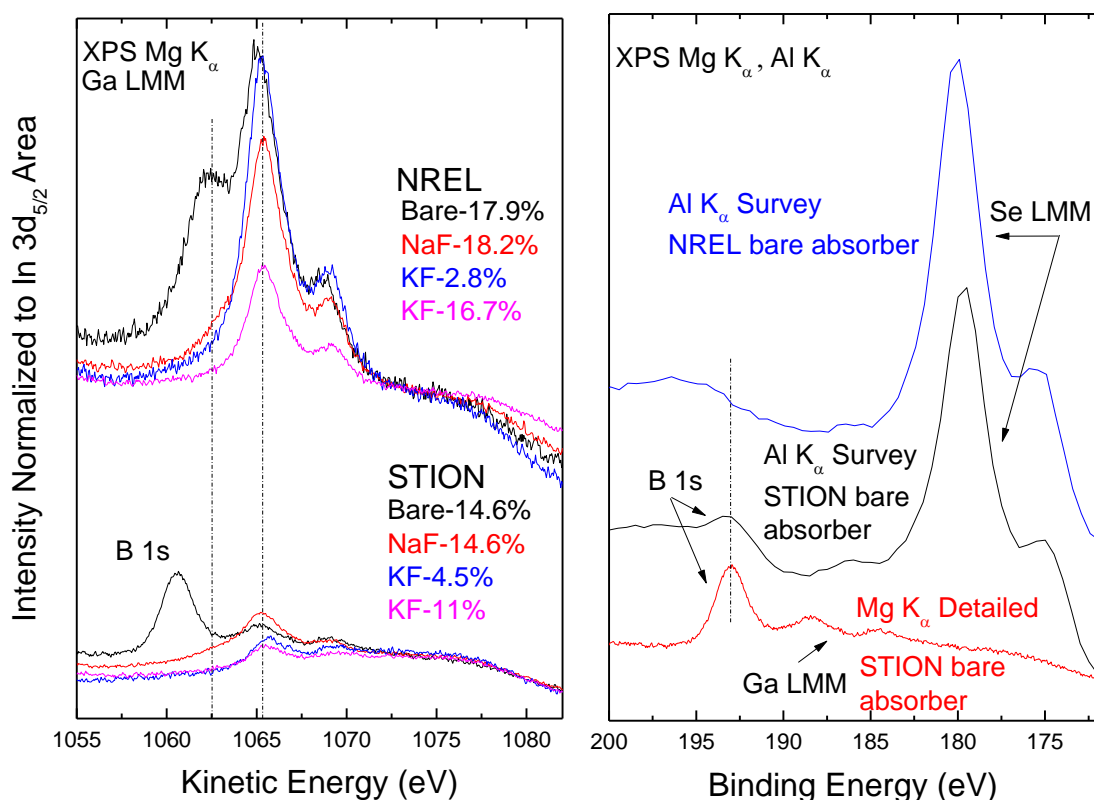


Figure 4.4: XPS detailed spectra of the Ga LMM Auger peak normalized to the In 3d_{5/2} peak area (left) and to Ga LMM peak height (right) of the NREL and STION bare absorbers (black), NaF-treated absorbers (red), and low and high efficiency KF-treated absorbers (blue, pink).

(whereas the left graph is kinetic energy). With different excitation energies, the binding energy of the Auger peak will change (the kinetic energy, however, will not). Thus, the red spectrum is the same region but taken with Mg K_{α} excitation. This is why the Se LMM appears in the Al K_{α} spectrum (but not the Ga LMM) and the Ga LMM appears in the Mg K_{α} spectrum (but not the Al K_{α} spectrum) in this region. Using the dotted line as a guide for the eye, there appears to be a component in the black spectrum (Al K_{α}) that is in the same position as the peak in the red spectrum below. However, to make sure that this component was not a part of the Se LMM profile, the Se LMM of the NREL bare CIGSe absorber is featured above (blue) and it is clear that this component is not part of the Se LMM. Thus, it is not part of the Ga LMM as well. This peak at 193 eV (1060 eV kinetic energy) is attributed to B 1s, corroborated by literature ^{111,112} and suggests a B contamination in the production line of the STION bare absorber. Note, this peak is not found in the XPS spectra of the other samples.

In order to take a closer look at the surface Ga/(Ga+In) ratio, fits of the Ga 3d/In 4d region were created and are presented in Figure 4.5 (NREL) and Figure 4.6 (STION). All the peaks were fit with a linear background, Voigt functions and couple Gaussian and Lorentzian contributions. The spin-orbit splitting and the spacing between the In 4d_{5/2} and In 4d_{3/2} and in between the Ga 3d_{5/2} and Ga 3d_{3/2} were fixed (0.86 eV for In and 0.46 eV for Ga) according to literature^{113–115}. The resulting residual of the fit is shown below each region in purple (note the magnification factors). These shallow core levels already possess some band character, and thus the quality of the fit is very surprisingly high for the NREL absorbers, especially given all the above-mentioned boundary conditions included in the fit. It is apparent that the surface Ga/(Ga+In) ratio changes with the alkali-

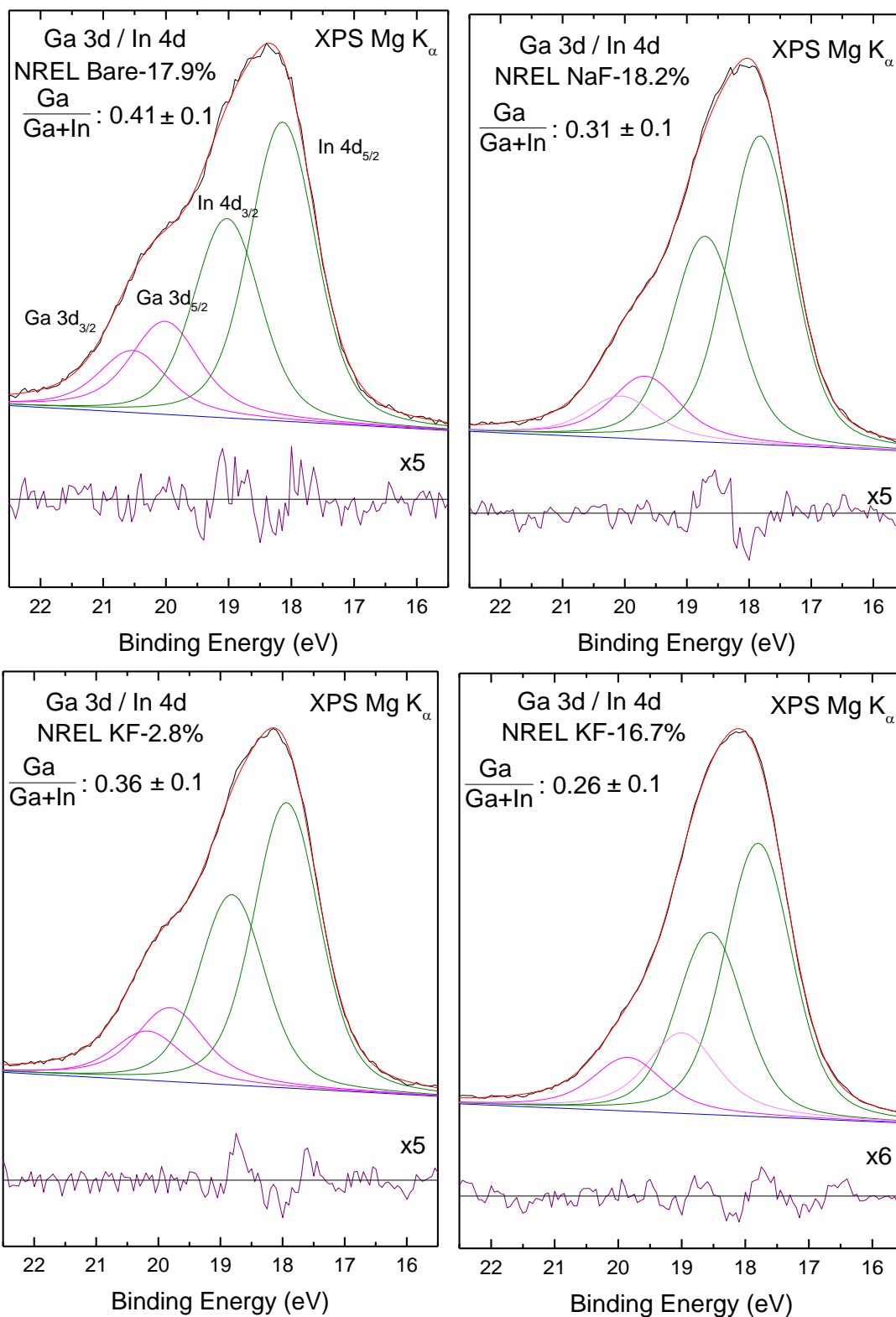


Figure 4.5: XPS detailed spectra of the Ga 3d / In 4d region of the NREL bare absorber (top left), NaF-treated absorber (top right), and low and high efficiency KF-treated absorbers (bottom left and right).

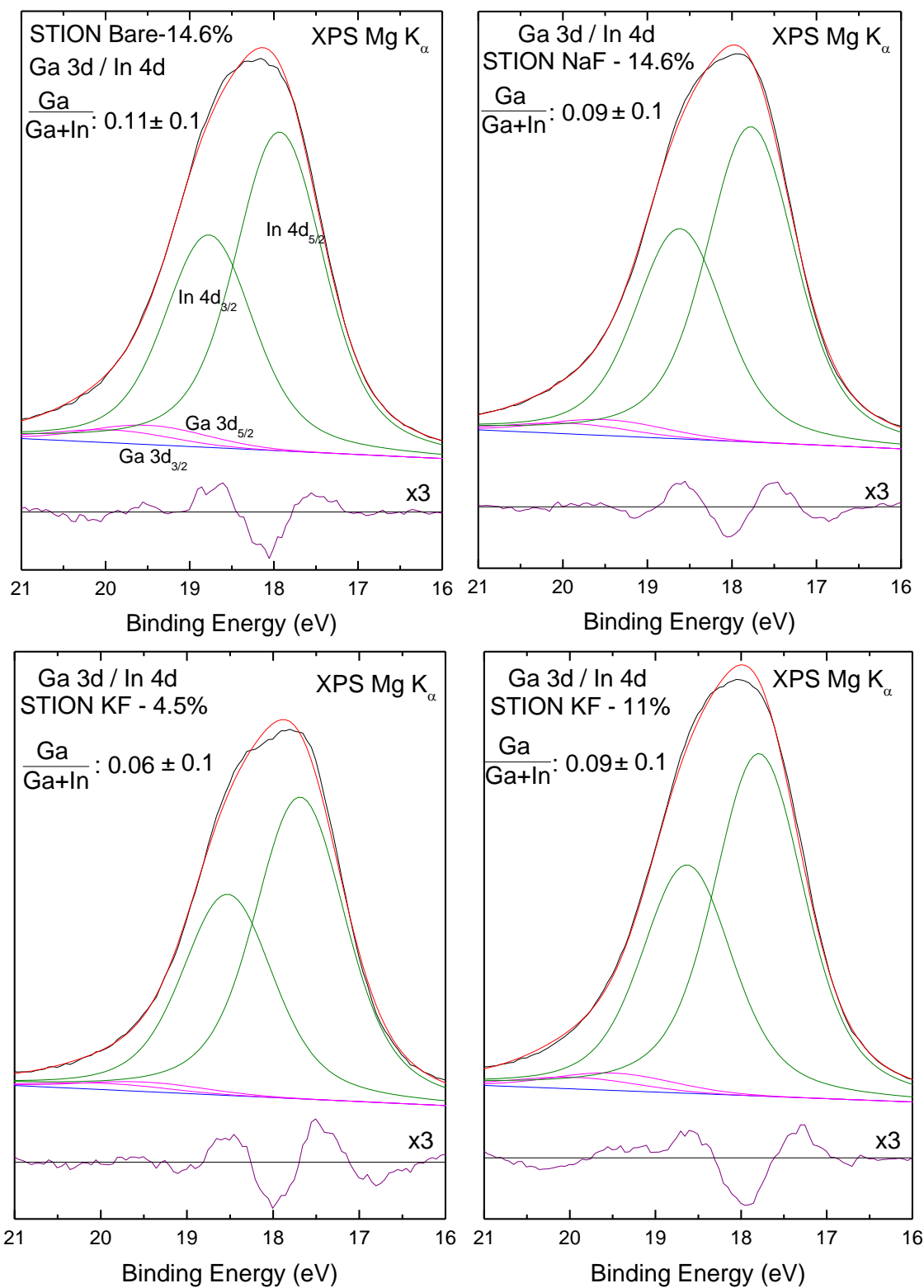


Figure 4.6: XPS detailed spectra of the Ga 3d / In 4d region of the STION bare absorber (top left), NaF-treated absorber (top right), and low and high efficiency KF-treated absorbers (bottom left and right).

treatments for the NREL absorbers. The NREL bare absorber has a Ga/(Ga+In) of 0.41 ± 0.10 eV. Visually, it is apparent there is more Ga at the surface due to the shoulder at ~ 20 eV being larger than the shoulder seen for the other NREL absorbers. The high efficiency KF-treated NREL absorber has the lowest Ga/(Ga+In), 0.26 ± 0.10 eV, and the low efficiency KF-treated NREL absorber has the largest Ga/(Ga+In) ratio (among the rinsed absorbers), 0.36 ± 0.10 eV. The Ga/(Ga+In) of the NaF-treated NREL absorber is 0.31 ± 0.10 eV. There is less of a change in the Ga/(Ga+In) for the STION absorbers, as seen in Figure 4.6. The fits themselves are also of a lower quality as seen in the residual (note the magnification factors) due to the very small Ga content on the surface. The addition of more components with the fixed boundary conditions did not further enhance the residual. The STION bare absorber has a surface Ga/(Ga+In) ratio of 0.11 ± 0.10 eV and the ratio for the treated STION absorbers do not really deviate from the bare absorber ratio. Both the NaF and high efficiency KF-treated STION absorbers have a Ga/(Ga+In) of 0.09 ± 0.10 eV and the low efficiency KF-treated absorber has a Ga/(Ga+In) of 0.06 ± 0.10 eV. While there is a larger difference in the Ga/(Ga+In) ratios of the treated NREL absorbers in comparison to the untreated absorber, the Ga/(Ga+In) ratios for the STION absorbers are essentially the same.

The Se 3d peak normalized to the In 3d_{5/2} peak area is shown in Figure 4.7, right, while the Se 3s and S 2s are shown on the left. The STION absorbers exhibit a more Se-poor surface relative to the NREL absorbers. Both the STION and NREL low efficiency KF-treated absorbers have the highest Se:In ratio, i.e. the surface is more Se-rich. There is a small component at ~ 59 eV present for the STION absorbers but not for the NREL absorbers. This component is indicative of SeO_x being present on the STION absorber

surfaces. Both NaF and high efficiency KF-treated absorbers shift toward lower binding energy while both low efficiency KF-treated samples shift towards higher binding energies. On the right of the figure, the Se 3s and S 2s peaks are normalized to the Se 3s of the respective sample sets. This normalization allows variations in the S:Se ratio in the STION samples (no S is expected in the NREL absorbers) to be seen along with shifts in the peaks. The peak shifts seen for the Se 3s follow the same pattern as discussed above for the Se 3d. The S:Se ratio for the STION absorbers clearly change as a function of alkali-treatment. The lowest S:Se ratio is seen for the low efficiency KF-treated sample

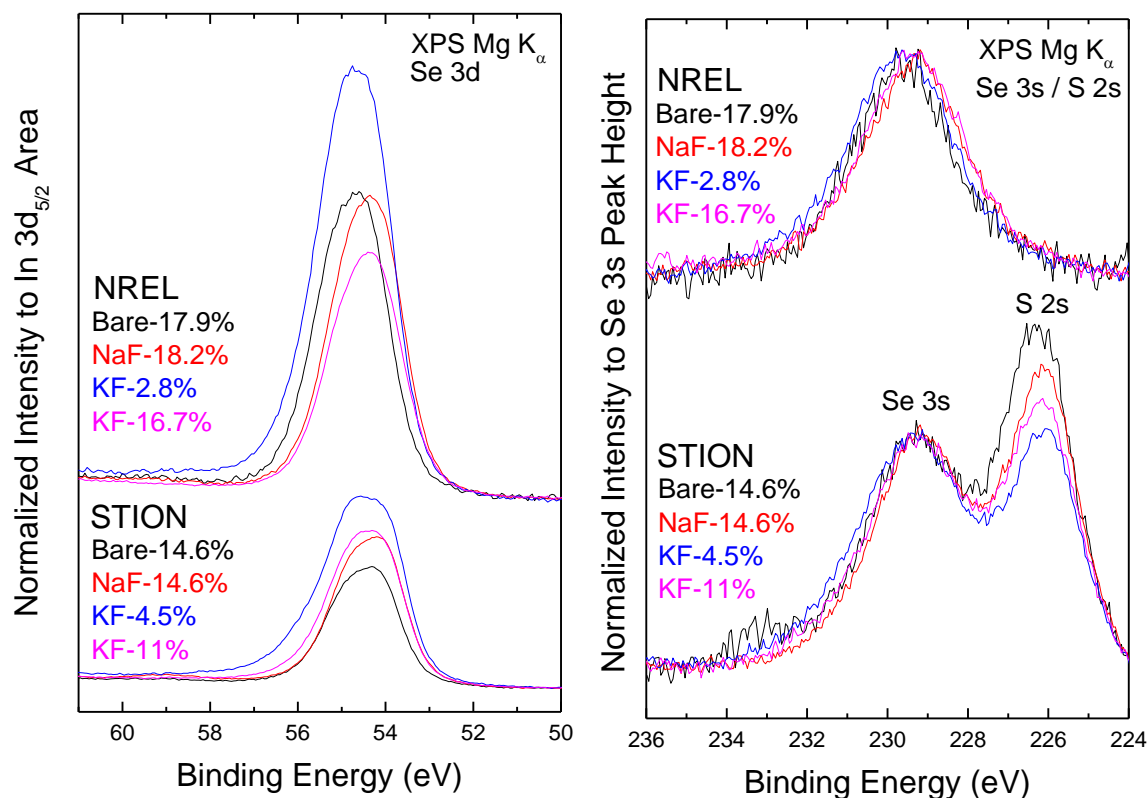


Figure 4.7: XPS detailed spectra of the Se 3d peak normalized to the In 3d_{5/2} peak area (left) and to Se 3s peak height (right) of the NREL and STION bare absorbers (black), NaF-treated absorbers (red), and low and high efficiency KF-treated absorbers (blue, pink). The S 2s peak intensity for the STION absorbers changes as a function of alkali-treatment.

and the highest is seen for the bare absorber. The NaF-treated absorber has a higher S:Se ratio than the high efficiency KF-treated sample. The spectra indicate that alkali-treatments of sulfur-containing chalcopyrites inherently changes the surface S:Se ratio.

Detailed spectra, normalized to peak height, of the In $3d_{5/2}$ (left) and the In MNN (right) are presented in Figure 4.8. The alkali-rinsing for both the STION and NREL samples shifts the In peak towards lower BE with the STION KF-4.5% and NREL NaF-18.2% samples shifted the most. The shift suggests a reduction of an In-oxide species. The STION bare absorber is shifted 0.20 eV towards lower BE relative to the NREL bare absorber suggesting the STION bare absorber contains less surface In-oxide species

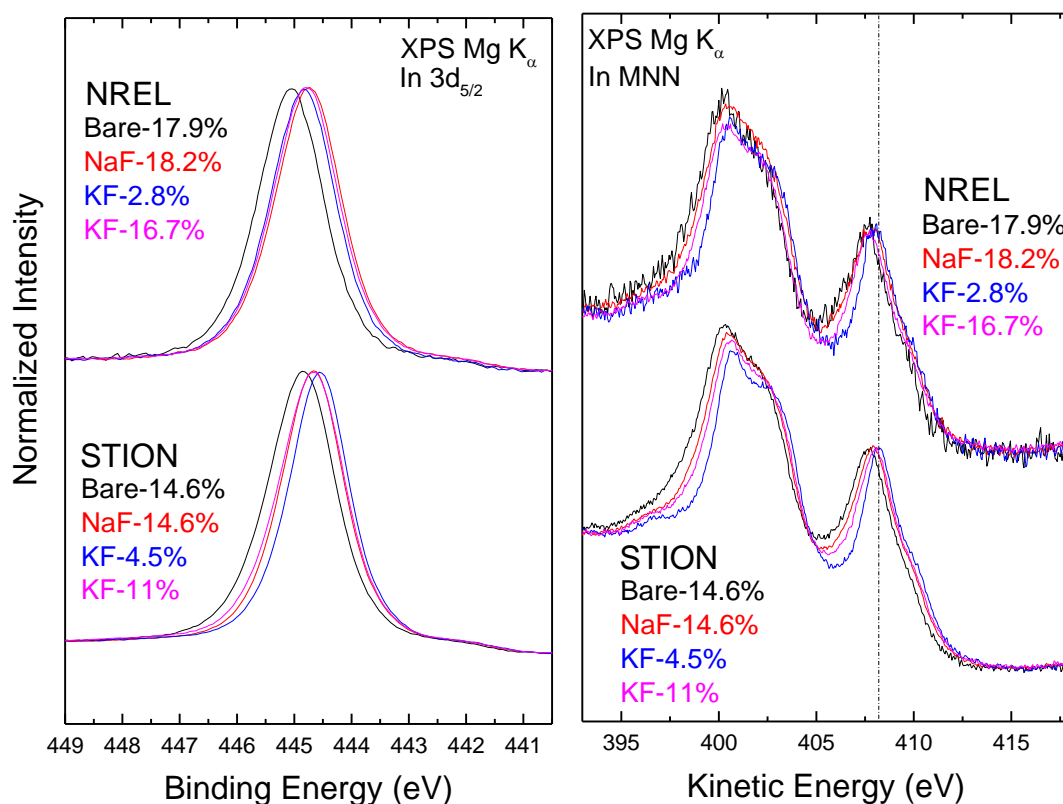


Figure 4.8: XPS detailed spectra of the In $3d_{5/2}$ peak (left) and the In MNN (right) normalized to peak height of the NREL and STION bare absorbers (black), NaF-treated absorbers (red), and low and high efficiency KF-treated absorbers (blue, pink).

than the NREL bare absorber. Analyzing the In MNN peak reveals that indeed, there is a reduction of In-oxide with the alkali-treatments. The added intensity on the In MNN shoulder at ~398 eV and the depth of the dip at ~405 eV shows this. The STION and NREL absorbers exhibit the most shallow dip with the NREL absorber a bit more shallow. With the alkali-treatment for both sets of samples, there is a reduction in the shoulder at ~398 eV, the dip at ~405 eV becomes deeper, and there is a reduction in the peak broadening. While the NaF and high efficiency KF-treated samples have similar surface In-oxidation, both low efficiency KF-treated samples have the least.

There has been some question as to whether K residue is left on the absorber surface after a KF-treatment. In fact, it can be seen with both the NREL and STION

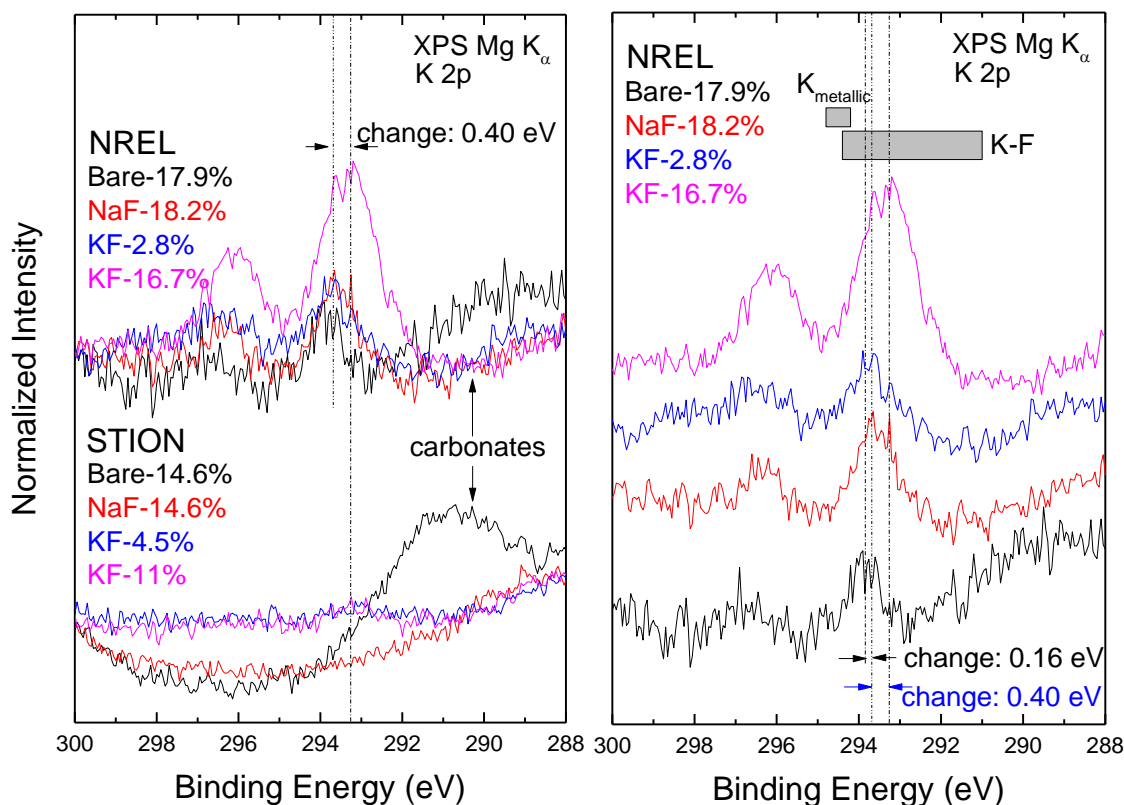


Figure 4.9: XPS detailed spectra of the K 2p peak (left). A closer look at the K 2p for the NREL absorbers is shown at the right along with K references.

absorbers in Figure 4.9, that indeed there is K deposited on the surface of not only all the KF-treated absorbers, but also the NaF and bare NREL absorbers. However, the K residue concentration is different between the STION and NREL absorbers, with the STION KF-treated absorbers having a significantly lower concentration of K on the surface relative to the NREL absorbers. It has been reported for the EMPA record absorber that the K deposited on the surface causes the Cu depletion¹⁰. While the data for the NREL absorbers show a considerable amount of K deposited and Cu depletion on the surface (except KF-2.8%), the data for the STION absorbers do not follow the same trend. There are trace amounts of K on the surface and an increase in the Cu peak. Th

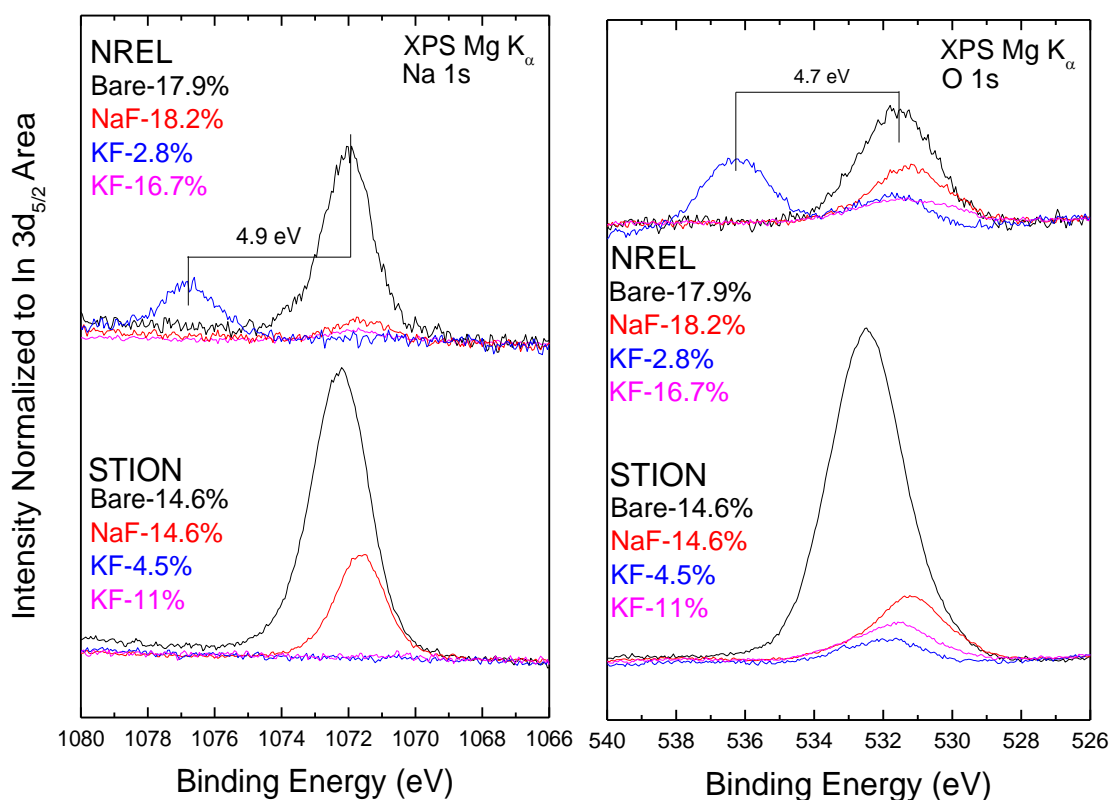


Figure 4.10: XPS detailed spectra of the Na 1s (left) and O 1s peaks (right) normalized to the In_{5/2} peak area of the NREL and STION bare absorbers (black), NaF-treated absorbers (red), and low and high efficiency KF-treated absorbers (blue, pink).

e NREL high efficiency KF-treated absorber has the largest K signal and is shifted 0.4 eV towards lower BE in comparison to the NREL bare absorber (right figure). Likewise, the K 2p peaks are shifted 0.16 eV towards lower BE. Despite the shift, the BE of the K peaks indicates a K-F bonding environment¹¹¹.

Shifting attention to Na and O, Figure 4.10 (left) shows the presence of Na on all four NREL absorbers as well as the STION bare and NaF-treated absorber. While both the NREL and STION bare absorbers have the largest Na peaks in their respective sets, the STION bare absorber has a larger Na 1s peak than the NREL bare absorber. The Na peaks for both NaF absorbers shift toward lower BE. The O 1s peak (right) shows a significantly high intensity for the STION bare absorber and amongst the rinsed samples, both NaF absorbers exhibit the largest O 1s peak. As well, the O 1s peak of all the rinsed samples are shifted towards lower BE, with both NaF-treated absorbers shifted the most. The O 1s peak is broad and asymmetrical indicating multiple O species, including hydroxides, which is not unexpected due to the nature of the KF and NaF PDT treatments. Both low efficiency KF absorbers have an additional component at ~537 eV, indicative of H₂O¹¹¹. The Na peak for the low efficiency NREL KF absorber exhibits a drastically shifted Na peak (almost 5 eV) in both the core-level and Auger (not shown) spectra indicating a different chemical species present. Although both the O and Na peaks for the NREL low-efficiency KF absorber are shifted ~5 eV towards higher BE, the shifts are not necessarily mutually exclusive, especially since the BE of the O 1s peaks indicates the presence of H₂O on the surface. In order to further investigate the chemical environment of Na for all the absorbers, a modified Auger parameter plot was constructed¹¹⁶ and is shown in Figure 4.11. A modified Auger parameter plot aids in identifying potential

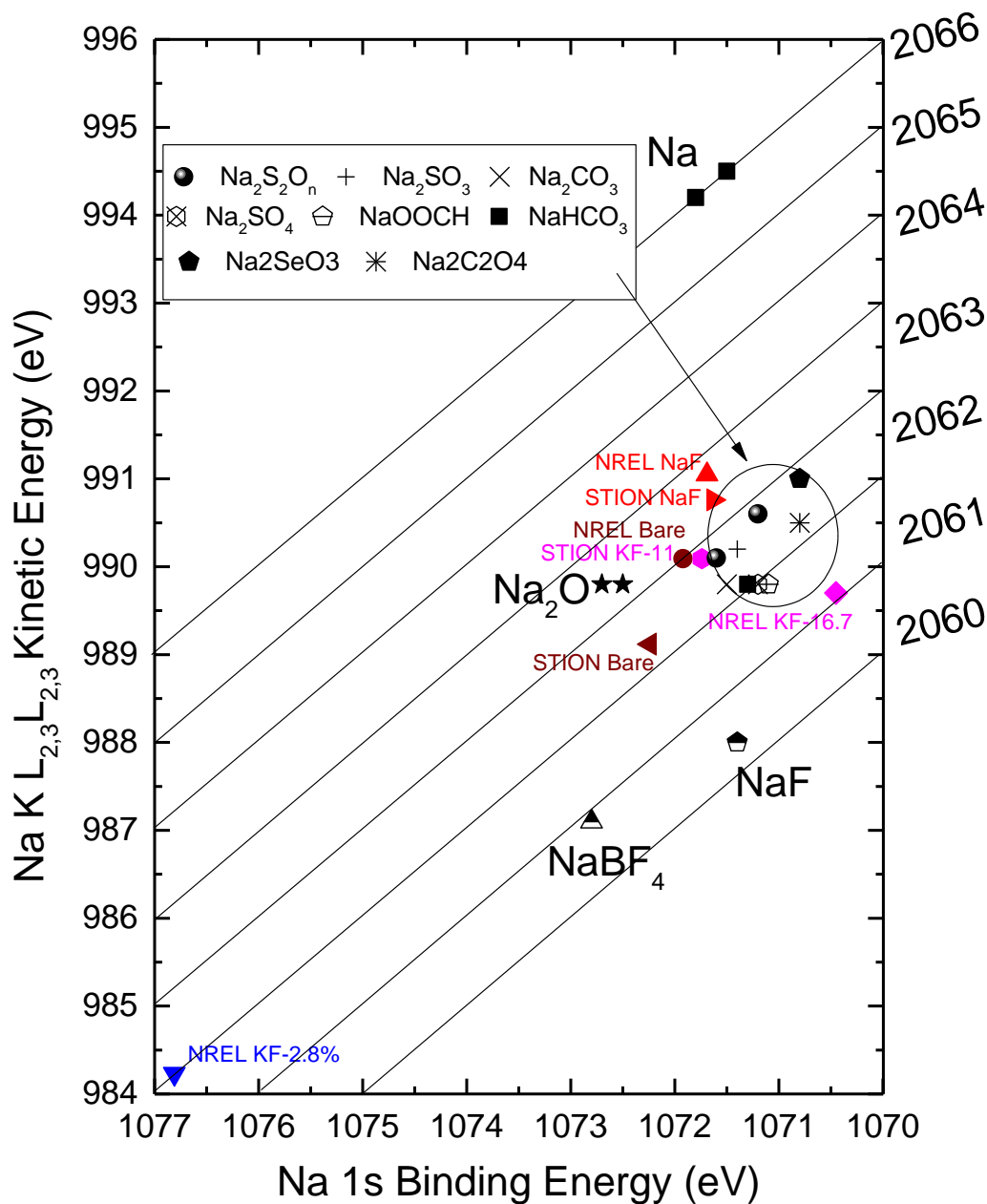


Figure 4.11: Modified Auger Parameter plot of Na 1s and Na KLL. The ion treated data are shown in red with references (111,112) in black.

species using both the Na KLL and Na 1s peak separation. All of the absorbers, except NREL KF-2.8%, are clustered between the Auger parameters 2061 and 2063 along with all of the Na-oxide species. It is clear that the Na on the absorbers are not metallic. The NREL KF-2.8% absorber has an Auger parameter (2061.5) that is similar to the STION

bare absorber and references NaHCO_2 , NaOOCH , and Na_2SO_4 indicating that these are possible chemical environments for these two absorbers. The Auger parameter plot shows that the Na on all of the absorber surfaces exhibits some Na-O bonding.

In order to investigate the possibility of Na-F bonding on the surface, the detailed region of the F 1s peak (left) and the F KLL region (right) are presented in Figure 4.12. F is detected on the surface of the STION bare and NaF-14.6% absorbers while no F is detected for the remaining absorbers. While it appears that there is only one species of F on the STION NaF absorber, there appears to be at least two species of F on the STION bare absorber. The binding energy of the F on the NaF absorber indicates that the F is in

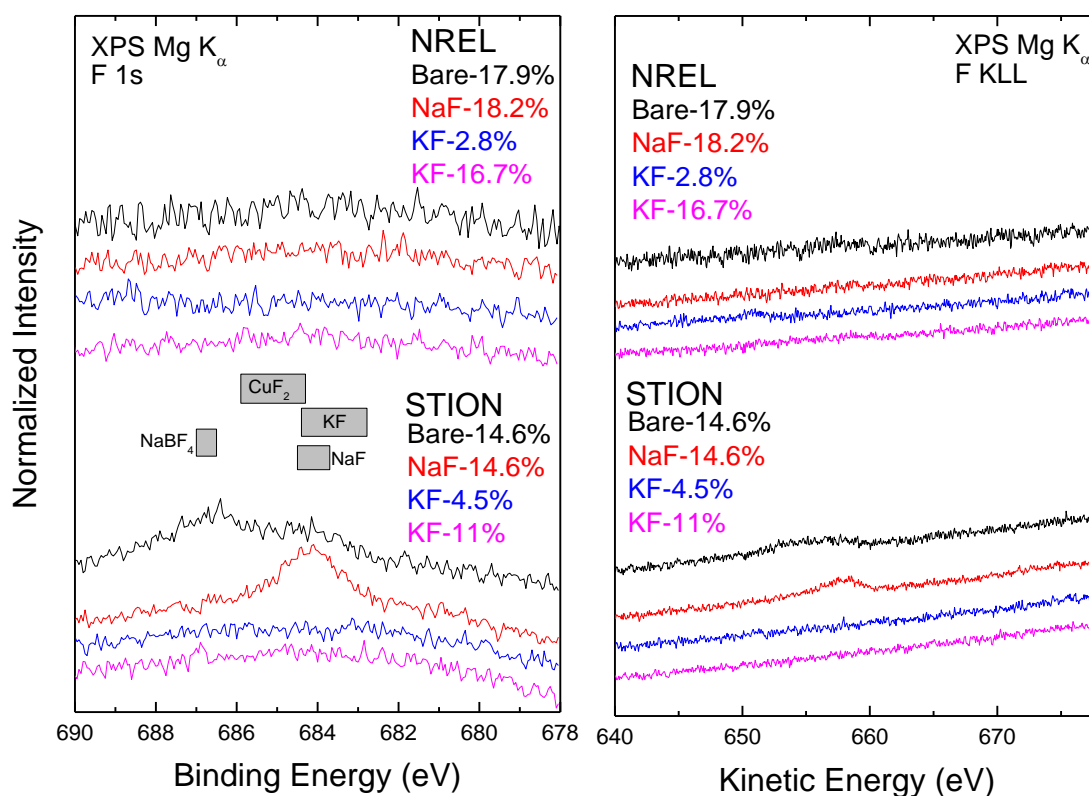


Figure 4.12: XPS detailed spectra of the F 1s (left) and F KLL (right) peaks of the NREL and STION bare absorbers (black), NaF-treated absorbers (red), and low and high efficiency KF-treated absorbers (blue, pink).

a Na-F and/or K-F chemical environment while the binding energy of the second F species on the STION bare absorber (~687 eV) suggests the possibility of a NaBF_4 species on the absorber. This indeed could be possible since B is detected on the surface of the STION bare absorber. In fact, a closer look at the spectra show that not only is there a B contamination, but a Zn contamination as well. Figure 4.13 presents the Zn 2p region of the NREL absorbers (left) and the STION absorbers (right). The detailed spectra for the NREL absorbers show that Zn is found on the surface of both the KF treated samples, with the most amount on the high efficiency KF absorber. The same trend is also seen for the STION absorbers, where Zn is found on both the KF absorbers with the high efficiency KF absorber have the largest amount. The fact that both Zn and B are detected

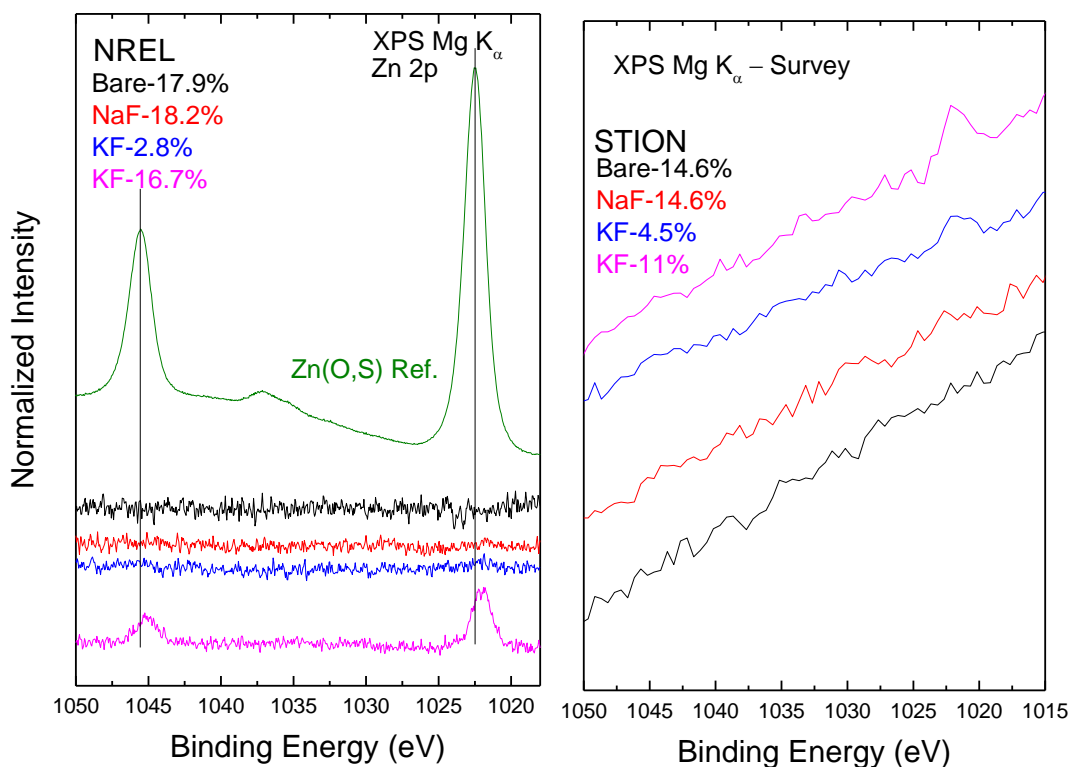


Figure 4.13: XPS spectra of the Zn 2p peaks for the NREL (left) and STION (right) bare absorbers (black), NaF-treated absorbers (red), and low and high efficiency KF-treated absorbers (blue, pink).

on some of the absorbers in the sample sets does not indicate that there is only one source of contamination. In fact, because the Zn is only detected on all four KF-treated absorbers, it suggests that the Zn contamination is coming from the KF post-deposition treatment of the CIGSe absorbers. Recall that both the STION and NREL absorbers are alkali-treated in similar fashions at NREL. The B contamination, on the other hand, is only found on the STION bare absorber. It is also possible that there was B on the other three STION absorbers but was rinsed off with the alkali-treatment. The STION bare absorber, however, was not rinsed. Indeed, the presence of both Zn and B on a few of the absorbers indicates that there are multiple sources of contamination in the deposition process of the absorber (B) and the alkali-treatments (Zn).

With a better understanding of the chemical structure on the absorber surfaces, a closer look into the electronic structure, notably the valence band, can take precedence. Figure 4.14 shows the UPS valence band spectra, taken with He II excitation, stacked to show shape changes (left) and separated to extrapolate a VBM (right). Both the NREL and STION absorbers show the least spectral intensity close to the VBM region while both low-efficiency KF absorbers exhibit a very large component at -3 eV (relative to E_F) that is attributed to Cu 3d-derived bands. The absence of the “Cu 3d” peak for both bare absorbers does not indicate the lack of Cu on the surface (Figure 4.2 shows there indeed is Cu) but the presence of surface adsorbates which broaden the valence band region²⁵, reflected in the derived VBMs. The VBM for the STION and NREL bare absorbers are -1.77 eV and -1.47 ± 0.10 eV, respectively. In contrast, the VBM for both low-efficiency KF absorbers is located much closer to E_F with -0.41 ± 0.10 eV for the STION absorber and -0.47 ± 0.10 eV for the NREL absorber. This is not surprising as the surface of these two

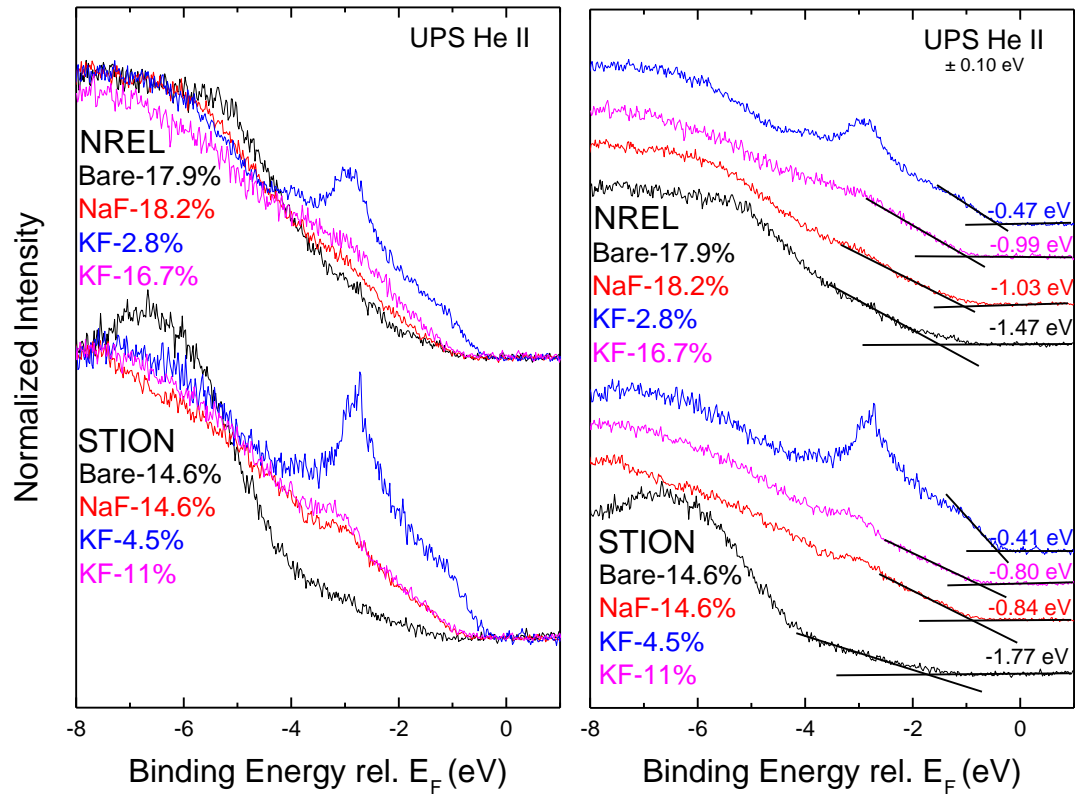


Figure 4.14: UPS spectra taken with He II excitation of the NREL and STION bare absorbers (black), NaF-treated absorbers (red), and low and high efficiency KF-treated absorbers (blue, pink).

absorbers are not only Cu-rich, but also exhibit the largest Se:In ratio on the surface. The consequence of Cu-Se metallic phases on the surface would be a VBM closer to E_F in comparison to a Cu-poor chalcopyrite surface. The NaF and high-efficiency KF absorbers of both sets are more similar to each other in terms of spectral intensity near the VBM region as well as the extrapolated VBM. The STION NaF and high-efficiency KF absorbers have a VBM of -0.84 and -0.80 ± 0.10 eV while the NREL NaF and high-efficiency KF absorbers have a VBM of -0.99 and -1.03 ± 0.10 eV. These values are similar to previously published high-efficiency CIGSe VBM values ^{25,51,60,85,86}.

While utilizing both XPS and UPS is advantageous to investigate the surface of the samples, XES offers a look deeper into the bulk. Figure 4.15 presents the XES spectra of the S $L_{2,3}$ emission excited non-resonantly with an excitation of 180 eV for all four STION absorbers. On the left, the spectra are displayed to compare spectral shape to each other and the references above while on the right, the spectra are stacked to show changes in intensity between the absorbers. The KF-4.5% absorber has the largest S $L_{2,3}$ emission while the NaF-14.5% has the lowest. This is contrary to the XPS measurements showing that the KF-4.5% had the least amount of S present on the surface in the set. This suggests that the alkali-treatments are etching off S on the surface (corroborated by XPS). In addition, there could also be a S gradient in the absorber independent of the alkali-treatments. The STION bare absorber shows the most S on the surface (XPS), however in the bulk (XES), it has less S than both KF absorbers. All four absorbers exhibit similar characteristic features at ~154, 155, and 159 eV. Comparing the spectral shapes to the reference spectra, the S in all four samples is predominantly bound to Cu and In forming $CuInS_2$. To take a closer look at changes between the bare absorber and the alkali-treated absorbers, the normalized bare absorber S $L_{2,3}$ emission spectra can be subtracted from the treated absorbers and the resulting residual can be analyzed. Figure 4.16 shows the residuals of subtracting the weighted bare absorber spectrum from the alkali-treated spectra and a comparison of the residual components to references. The weight of the bare absorber was chosen so the resulting residual did not have negative values. All three residuals show that there is indeed another species not evident in the bare absorber. In fact, the two KF-treated absorbers have an additional species different

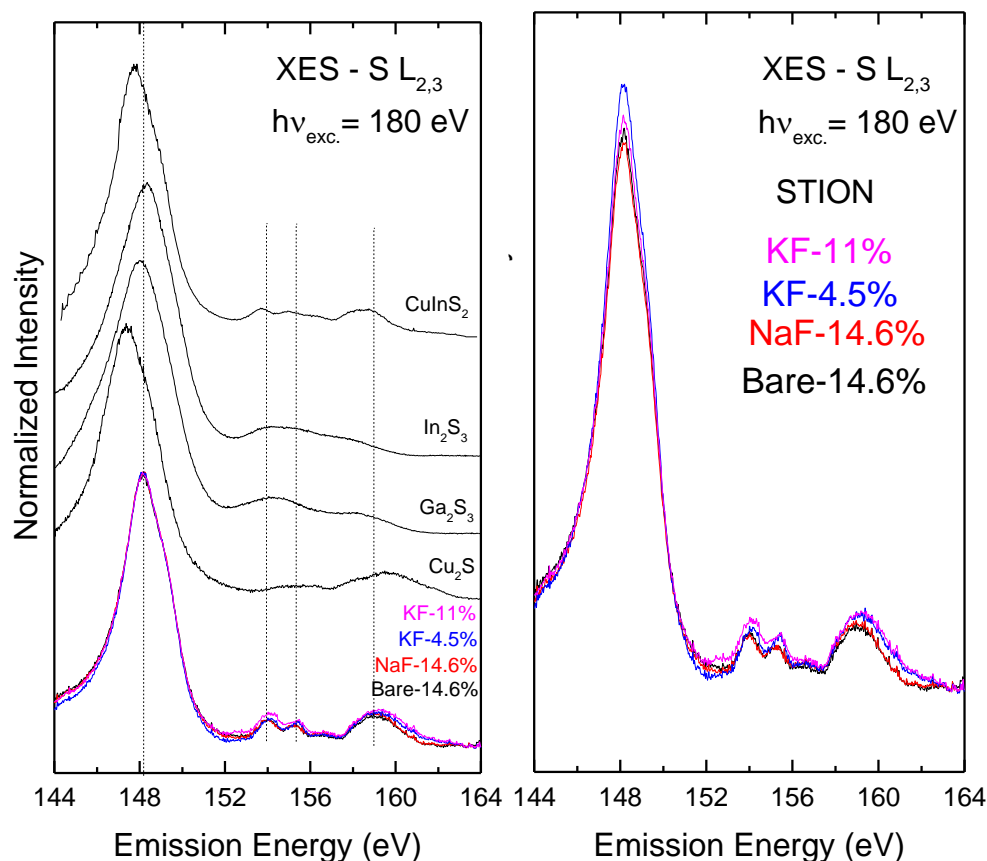


Figure 4.15: XES emission spectra excited nonresonantly with 180 eV of the S $L_{2,3}$ region for the STION bare (black), NaF-treated (red), and low and high efficiency KF-treated absorbers (blue, pink). Reference spectra are provided for comparison.

from the species found for the NaF absorber. The components at ~154, ~155, and ~160 eV for the KF spectra are indicative of sulfates in the absorber. The emission energy of the main S 3s peak (~148 eV) suggests an additional In_2S_3 and/or Ga_2S_3 species not apparent in the bare absorber spectrum.

XES measurements of both K $L_{2,3}$ and F K_{α} can be used to determine whether there is K and/or F in the bulk of the sample. The emission spectra of K $L_{2,3}$ (left) and F K_{α} (right) are presented in Figure 4.17 for the STION and NREL absorbers. The K $L_{2,3}$ emission spectra show the same trends as seen on the surface: the NREL KF-treated

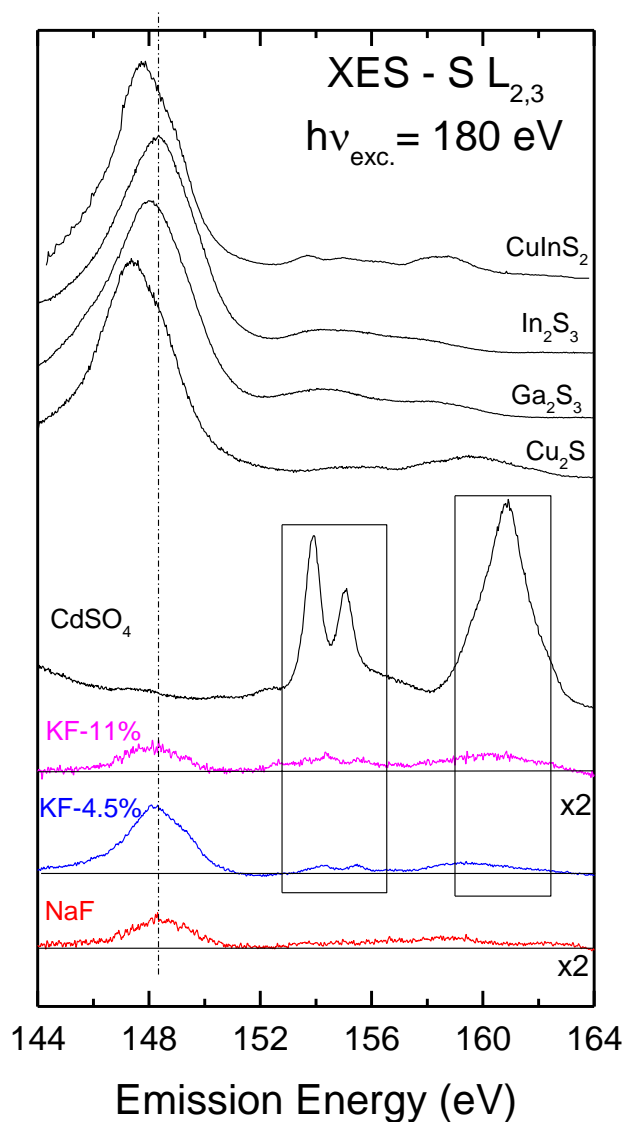


Figure 4.16: Relative weights of the STION bare absorber spectrum was subtracted from the alkali-treated absorber spectra and the resulting residuals are presented with reference spectra. Multiplication factors shown.

absorbers have a larger amount of deposited K in comparison to the STION absorbers. The F K_{α} , on the other hand, indicates that there is F found in the bulk of all the samples. XPS shows that F was also detected for both the STION bare and NaF-treated absorber, however XES shows the presence of F for all eight absorbers. In fact, all four NREL absorbers, especially the bare absorber, have a larger F K_{α} intensity than the STION

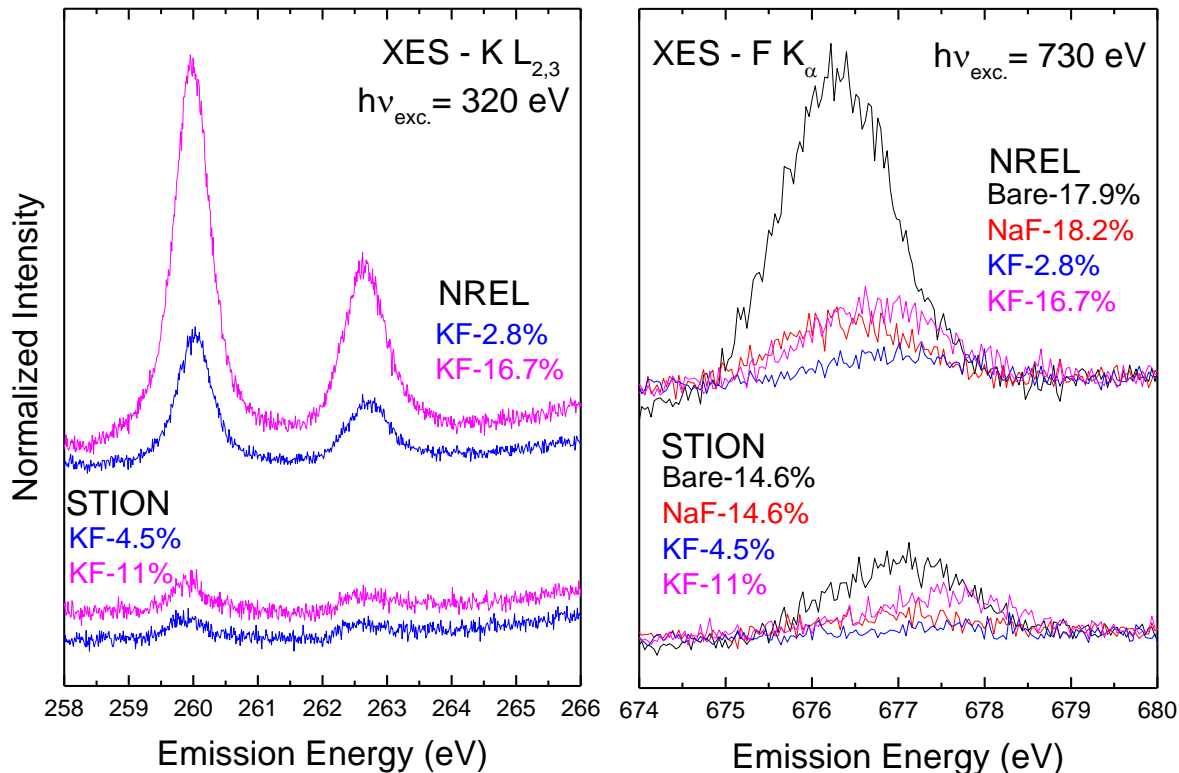


Figure 4.17: XES emission spectra of the K $L_{2,3}$ (left) and F K_{α} of the NREL and STION bare absorbers (black), NaF-treated absorbers (red), and low and high efficiency KF-treated absorbers (blue, pink).

absorbers. Since the F is found on both the bare absorbers and the alkali-treated absorbers, it suggests that the F may not only be from the alkali-treatments, but also a contamination from the growth process of the absorber. Overall, the XPS, UPS, and XES data have shown that the effects of alkali-treatments on the STION absorbers are not the same as the NREL absorbers, although similar trends are seen within the respective sample sets. Indeed, while there is a lot of insight and research on alkali-treated laboratory-scale research thin-film photovoltaics, there is a need to include industry-grade photovoltaics in these efforts with hopes of increasing overall module conversion efficiencies.

4.4 - CONCLUSION

To summarize the findings on alkali treatments of both the NREL and STION CIG(S)Se absorbers, XPS, UPS, and XES were utilized to look at the chemical and electronic structure of these samples. XPS shows that there is a low Ga content at surface for all STION absorbers relative to NREL absorbers. The Ga/(Ga+In) ratio changes for the NREL absorbers with alkali-treatments, however, the ratio does not change with the STION absorbers. Both the STION and NREL low efficiency KF-treated absorbers have the largest Cu:In ratio. All the alkali-treated absorbers have a low or absent Na signal on the surface. The Na is shifted ~5 eV for the KF-2.8% absorbers, but the modified Auger parameter suggests that it is still in a Na-Oxide bonding environment. Reduced O and carbonate peak intensity on all Alkali-treated samples, with KF-2.8% showing a large O 1s peak at ~536 eV. F is seen in the bulk for all eight absorbers and at the surface of the STION bare and NaF absorbers. B, Zn, and F (bulk) peaks show that there are contaminants during the development of the absorber and/or the Alkali-treatments. The S/Se ratio varies for all STION samples; Bare absorber shows the highest S/Se ratio, while KF-2.8% shows the lowest. S in all STION absorbers is found mostly in a CuInS₂-like environment, with treated absorbers showing evidence of In-S and/or Ga-S bonding environments. Both STION KF-treated absorbers and all four NREL absorbers show K at surface and all four KF-treated absorbers have K in the bulk as well. Surface contamination: B 1s on STION bare absorber and Zn (XPS) on the surface of both NREL KF-treated absorbers. UPS shows that the STION bare absorber has VBM of 1.77 ± 0.10 eV (larger than expected), due to the presence of adsorbates and possibly B. The NREL bare absorber has VBM of 1.47 ± 0.10 eV, large also due to adsorbates. The STION and

NREL NaF-treated absorbers have a VBM at 0.84 ± 0.10 eV and 1.03 ± 0.10 eV, respectively, which is comparable to previously published data. The STION KF-11% absorber has a VBM comparable to the NaF absorber in this set: 0.87 ± 0.10 eV and the NREL KF-16.7% also has a similar VBM to the NaF absorber in respective set: 0.99 ± 0.10 eV. Both “low-efficiency” KF absorbers have similar VBM values to each other with the STION absorber at 0.47 ± 0.10 eV and the NREL absorber at 0.41 ± 0.10 eV. The VBM is located closer to the E_F than the other absorbers, likely due to not only the large Cu 3d band component at ~ 3 eV, but the large presence of Se on the surface (in comparison to the other absorbers), potentially creating CuSe_2 species.

CHAPTER 5

KF COEVAPORATION VS. KF POST DEPOSITION TREATMENT: SPECTROSCOPIC INVESTIGATION ON THE EFFECTS OF KF

5.1 – INTRODUCTION

With the inclusion of Na proving to be successful in chalcopyrite devices, research into the utilization of other alkali metals became of interest^{11,32–38,40,41,43,117–124}, especially after EMPA raised the CIGSe world-record efficiency to 20.4% (from 18.7% for flexible substrates and 20% for soda-lime substrates),^{10,103} and ZSW increased the record to 21.7% shortly after⁴². Both record efficiency devices utilized KF post-deposition treatment (PDT) as the method of incorporating K, but fundamental research is needed to further understand the role of K on the absorber and the buffer/absorber interfacial properties as a function of K deposition parameters in order to optimize conversion efficiencies.

It is well known that Na diffuses from the soda-lime glass into the chalcopyrite absorber^{34–38,122–125}, however it is not known how and if the Na diffusion affects the inclusion of K. For a more controlled inclusion of Na (K), a barrier is added to the glass before the Mo sputter treatment to prevent such diffusion^{123,126,127}. It is imperative to understand the full effects of K inclusion in the CIGSe device, especially as a function of deposition processes, along with possible Na diffusion effects.

5.2 – EXPERIMENTAL

The sample set consisted of five absorbers from NREL: two bare absorbers with and without a SiO₂ barrier, two KF-PDT treated absorbers with and without a SiO₂ absorber, and one CKIGSe absorber, for which KF was co-evaporated during the deposition of the

CIGSe absorber. The purpose of the SiO₂ barrier is to prevent alkali atoms from diffusing from the glass, thus allowing us to study how the KF PDT affects the CIGSe absorber. All absorbers were grown at 525 °C with constant elemental flux profiles (i.e., not with the NREL three-stage process) on a Mo-sputtered glass¹¹⁸. The efficiencies of corresponding devices range between 9.1% (CIGSe/SiO₂) and 15.5% (CKIGSe). At UNLV, the absorber surfaces were ion-treated for a total of 60 min using 50 eV Ar⁺ ions at low incidence angle. The samples were then rinsed with 100 mL H₂O + 12.5 mL NH₄OH at 65 °C in an inert environment (“rinsed” and “NH₄OH” will be used interchangeably in this chapter).

The absorbers were briefly exposed to air, packed, and vacuumed-sealed under dry nitrogen before being sent to UNLV. The samples were unsealed in the inert environment of our glove boxes, mounted, and introduced to the UHV system. XPS, UPS, and IPES were utilized to investigate the chemical and electronic structure of the NREL sample set. Mg K_α and Al K_α irradiation and a SPECS PHOIBOS 150 MCD electron analyzer were employed for XPS measurements while a He discharge lamp and He II excitation were employed for the UPS measurements. A custom-built Dose-type detector with a SrF₂ window and Ar:I₂ filling,⁸¹ along with a commercial low-energy electron gun (Staib), were used for IPES experiments. The spectra were calibrated using Auger and core-level peaks of clean Cu, Ag, and Au foils (XPS)⁸⁰ and the Fermi energy of a clean Au foil (UPS, IPES).

All peaks were analyzed by fitting the different spectral intensities with Voigt functions (with coupled Lorentzian and Gaussian widths) and a linear background using the Fityk peak-fitting program⁹⁰. The VBM and CBM were determined by linear extrapolation of the leading edge in the valence band (UPS) and conduction band (IPES)

spectra¹⁰⁹. The base pressure in the UNLV analysis chamber was better than 5×10^{-10} mbar.

5.3 – RESULTS AND DISCUSSION

Figure 5.1 shows the XPS Mg K_{α} survey spectrum taken on all five samples after ion-treatment (black) and NH_4OH rinse (red). All expected peaks (Cu, In, Ga, Se, Na) are present (no Na on ion-treated absorbers with SiO_2 barrier, as will be discussed later), along with adsorbates, C and O. All spectra were normalized to the In $3d_{5/2}$ peak in order to compare peak ratios to In. Detail spectra of the Cu $2p_{3/2}$ of the current sample set (left) and a comparison with a previous NREL alkali-treated sample set (chapter 4) are shown in Figure 5.2. It compares the effects of the rinse, KF-PDT, and co-evaporated KF on the

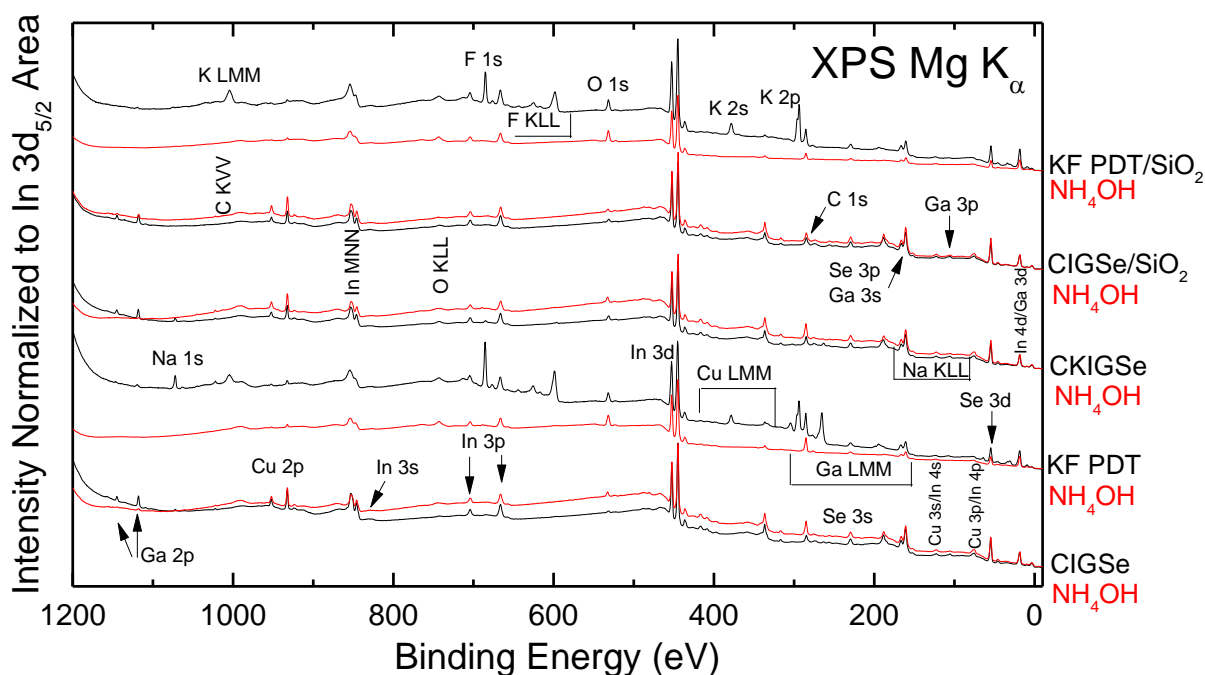


Figure 5.1: XPS Mg K_{α} survey spectrum taken of the NREL bare and KF-treated absorbers. The ion-treated surfaces are shown in black, while the rinsed surfaces are shown in red.

NREL samples, and also shows the differences between the 3-stage coevaporation process (bottom) and constant elemental flux (center, top). For the center and top spectra, normalizing the Cu $2p_{3/2}$ peak to the In $3d_{5/2}$ area, shows that there is a Cu depletion at the surface of both KF PDT absorbers that is still present after the ammonia treatment. The Cu depletion is also seen for the “high-efficiency” three-stage KF-PDT and NaF-PDT NREL absorbers (right). The Cu:In ratio from the 3-stage co-evaporation CIGSe absorber (“Bare-17.9%”) is much smaller than for the CIGSe absorber grown with constant elemental flux (left). The surfaces of the bare and CKIGSe absorber of the current sample set are not Cu-poor. After the rinse, the Cu:In ratio increases for the CIGSe/SiO₂ and

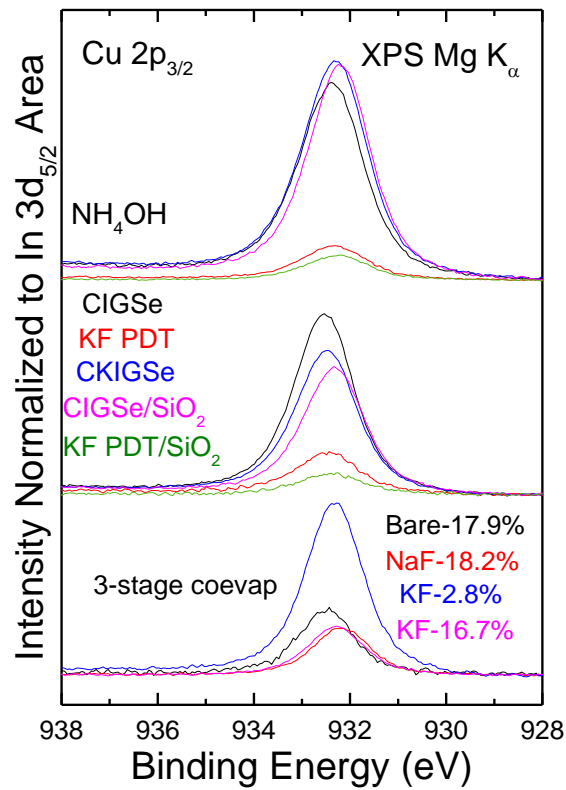


Figure 5.2: Detailed XPS Mg K_{α} spectra of the Cu $2p_{3/2}$ taken on the ion-treated (center) and NH₄OH treated (top) of the CKIGSe, both CIGSe, and both KF PDT absorbers. This is compared to a previous sample set, displayed on the bottom (four alkali-treated NREL absorbers, grown with the three-stage coevaporation process).

CKIGSe, but there is no change for the CIGSe absorber. All alkali-treated absorbers and the CIGSe/SiO₂ absorber are shifted towards lower binding energy (BE) in relation to the CIGSe. There is also no evidence for Cu-F or Cu-O species.

The detail spectra in Figure 5.3 present the Se 3d peak normalized to In 3d_{5/2} area (left) and peak height (right). When normalizing the Se 3d peak to the In 3d_{5/2} peak, it is clear that the KF PDT absorbers both have lower surface Se:In ratios. After the NH₄OH treatment, the Se:In ratio for the KF PDT absorbers reduce by almost half, while the ratio stays relatively constant for the CKIGSe and both CIGSe absorbers. There are also no Se-oxides on the surface, evident by the lack of a peak at ~ 59 eV. Normalizing the Se 3d to peak height, it is easier to see shape changes and shifts. In particular, the unrinsed

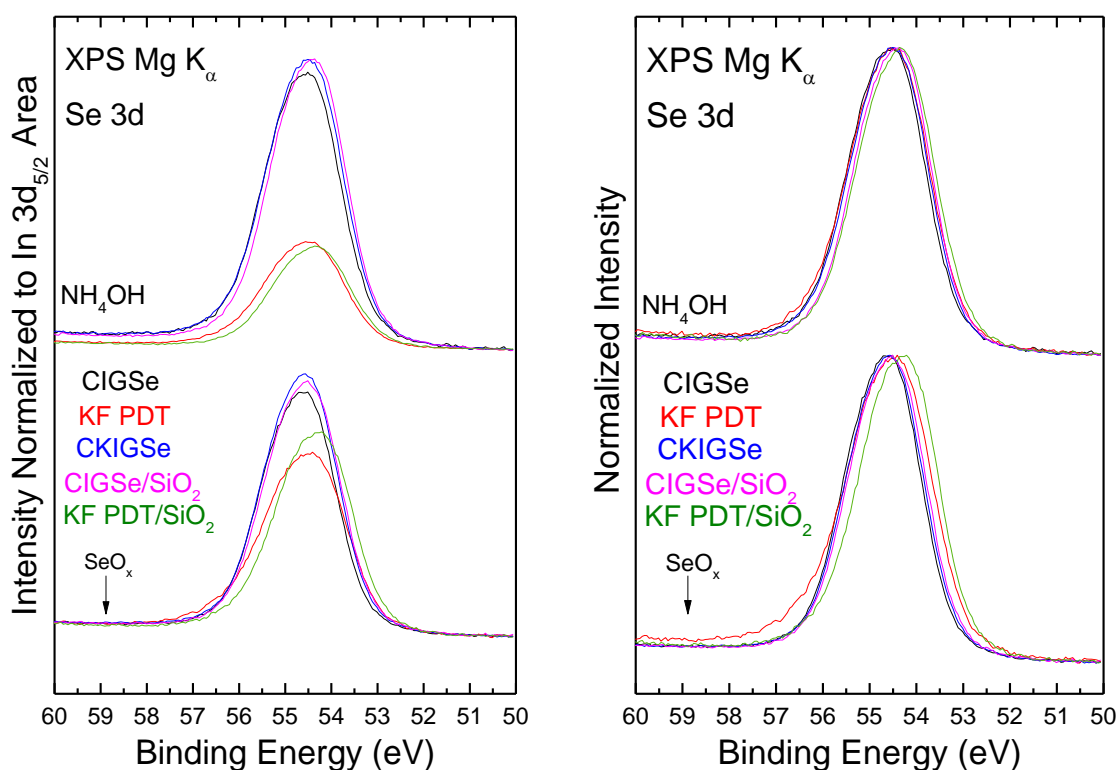


Figure 5.3: Detailed XPS Mg K_α spectra of the Se 3d region, normalized by In 3d_{5/2} area (left) and peak height (right). The ion-treated spectra are shown at the bottom, and the NH₄OH treated spectra at the top. The expected locations for oxide contributions are indicated.

KF PDT absorber exhibits a wider shape and a shoulder at 57 eV that is reduced with the NH_4OH treatment. References^{111,112} suggest a Se-C bonding environment, which is commensurate with the fact that this absorber shows the largest amount of C on the surface (as will be discussed later in conjunction with Figure 5.13). There is no evidence for the presence of a Se-O bonding environment on any of the absorber surfaces (SeO_x species would appear at ~59 eV). After rinsing, the Se 3d peaks for all absorbers shift slightly to lower binding energies.

The In 3d_{5/2} (left) and In MNN (right) regions exhibit unusual peak shapes for both KF PDT absorbers, as shown in Figure 5.4. The spectra are again normalized to peak

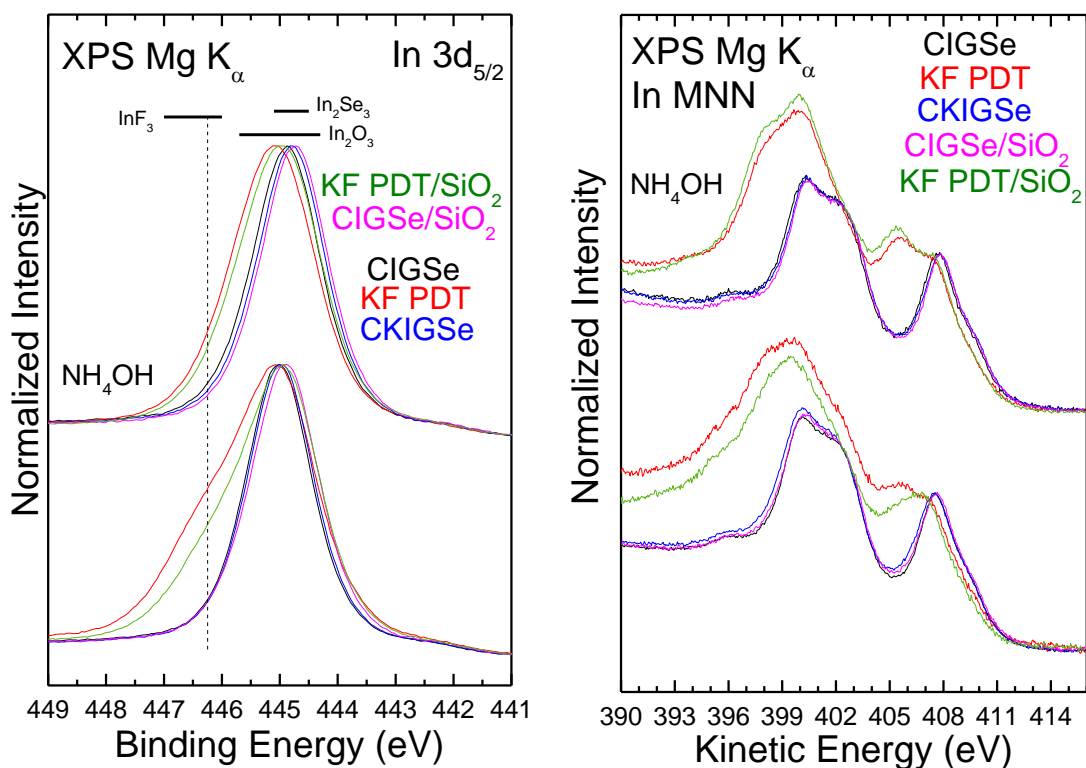


Figure 5.4: Detailed XPS Mg K $_{\alpha}$ spectra of the In 3d_{5/2} (left) and In MNN (right) regions, normalized by peak height. The ion-treated spectra are shown at the bottom, while the NH_4OH -treated spectra are at the top. The expected locations for oxide, selenide, and fluoride contributions are indicated.

height (in the case of the In MNN, the most prominent peak at ~408 eV was used). In XPS, both unrinsed KF PDT absorbers have a large shoulder at ~446.5 eV, suggesting the presence of an In-F bonding environment. These two peaks are also wider than those of the CKIGSe and both CIGSe absorbers, suggesting the presence of oxides as well. The NH_4OH treatment reduces the amount of In-F and shifts both KF PDT absorbers towards higher BE, while CKIGSe and both CIGSe absorbers shift toward lower BE, suggesting reduction of oxides, as will be discussed in more detail in the following.

The In MNN region is particularly useful to discern the presence of oxides, as it offers a more distinct peak position difference between In-Se and In-O bonding

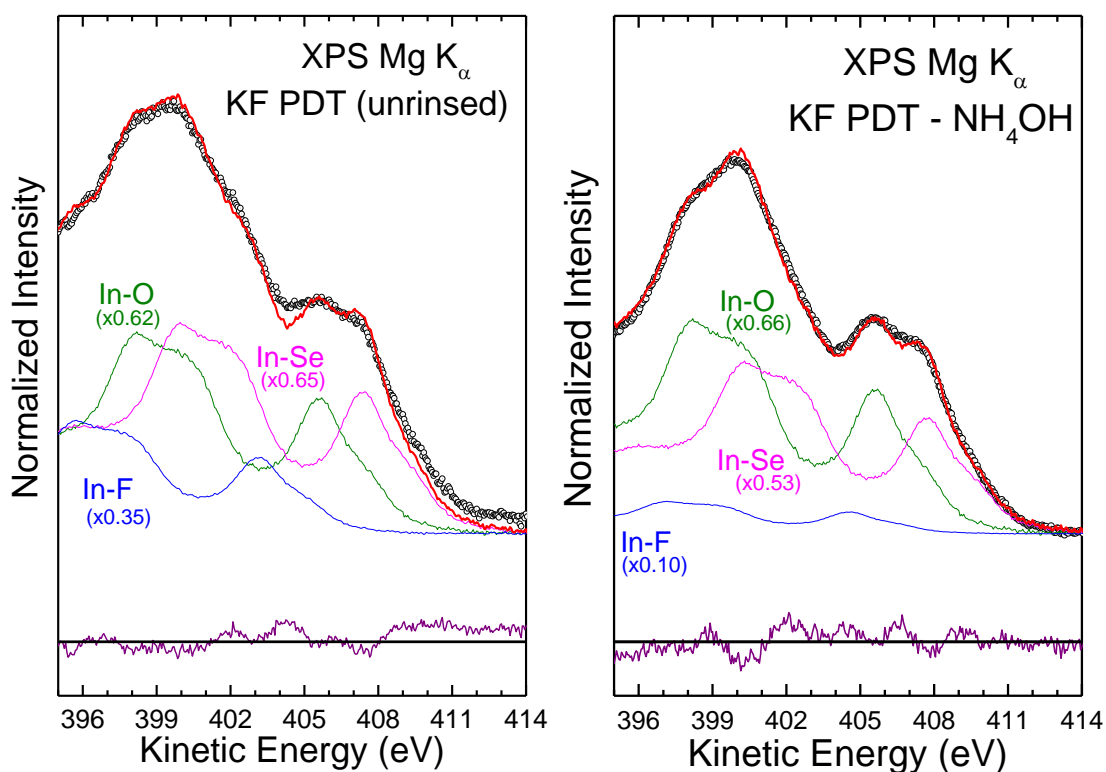


Figure 5.5: Detailed XPS Mg K_α spectra in the In MNN region, normalized by peak height, for the clean and rinsed KF PDT absorbers. Three In-Se references are used to fit the peaks to show contributions from In-F, In-O, and In-Se species. The residual is shown on the bottom in purple.

environments¹²⁸. The most striking feature is the overall shape of the In MNN peaks of both KF PDT absorbers in comparison to the other absorbers. Pre-rinse, the In MNN region for both KF PDT absorbers is a superposition of (at least) three species, most likely In-F, In-O, and In-Se bonding environments. After the NH₄OH treatment, we find a clear reduction in the In-F species (seen in both graphs). However, we also observe an increase in In-O species for both KF PDT absorbers, seen by the peak at ~405 eV. This peak is larger for the KF PDT/SiO₂ absorber (than for the KF PDT absorber), indicating the presence of more In-O species. Amongst CKIGSe and both CIGSe absorbers, the CIGSe shows the least amount of oxides, as seen by the deepest “dip” at ~405 eV. CKIGSe and CIGSe/SiO₂ both exhibit more shallow dips and a shoulder at ~399 eV. After the NH₄OH treatment, the dip is similar for these three absorbers, but slightly deeper for the CIGSe/SiO₂ absorber. This is also seen in the region 390-399 eV, where the spectral intensity is lower. The NH₄OH treatment removes/reduces oxides for CKIGSe and both CIGSe absorbers, but adds oxides to the surface of both KF PDT absorbers. In contrast, the NH₄OH treatment reduces the In-F species on the surface of these two absorbers, best seen in Figure 5.5. The In MNN spectra of the pre and post-rinse KF PDT absorber were fit with an In-Se reference (ion-treated CIGSe absorber), shifted to reflect contributions from In-O and In-F. After the rinse there is a clear decrease in In-F contributions (from x0.35 to x0.10) and increase in In-O (from 0.62x to 0.66x). The quality of the residual shows that three species can fit the spectra pretty well. Note, it is more difficult to fit a spectrum using other spectra than using functions hence a more poor residual is expected.

In addition to the presence of an In-F species on the surface of the KF PDT

absorbers, we find indications for the presence of a Ga-F species as well. Figure 5.6 shows survey spectra of Ga $2p_{3/2}$ (left) and Ga LMM (right). The Ga $2p_{3/2}$ peaks for both KF PDT absorbers are shifted $\sim 2\text{eV}$ towards higher BE, which corresponds to a Ga-F bonding environment. Normalizing the Ga $2p_{3/2}$ peak to In $3d_{5/2}$ shows that the Ga:In ratio is smallest for both KF PDT absorbers, and largest for the CIGSe absorber before the NH_4OH treatment. After the treatment, we find a Ga signal reduction at the surface for all the absorbers, most notably for the KF PDT absorbers. After the NH_4OH treatment, the CIGSe/ SiO_2 absorber surface shows the largest Ga:In ratio, albeit half of the original peak.

The Ga LMM peak shape gives a good indication for the presence of Ga-oxides.

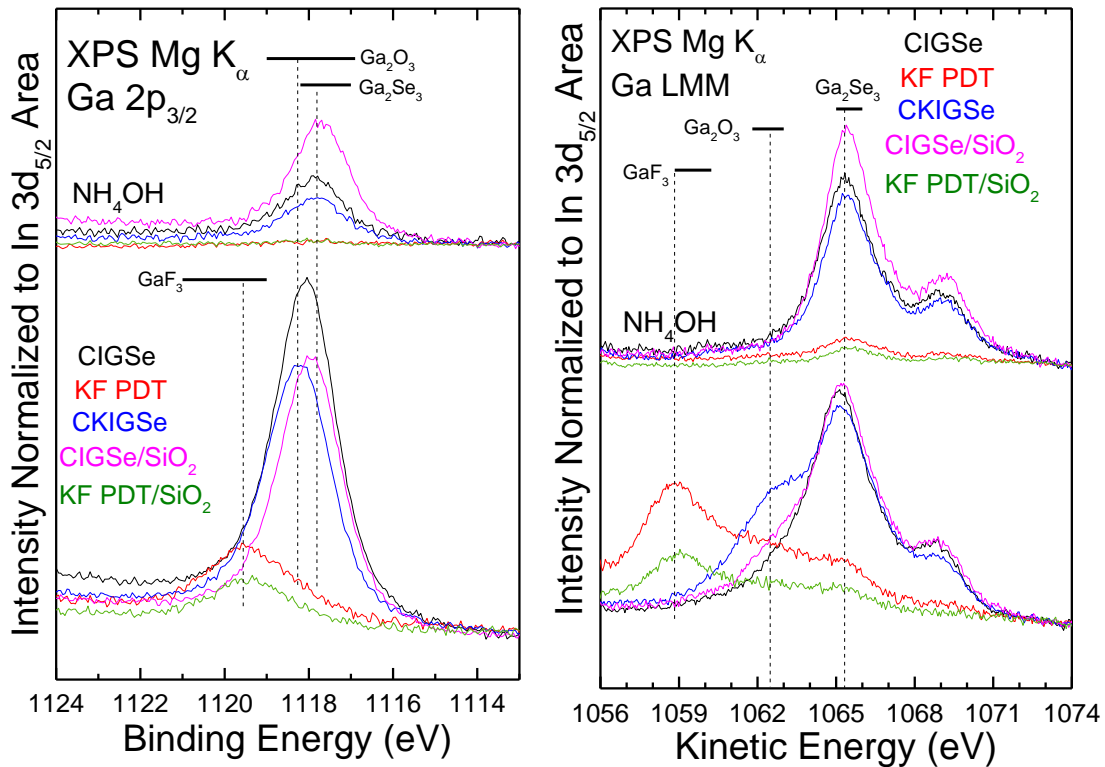


Figure 5.6: Detailed XPS Mg K_α spectra of the Ga $2p_{3/2}$ (left) and Ga LMM (right) regions, normalized by the In $3d_{5/2}$ area. The ion-treated spectra are shown at the bottom, while the NH_4OH -treated spectra are at the top. The expected locations for oxide, selenide, and fluoride contributions are indicated.

For instance, we observe an extra component at ~ 1062 eV for the unrinsed CKIGSe and CIGSe/SiO₂ absorbers that is removed after the NH₄OH treatment. The Ga LMM peaks for both KF PDT absorbers are shifted towards lower KE and the primary peak positions match that of Ga-F. After the NH₄OH treatment, the Ga LMM peaks are reduced, especially for the KF PDT absorbers. The Ga-O and Ga-F species are removed. The CIGSe/SiO₂ absorber shows the largest Ga LMM peak, similar to the Ga 2p_{3/2} peak.

The Ga 3d/In 4d region offers the opportunity to measure how the Ga/(Ga+In) ratio changes amongst the samples before and after the NH₄OH treatment, as depicted in

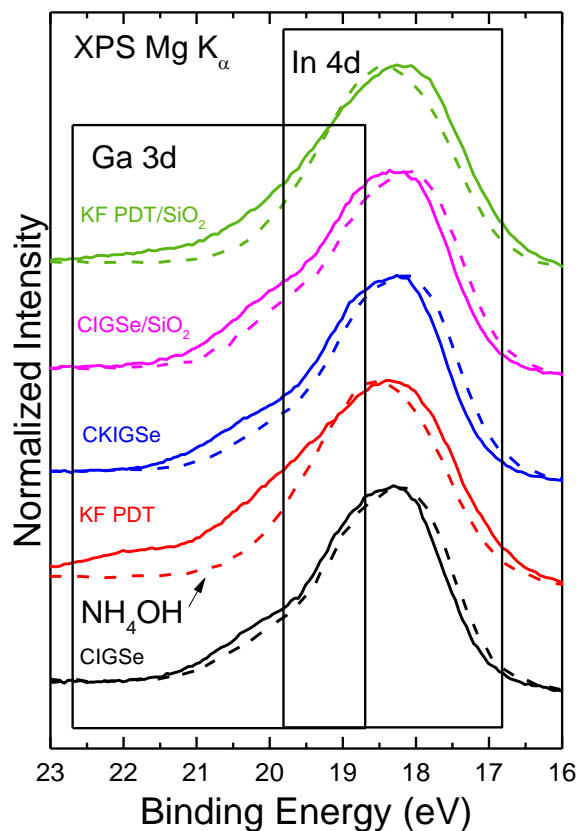


Figure 5.7: Detailed XPS Mg K_α spectra of the Ga 3d and In 4d region. The dotted spectra represent NH₄OH treated absorbers while the continuous line spectra represent the “clean” surfaces. Regions where Ga 3d and In 4d peaks are located are boxed.

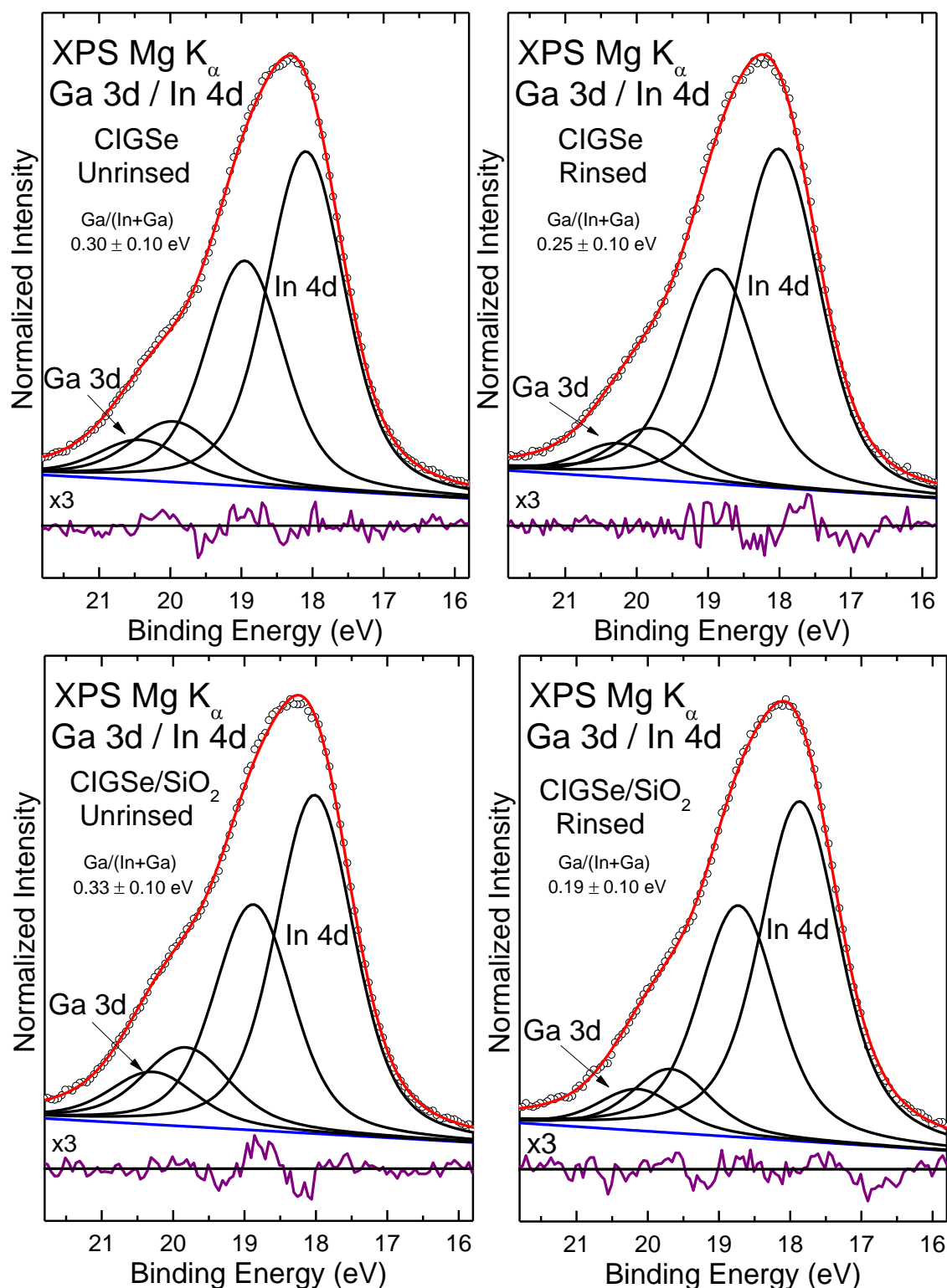


Figure 5.8: XPS detail spectra of the Ga 3d/In 4d of the pre and post-rinse CIGSe absorber (top) and CIGSe/SiO₂ (bottom). Fit curves for In:Ga contributions to the peak are shown along with their respective residuals (purple).

Figure 5.7. The unrinsed absorber spectra are plotted with a continuous line while the dotted spectra represent the NH_4OH treated absorbers. Clear changes are seen amongst the samples themselves and between pre-rinse and post-rinse spectra. The pre-rinse KF PDT and KF PDT/ SiO_2 spectra are broadest suggesting the presence of multiple species. After the rinse, the spectra are more narrow and shifted towards higher BE. The CIGSe, CKIGSe, and CIGSe/ SiO_2 absorbers exhibit more similar peak shapes and they all shift towards lower BE.

The In and Ga components to the spectra are shown by fitting the data. Pre-rinse and post-rinse fits for the CIGSe and CIGSe/ SiO_2 are shown in Figure 5.8, CKIGSe in Figure 5.9, and KF PDT and KF PDT/ SiO_2 in Figure 5.10. The peaks were fit with a linear

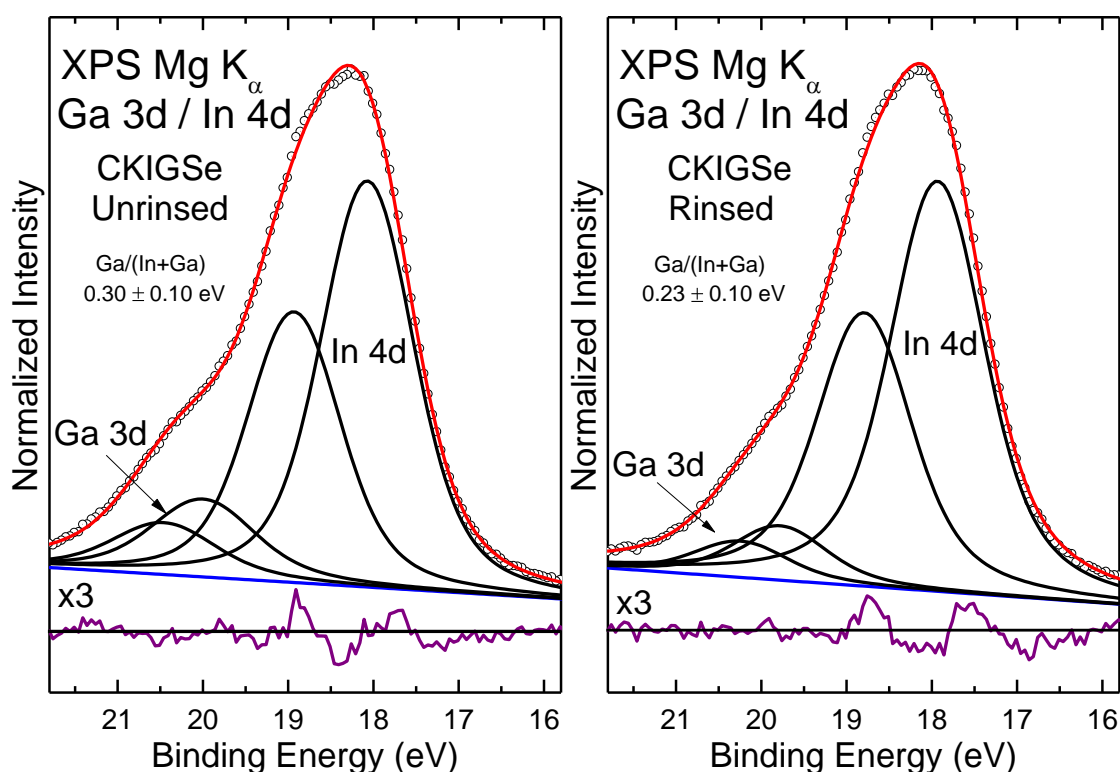


Figure 5.9: XPS detail spectra of the Ga 3d/In 4d region of the CKIGSe absorber pre-rinse (left) and post-rinse (right). Fit curves for In:Ga contributions to the peak are shown along with their respective residuals (purple).

background and Voigt profiles, using coupled Gaussian widths for all components, and coupled but separate Lorentzian widths for In and Ga, respectively. The ratios of the spin-orbit split peaks were fixed according to their multiplicity, along with their respective peak separation, 0.86 eV for In^{113,114} and 0.46 eV for Ga¹¹⁵. The data is shown with black dots, the In 4d and Ga 3d components in black, and the resulting fit in red for Figures 5.8 and 5.9. The residual of the fit is shown below each spectrum (purple). These shallow core levels already possess some band character, and thus the quality of the fit is very surprisingly high, especially given all the above-mentioned boundary conditions included in the fit. The surface Ga/(Ga+In) ratio for the pre-rinsed CIGSe and CIGSe/SiO₂ absorbers samples are 0.30 and 0.33 (± 0.10), respectively, indicating a very small change in the surface ratio with the addition of the SiO₂ barrier. This is different than what the Ga 2p detailed region shows but is similar to what the Ga LMM presents. It is speculated that since the CIGSe/SiO₂ absorber has a larger O 1s and C 1s peak (as will be discussed in conjunction with Figures 5.13 and 5.15 later), the low KE (high BE) peaks would be more attenuated than the CIGSe absorber and higher KE peaks. After the NH₄OH treatment, the Ga/(Ga+In) ratio decreases: 0.25 ± 0.10 eV for the CIGSe absorber and 0.27 ± 0.10 eV for CIGSe/SiO₂ indicating a small Ga depletion at the surface after the rinse. For CKIGSe, the pre-rinse surface Ga/(Ga+In) ratio is similar to both CIGSe and CIGSe/SiO₂, 0.30 ± 0.10 eV, and exhibits a slightly larger Ga-depletion on the surface after the rinse, 0.23 ± 0.10 eV.

Figure 5.10 portrays the fits for the pre and post-rinse KF PDT and KF PDT/SiO₂ surfaces. Due to the broadness of the peaks, several species are expected to contribute to the overall spectra and are indicated with In-Se in black, In-O in pink, In-F in teal, Ga-

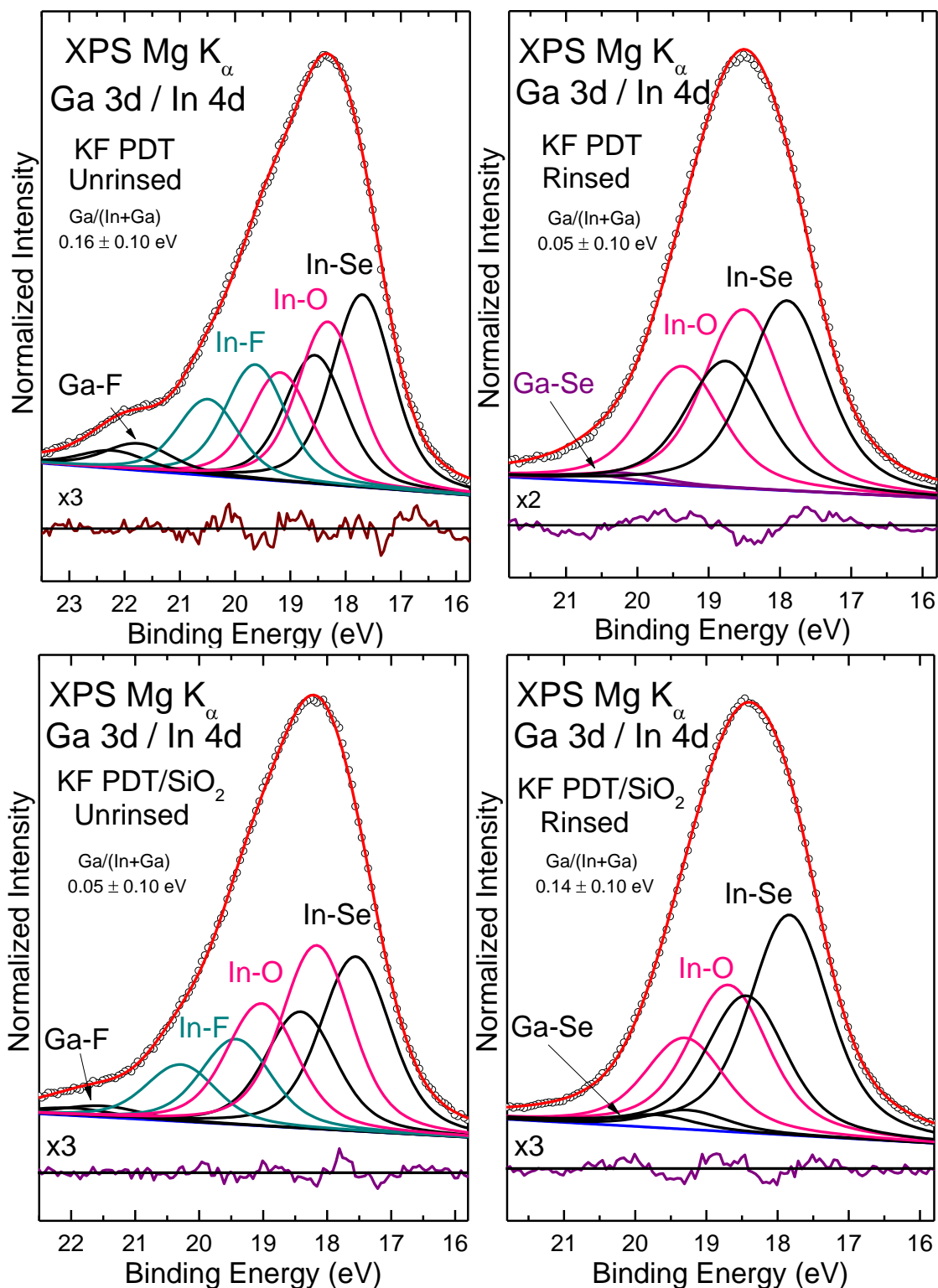


Figure 5.10: XPS detail spectra of the Ga 3d/In 4d region of the pre and post-rinse KF PDT absorber (top) and KF PDT/SiO₂ (bottom). Fit curves for In:Ga contributions to the peak are shown along with their respective residuals (purple).

F in black, and Ga-Se in purple. In contrast, the In 4d and Ga 3d peaks depicted in Figures 5.8 and 5.9 are indicative of In-Se and Ga-Se species. The presence of multiple species for the KF PDT absorbers is corroborated by the In 3d, In MNN, Ga 2p, and Ga LMM spectra seen previously. The peaks were identified according to references^{111,112} and their peak separations fixed amongst all the spectra. With a KF PDT on the absorber, Ga-depletion already occurs in comparison with the CIGSe and CIGSe/SiO₂ absorbers. The Ga/(Ga+In) ratio for the pre-rinse KF PDT absorber and KF PDT/SiO₂ absorber are 0.16 ± 0.10 eV and 0.05 ± 0.10 eV, respectively. The ratios suggest that with the addition of the SiO₂ barrier, the Ga-depletion on the surface is even more pronounced. After the NH₄OH treatment, the Ga components shift to lower binding energies (note the loss of the shoulder at 22 eV) indicative of Ga-Se^{111,112} (also seen with Ga LMM). The Ga 3d/In 4d region after the NH₄OH treatment is narrower for both samples. As a result, the peaks could be fit with only two In species instead of three but that is not to say the third species is gone. Adding a third species did not further enhance the residual, and in the case of the rinsed KF PDT fit, it was detrimental to the other fits. The peak s are labeled as In-O and In-Se due to their peak locations and evidence for a big reduction of In-F, but small reduction of In-Se and an increase in In-O as seen in the n MNN spectra. The resulting Ga/(Ga+In) ratio shows that the KF PDT surface exhibits an even more Ga-poor surface while the ratio for the KF PDT/SiO₂ absorber almost tripled (0.07 ± 0.10 eV and 0.14 ± 0.10 , respectively). Overall, the Ga/(Ga+In) ratio of the KF PDT absorbers shows that the treatment creates a more Ga-poor surface than the CIGSe and CKIGSe counterparts.

An inherent property of fitting peaks is that the more functions you add, the fit gets better. However, the functions need to be accounted for and they need to serve a purpose

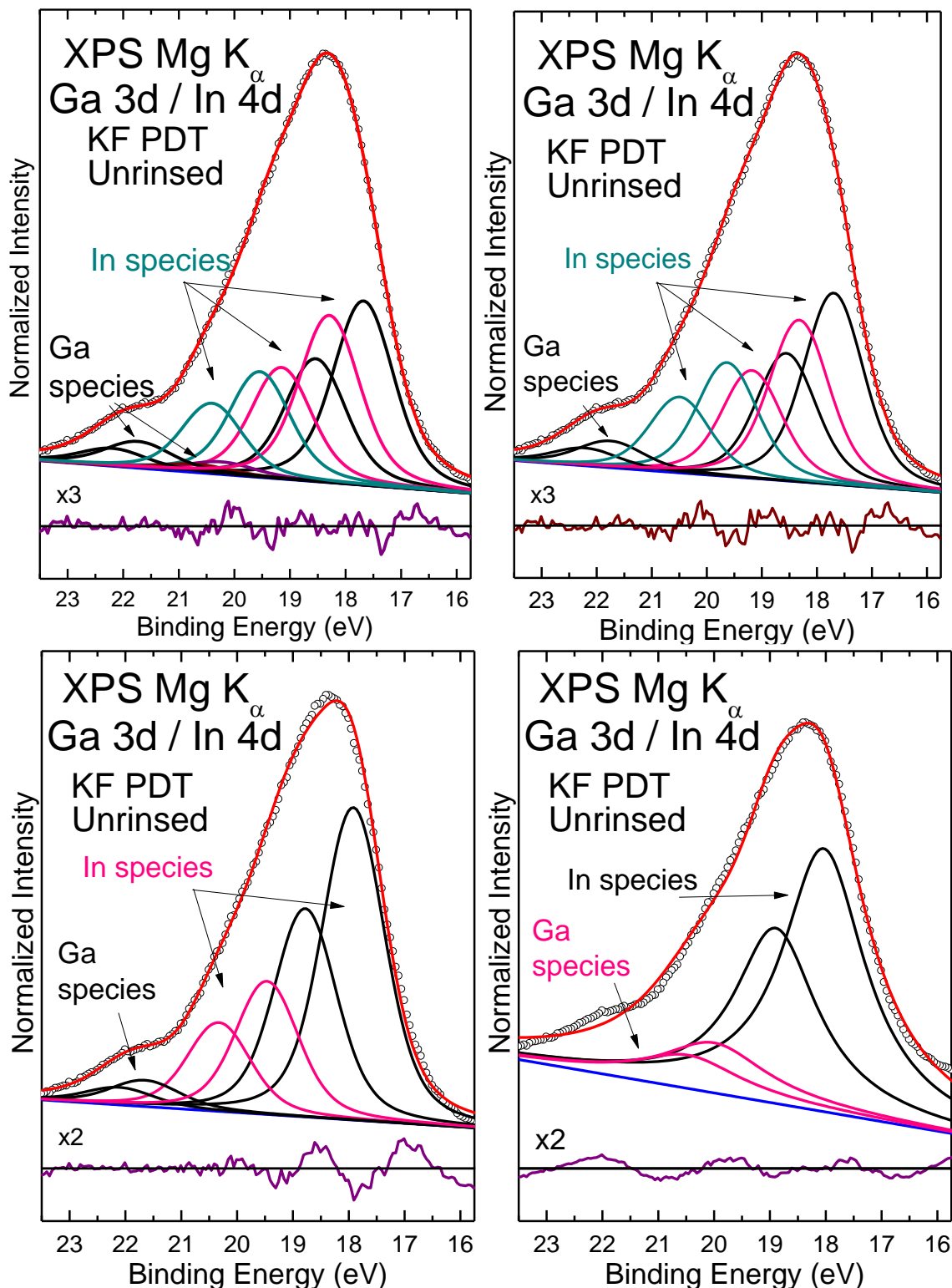


Figure 5.11: XPS detail spectra of the Ga 3d/In 4d region of the pre-rinse KF PDT absorber as a function of fit curves to show the process of determining a good fit. Fit curves for In:Ga (In 4d_{5/2}, In 4d_{3/2}, Ga 3d_{5/2}, Ga 3d_{3/2}) contributions to the peak are shown along with their respective residuals (purple).

in the fit. The KF PDT absorbers both required more components to fit the Ga 3d/In 4d region than the other samples and an example of the fitting process is presented in Figure 5.11. On the bottom right, the Ga 3d/In 4d region is only fit with 5 total components: a linear background, In 4d_{5/2}, In 4d_{3/2}, Ga 3d_{5/2}, and Ga 3d_{3/2}. The residual, shown below the fit, exhibits a sinusoidal shape indicative of a poor fit of the peak. With the addition of two more components (bottom left), representing the In 4d peaks, The resulting residual shows more statistical noise towards higher binding energies, but the fit towards lower binding energies is still poor. With the addition of another set of two components (top right), representing In 4d again, the fit of the peak is much better (note the magnification difference between the bottom two fits and the top two fits). Not only this, but the components can all be accounted for using evidence of other XPS detailed regions. The top left graph displays a fit with two more additional components, representing Ga 3d, however, there is not a significant improvement in the residual of the fit in comparison to the top right fit. Thus, the top right fit is used to describe the Ga 3d/In 4d region of the unrinsed KF PDT absorber.

To summarize our findings thus far, the analysis of the Cu, In, Ga, and Se photoemission and Auger peaks shows no evidence of Se and Cu oxides and fluorides, but evidence of Ga and In oxides and fluorides. We see a surface depletion of Cu and Se with the KF PDT that is even further reduced with the NH₄OH treatment. So far, we see that the KF PDT affects the surface of the CIGSe absorbers similarly for both the absorber with the SiO₂ barrier and the absorber without, while there are clear differences between the two untreated absorbers. The bare absorber without the SiO₂ barrier exhibits a larger Cu:In ratio (compared to its counterpart), but after the NH₄OH treatment, it is the

CIGSe/SiO₂ absorber that shows the larger Cu:In ratio. The CIGSe/SiO₂ absorber exhibits a slightly larger Ga/(Ga+In) ratio than the CIGSe absorber. The surface of the CKIGSe absorber is found to be more similar to the CIGSe (with and without SiO₂) absorbers, than the KF PDT absorbers, indicating that not only the addition of K but also the deposition method of KF plays an important role for the surface properties. The KF absorbers exhibit a strong Cu and Ga-depletion on the surface with the KF PDT absorber displaying the larger Cu:In and Ga/(Ga+In) ratios before the NH₄OH treatment. After the treatment, the KF PDT still has the larger Cu:In ratio, but the KF PDT/SiO₂ presents a larger Ga/(Ga+In) ratio. The ratio change for the KF PDT/SiO₂ suggests that either the deposition of Ga on

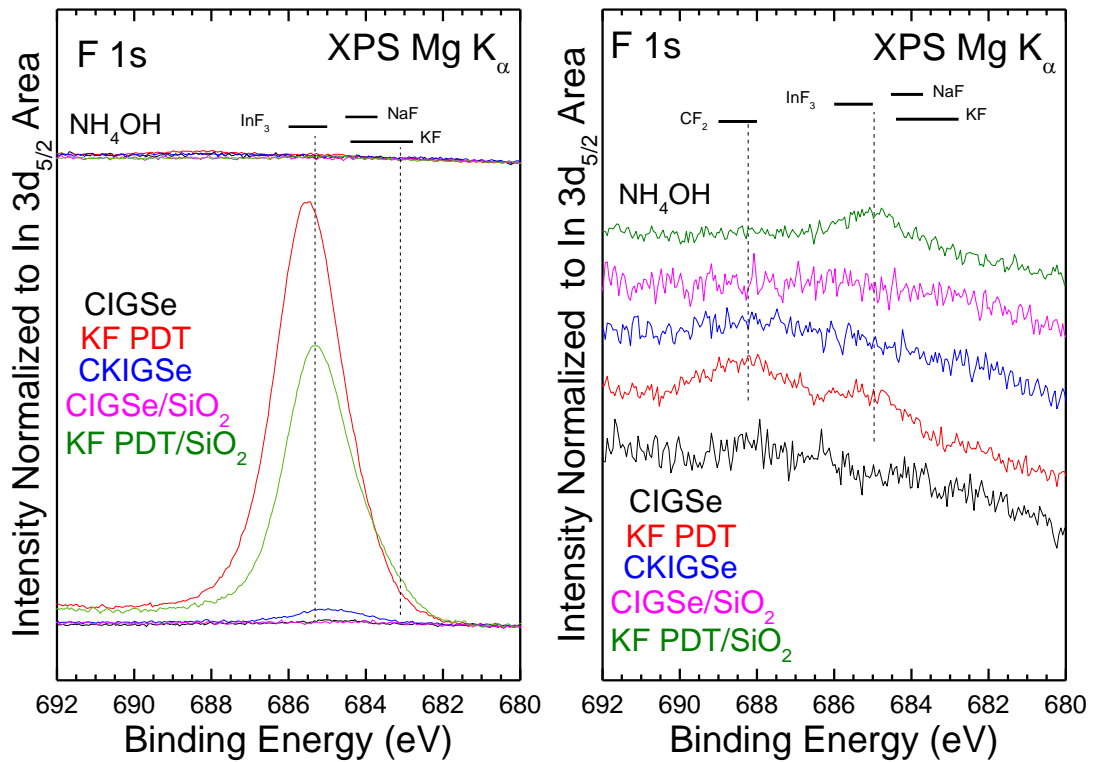


Figure 5.12: Detailed XPS Mg K_α spectra of the F 1s region, normalized by the In 3d_{5/2} area. The ion-treated spectra are shown at the bottom, while the NH₄OH-treated spectra are at the top (left). The right graph is scaled to see the F 1s peaks of the NH₄OH treated absorbers (only). The expected locations for InF₃, NaF, KF, and CF₃ contributions are indicated.

the surface occurred during the NH_4OH treatment, or Ga diffused to the surface from the bulk.

Analyzing the F peaks also offers direct insights into the local bonding environments on the surface. Figure 5.12 shows the presence of a F 1s signal for both the KF PDT absorbers and the CKIGSe absorber. The KF PDT peak is broader and larger than for KF PDT/ SiO_2 and CKIGSe, suggesting multiple species (corroborating the earlier evidence for the presence of Ga-F and In-F bonds). The KF PDT/ SiO_2 absorber is also broad and shows a larger tail towards ~ 682 eV, indicative of KF. This is supported by the KF peak intensities in Figure 5.6, where KF/ SiO_2 shows the largest peak. The

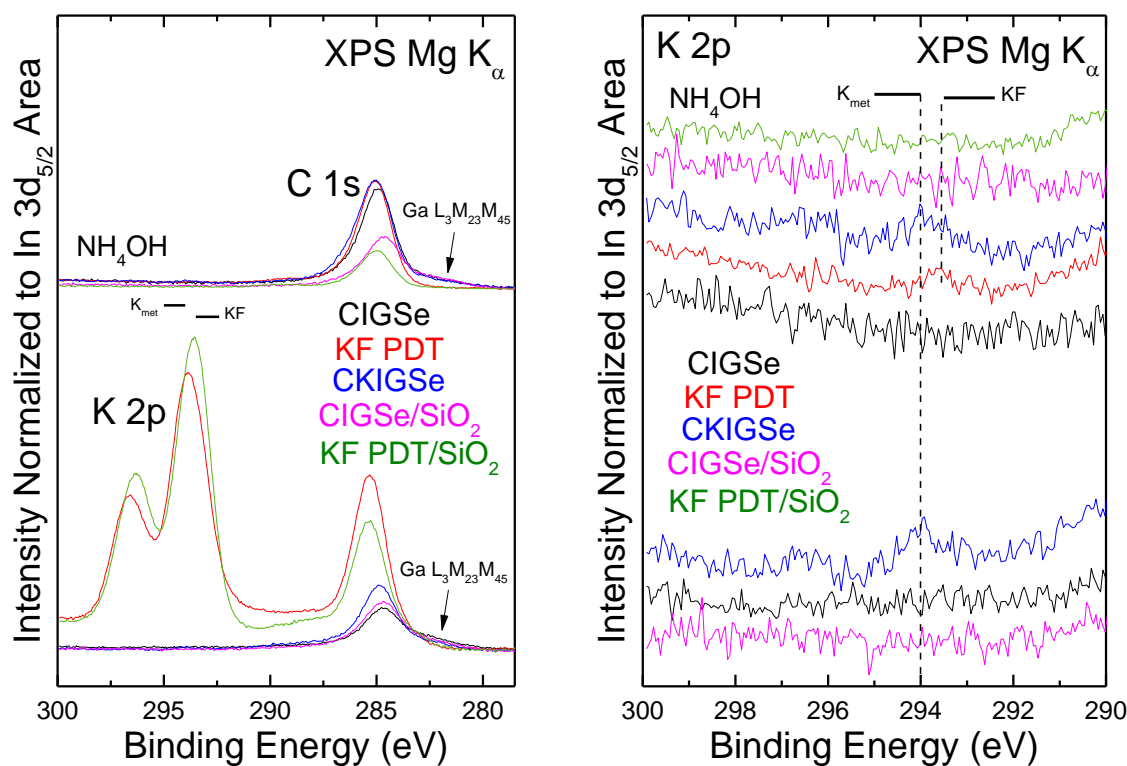


Figure 5.13: Detailed XPS Mg K $_{\alpha}$ spectra of the C 1s and K 2p region, normalized by the In 3d $_{5/2}$ area (left). The ion-treated spectra are shown at the bottom, while the NH_4OH -treated spectra are at the top (left). The right graph is magnified to show the K 2p peaks of the NH_4OH and ion-treated absorbers. The expected locations for Ga LMM, KF, and metallic K (K $_{\text{met}}$) are indicated.

CKIGSe F 1s peak is shifted towards lower BE, matching the BE range of NaF. On this scale, it appears that, after rinsing the absorbers, F is completely removed. However, closer inspection (Fig. 5.12 right) suggests otherwise. On this scale, it is clear that both KF PDT absorbers show F on the surface, with KF PDT/SiO₂ having one species that aligns well with In-F, and KF PDT having at least two species, most likely In-F and C-F. The NH₄OH treatment definitely reduces the F on the absorber surfaces, but it is not completely removed for the KF PDT absorbers.

Having established the presence of F on the various surfaces, we now turn to K. Detailed spectra of the C 1s and K 2p peaks are presented in Figure 5.13. In the C 1s plot on the left, all absorbers show C on the surface; however, both unrinsed KF PDT absorbers show the most. The spectral intensity between 287 and 291 eV is also quite large, possibly a combination of inelastically scattered electrons from the C 1s peak and the presence of multiple species, for example carbonates at 290 eV. This is further corroborated by the “dip” at ~291 eV seen for the KF PDT/SiO₂ absorber that is absent for the KF PDT absorber (even though this absorber shows more C and less K). Relative to the unrinsed KF-PDT absorbers, the C 1s peaks of the unrinsed CKIGSe and the two CIGSe absorbers are shifted towards lower BE. However, after the NH₄OH treatment, we find more C on the surface of CKIGSe and both CIGSe absorbers, while there is a significant decrease in C for both KF PDT absorbers (note that the shoulder at ~283 eV, which becomes more pronounced after the rinse, is a Ga LMM Auger line). K 2p peaks are visible for the unrinsed KF PDT absorbers, and very small peaks can also be seen for the unrinsed CKIGSe absorber (Figure 5.13, right), indicating that there is a lower concentration of K on the surface for the coevaporation process relative to PDT treatment.

The KF PDT/SiO₂ absorber shows the largest K 2p peaks before the rinse, and they shift towards lower BE relative to the KF PDT absorber. Magnifying the intensity scale (Figure 5.13, right), we also find a K 2p peak for the CKIGSe absorber, albeit very small. Like in the case of F, the KF coevaporation deposition does show traces of K on the surface. After the NH₄OH treatment, the K is removed from KF PDT/SiO₂ absorber, but it is still present for the CKIGSe (slightly reduced) and KF PDT (greatly reduced). The K peak position on both KF PDT absorbers before the rinse is indicative of a K-F bonding environment. For CKIGSe, the K 2p BE position is shifted towards higher BE.

The Na 1s region for the ion- and NH₄OH-treated absorbers are compared in

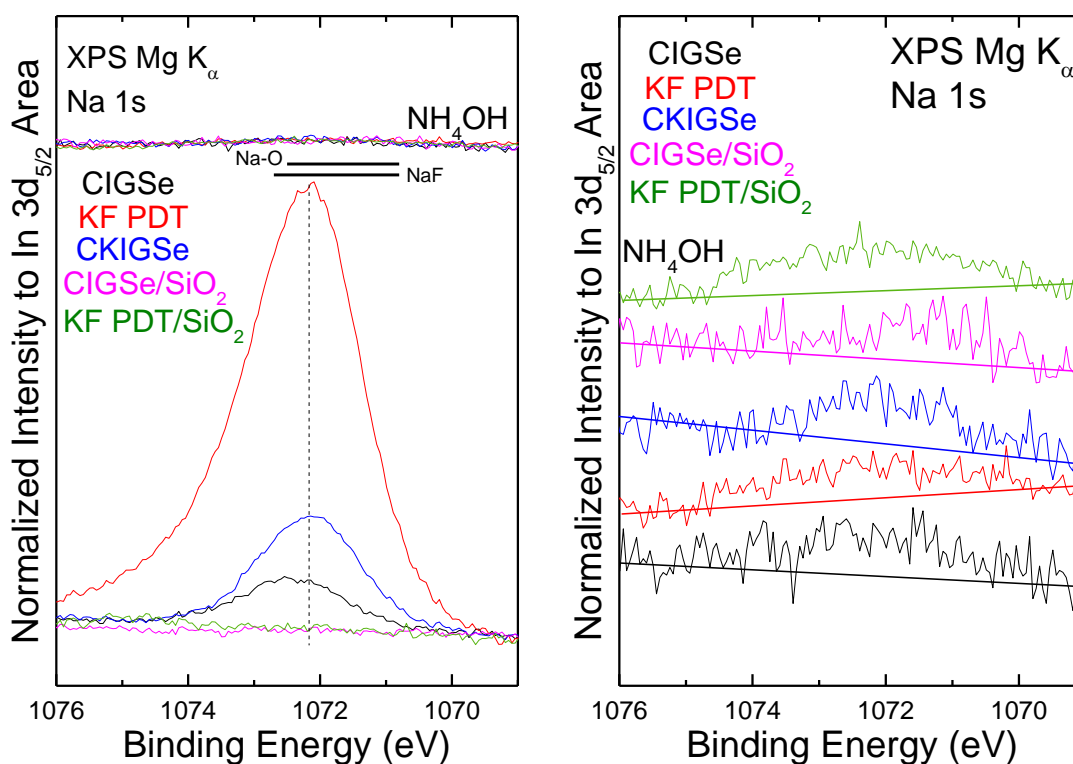


Figure 5.14: Detailed XPS Mg K_α spectra of the Na 1s region, normalized by the In 3d_{5/2} area. The ion-treated spectra are shown at the bottom, while the NH₄OH-treated spectra are at the top (left). The right graph is scaled to show the Na 1s peaks of the NH₄OH-treated absorbers (only). A line was drawn to help guide the eye. On the left, the expected locations for NaF and NaO contributions are indicated.

Figure 5.14. The effects of the SiO₂ barrier are clearly seen in the ion-treated spectra, in which there is no detectable Na peak on the surface of the samples with barrier. Among the barrier-free absorbers, the ion-treated KF PDT absorber shows the largest Na peak, almost triple the size of the CKIGSe Na peak. The Na peaks are broad and asymmetric, suggesting the presence of multiple species, including Na oxides and/or NaF. NaF species would make more sense on the CKIGSe and KF PDT absorbers since Figure 6 shows there is indeed F on the surface. Figure 5.14, right, presents magnified spectra of the NH₄OH-treated absorbers. We find trace amounts of Na on all five samples, including the absorbers with SiO₂ barrier, which might have been deposited during the NH₄OH treatment. A modified Auger parameter, α' , plot aids in identifying potential species using both the Na KLL and Na 1s peak separation. All of the absorbers range between the α' 2060 and 2063 eV along with all of the Na-oxide species. It is clear that the Na on the absorbers are not metallic. The rinsed CIGSe/SiO₂ has the same α' as NaHCO₂, NaOOCH, and Na₂SO₄ indicating that these are possible chemical environments for these two absorbers. Na₂SO₄ can be ruled out since there is no S on the samples. The pre-rinsed KF PDT absorber lies in between Na₂O and NaF and the α' could be a convolution of the two species. Figure 5.14 shows the Na 1s peak for this absorber and the broadness of the peak suggests multiple species. The α' plot shows that the Na on all of the absorber surfaces exhibits some Na-O bonding.

The variance in adsorbates on the absorber surfaces can clearly be seen in the O 1s spectra in Figure 5.16. Both, changes in the peak intensities (left) and peak position and shape (right) are evident. The KF PDT absorbers have the largest O 1s peaks, both before and after NH₄OH treatment. The peak shapes for all the absorbers, pre and post-

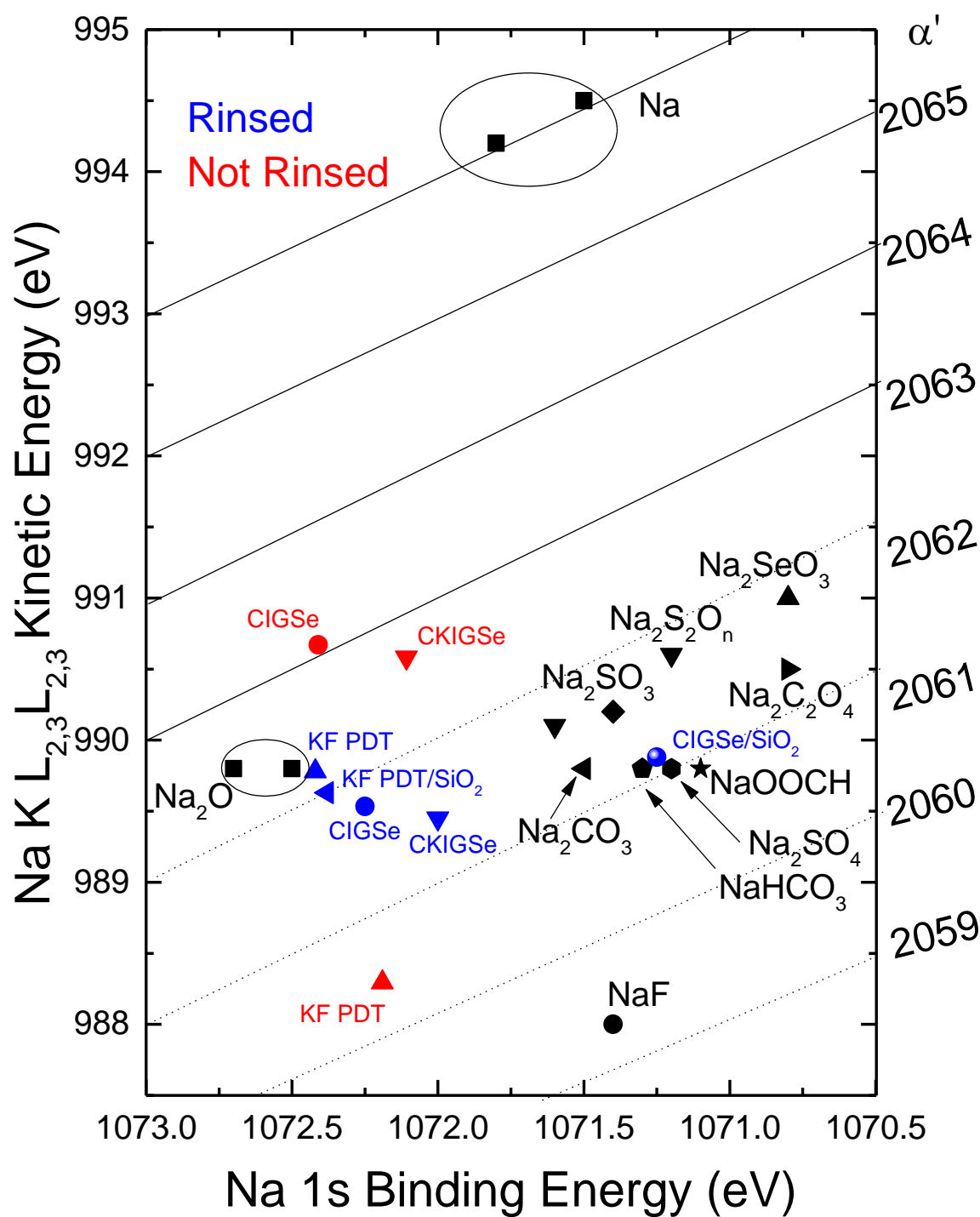


Figure 5.15: Modified Auger Parameter plot of Na 1s and Na KLL. The ion-treated data are shown in red, the NH₄OH treated data in blue, and references (111,112) in black.

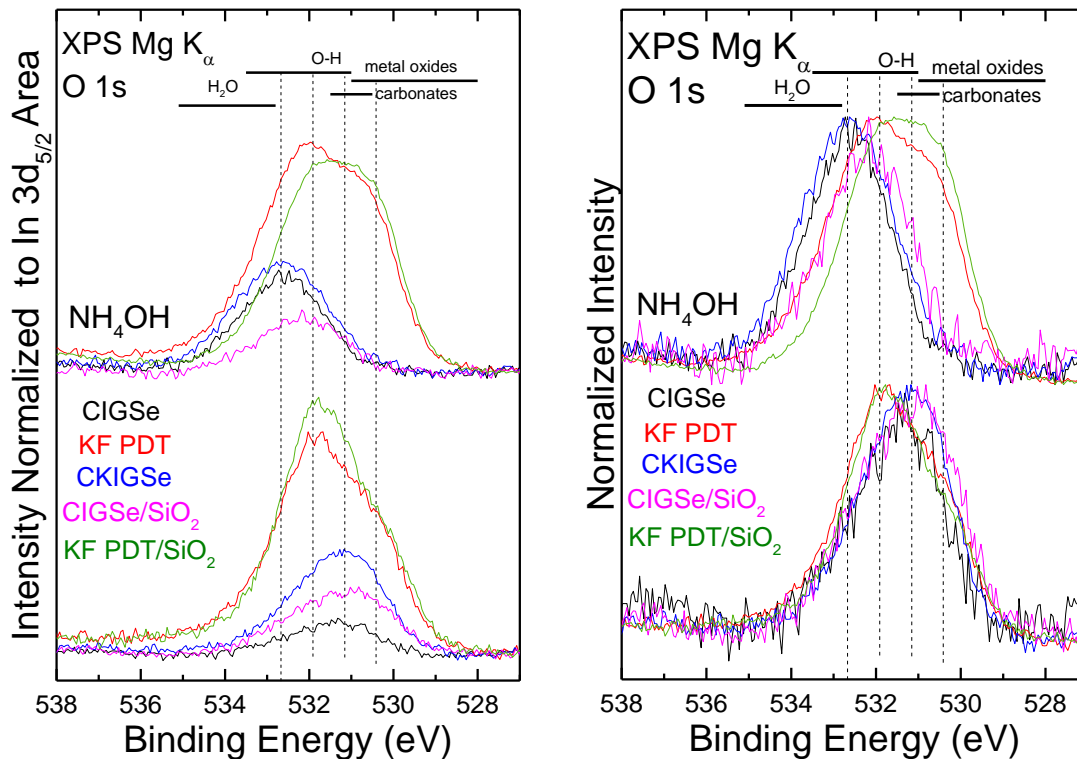


Figure 5.16: Detailed XPS Mg K_{α} spectra of the O 1s region, normalized by the In $3d_{5/2}$ area (left) and O 1s peak height (right). The ion-treated spectra are shown at the bottom, while the NH_4OH -treated spectra are at the top. The expected locations for water, hydroxide, metal oxides, and carbonates are indicated.

rinse, are asymmetrical and broad, suggesting multiple O species, mostly contributions from hydroxides and surface adsorbates. The changes in peak shapes and binding energies indicate a change in the relative amounts of hydroxide and oxide contributions. For example, the CKIGSe O 1s shifts almost 2 eV towards higher BE after the rinse, where the peaks of H_2O and OH are expected. Fits of these peaks are presented in Figures 5.17, 5.18, and 5.19. The peaks were fit with a linear background, identical Gaussian and Lorentzian widths, and fixed positions for all species. The residuals shown below the spectra indicate that the quality of the fit is quite high for all the surfaces. Peak assignments were determined utilizing references^{111,112,129}. The unrinsed CIGSe,

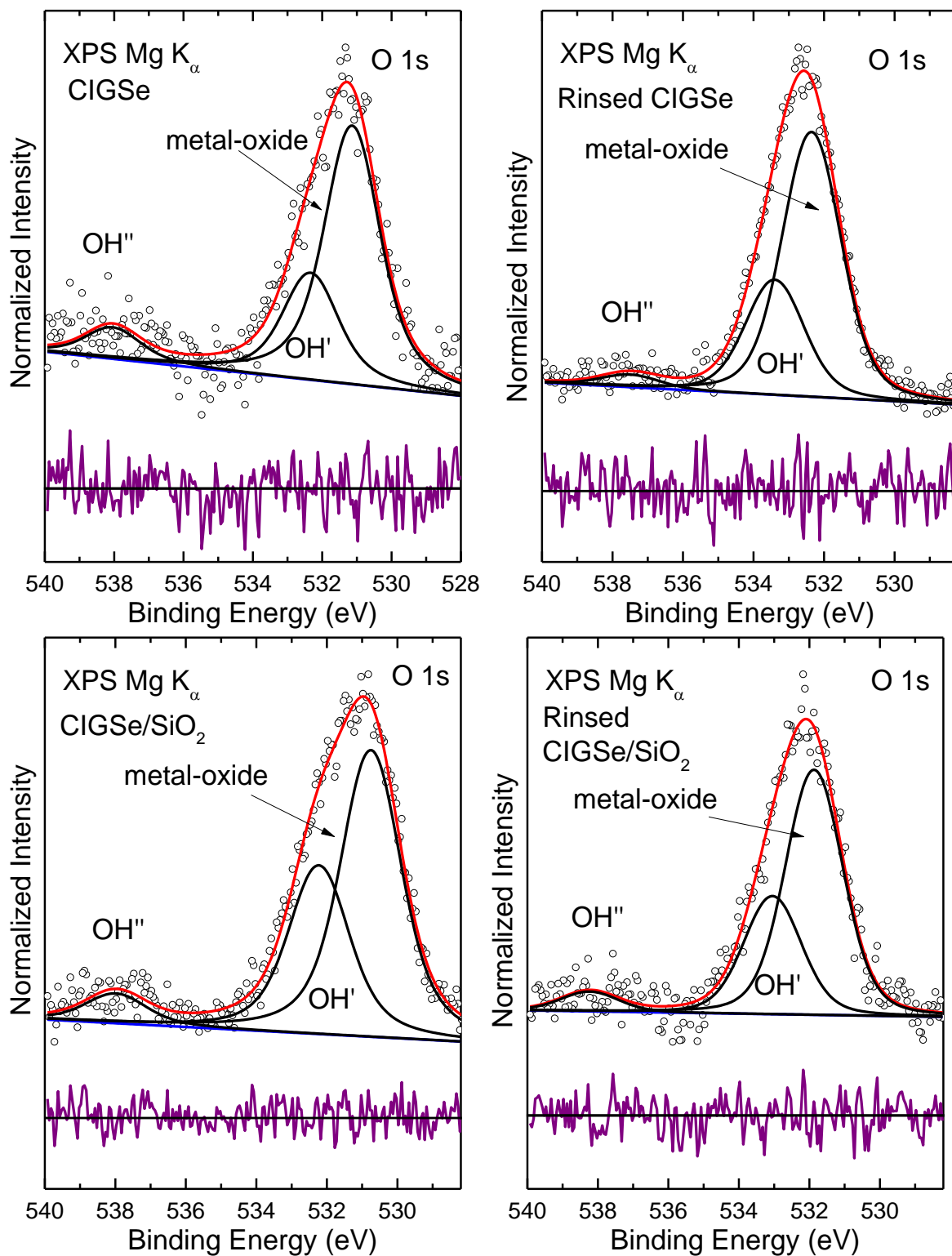


Figure 5.17: XPS detail spectra of the O 1s peak and fit (components in black, sum in red) of the pre and post-rinsed CIGSe (top) and CIGSe/SiO₂ samples (bottom).

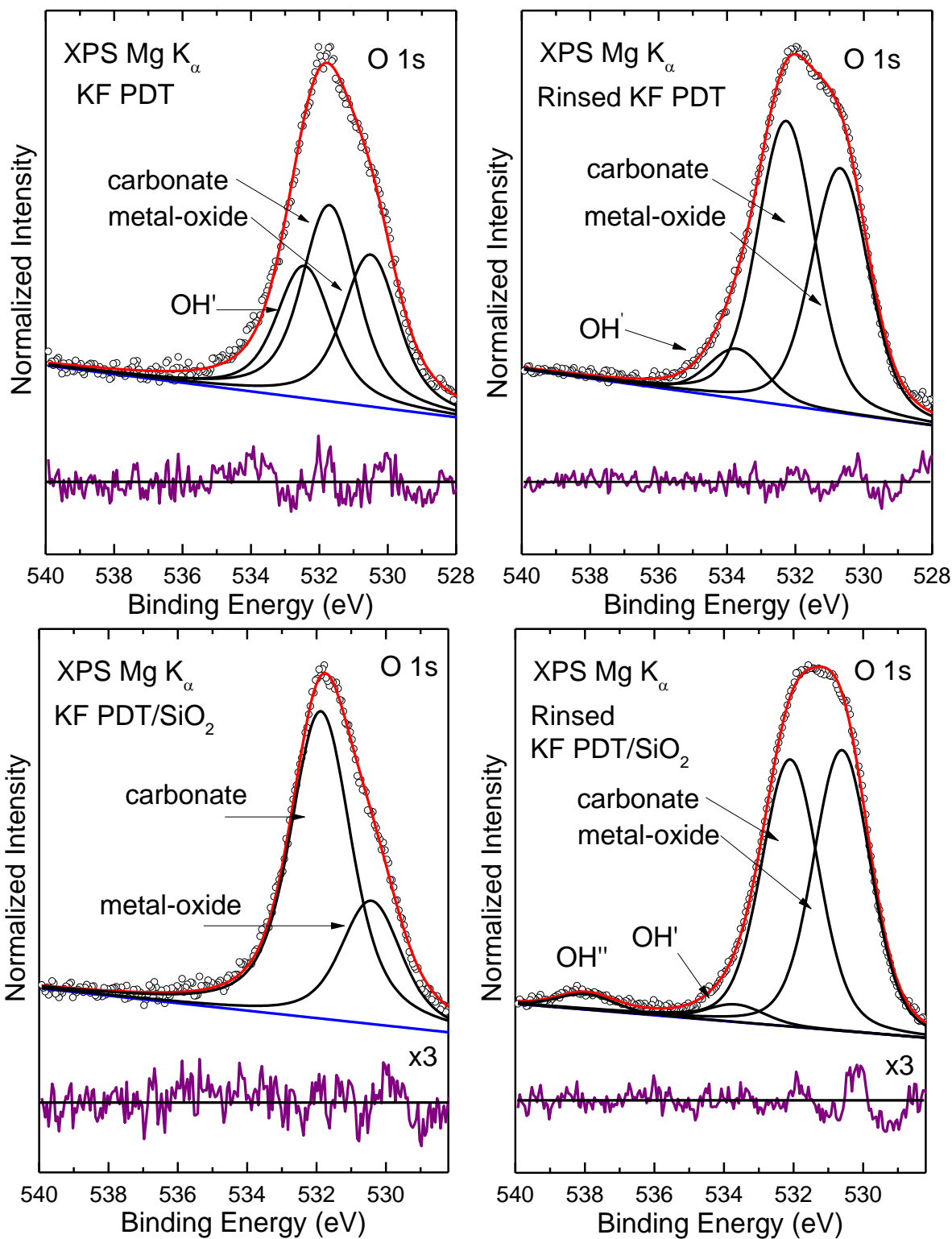


Figure 5.18: XPS detail spectra of the O 1s peak and fit (components in black, sum in red) of the pre and post-rinsed KF PDT (top) and KF PDT/SiO₂ samples (bottom).

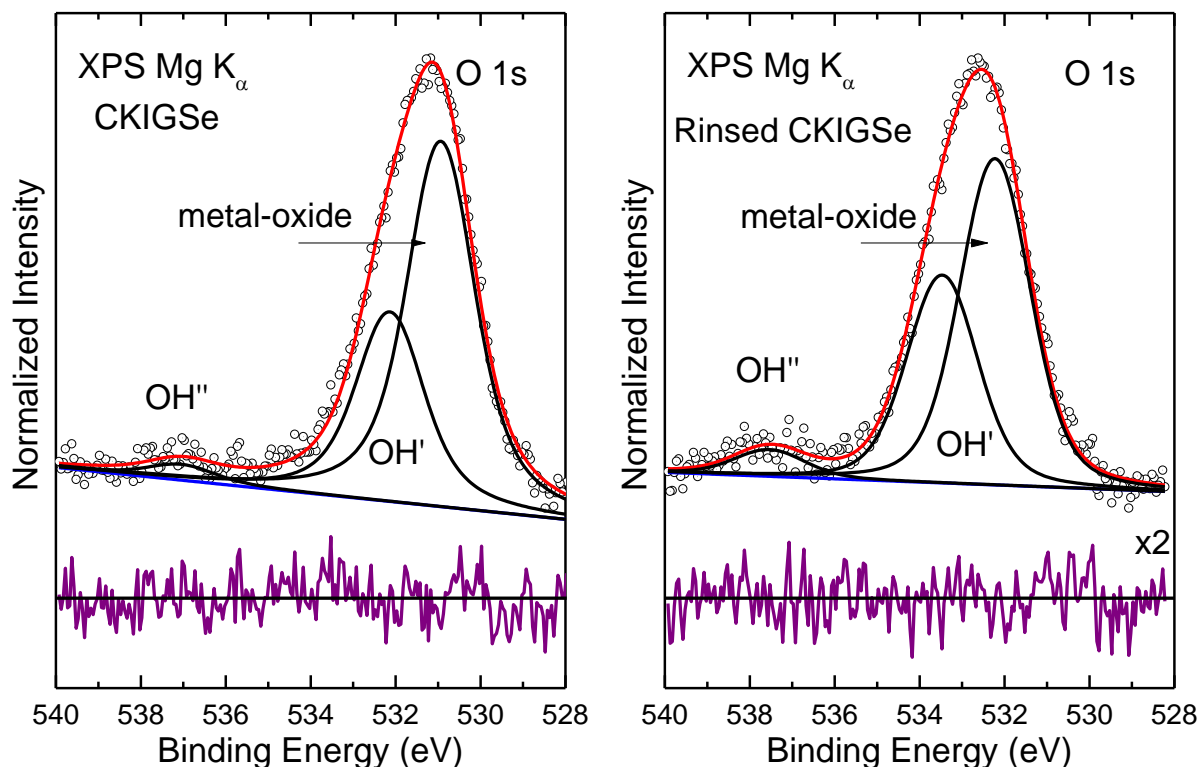


Figure 5.19: XPS detail spectra of the O 1s peak and fit (components in black, sum in red) of the pre and post-rinsed CKIGSe sample.

CIGSe/SiO₂, and CKIGSe all have O bonding to H on their surfaces in various bonding environments represented by the peaks located at ~533 eV (OH') and ~538 eV (OH''). The unrinsed KF PDT absorbers do not have OH'' on the surface, suggesting the OH'' was removed during the KF PDT. However, the KF PDT absorbers do have carbonate peaks that are not found for the CIGSe and CKIGSe absorbers. Recall that both unrinsed KF PDT absorbers had the largest C 1s peaks and evidence of carbonates at ~290 eV (Figure 5.13). Rinsing the CIGSe and CKIGSe absorbers cause the O 1s peak to shift towards lower BE and changes the OH:O ratio. For the CIGSe and CIGSe/SiO₂ absorbers, the OH:O ratio decreases while for CKIGSe it increases. The OH'' peak also decreases for both CIGSe absorbers but increases for the CKIGSe absorber. Rinsing the

KF PDT absorbers increases the metal-oxide peak (recall the increase in In-oxide species after rinsing both KF PDT absorbers). However, the other species behave differently between the samples. For the KF PDT absorber, the carbonate peak increases by about a third, the OH' peak decreases, and there is no indication of OH'' on the surface. For the

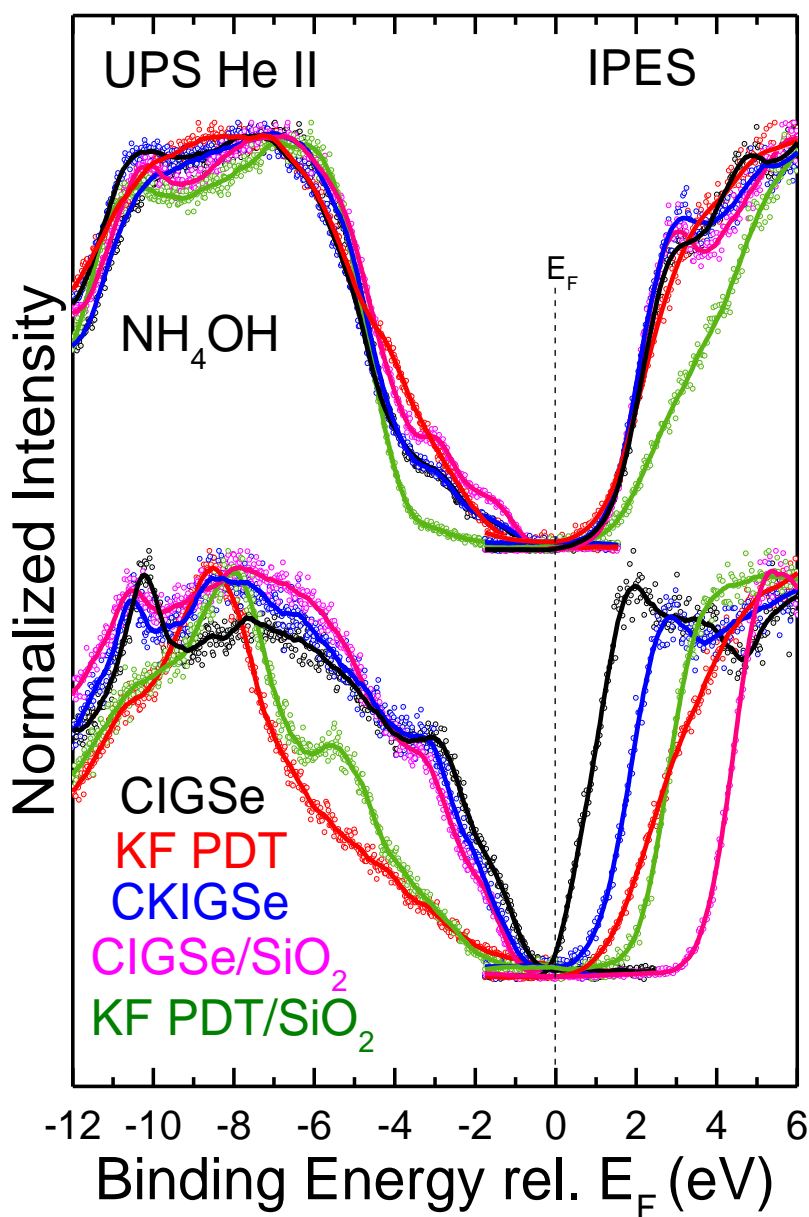


Figure 5.20: UPS (He II) and IPES spectra of all absorbers. A Savitsky-Golay smooth line is used as a guide to the eye.

KF PDT/SiO₂ absorber, there is an addition of OH^{''} and OH['] species and a reduction in the carbonate peak. Rinsing all the absorbers does not produce the same result amongst the samples.

Figure 5.20 shows UPS (He II) and IPES data of the valence (VB) and conduction band (CB) and their edge positions with respect to the Fermi energy. The NH₄OH treated absorbers are shown on top, while the ion-treated are on the bottom. The spectra are stacked to show changes in spectral intensity and shifts of the leading edge. For the ion-treated surfaces, the KF PDT/SiO₂ and CIGSe/SiO₂ absorbers exhibit CBM's furthest from E_F, while both KF PDT absorbers show VBM's furthest from the E_F. The Cu 3d band (at approx. -3 eV) is most pronounced for the CIGSe and CKIGSe absorbers (pre-rinse). Post-rinse, the spectral weights of most of the absorbers are very similar with more changes seen in the VBM. The KF PDT/SiO₂ is the outlier with the valence band and conduction band spectra shifted farther from the E_F and the spectral weight being different.

Figure 5.21 separated the UPS/IPES spectra to present changes in the bandgap among the different samples and as a function of NH₄OH treatment. The ion-treated surfaces are shown in black, while the rinsed surfaces are shown in red. In comparison to both CIGSe absorbers all KF incorporated samples exhibit a widening of the bandgap, with the largest post-rinse bandgap being 2.93 ± 0.15 eV, and the smallest 2.02 ± 0.15 eV. The electronic surface bandgaps of the two CIGSe absorbers are 1.60 and 1.66 ± 0.15 eV. The majority of the change between KF-treated and untreated CIGSe absorbers comes from changes in the conduction band maximum. Although the spectral weight distributions of the valence band change after rinsing, the derived valence band maxima

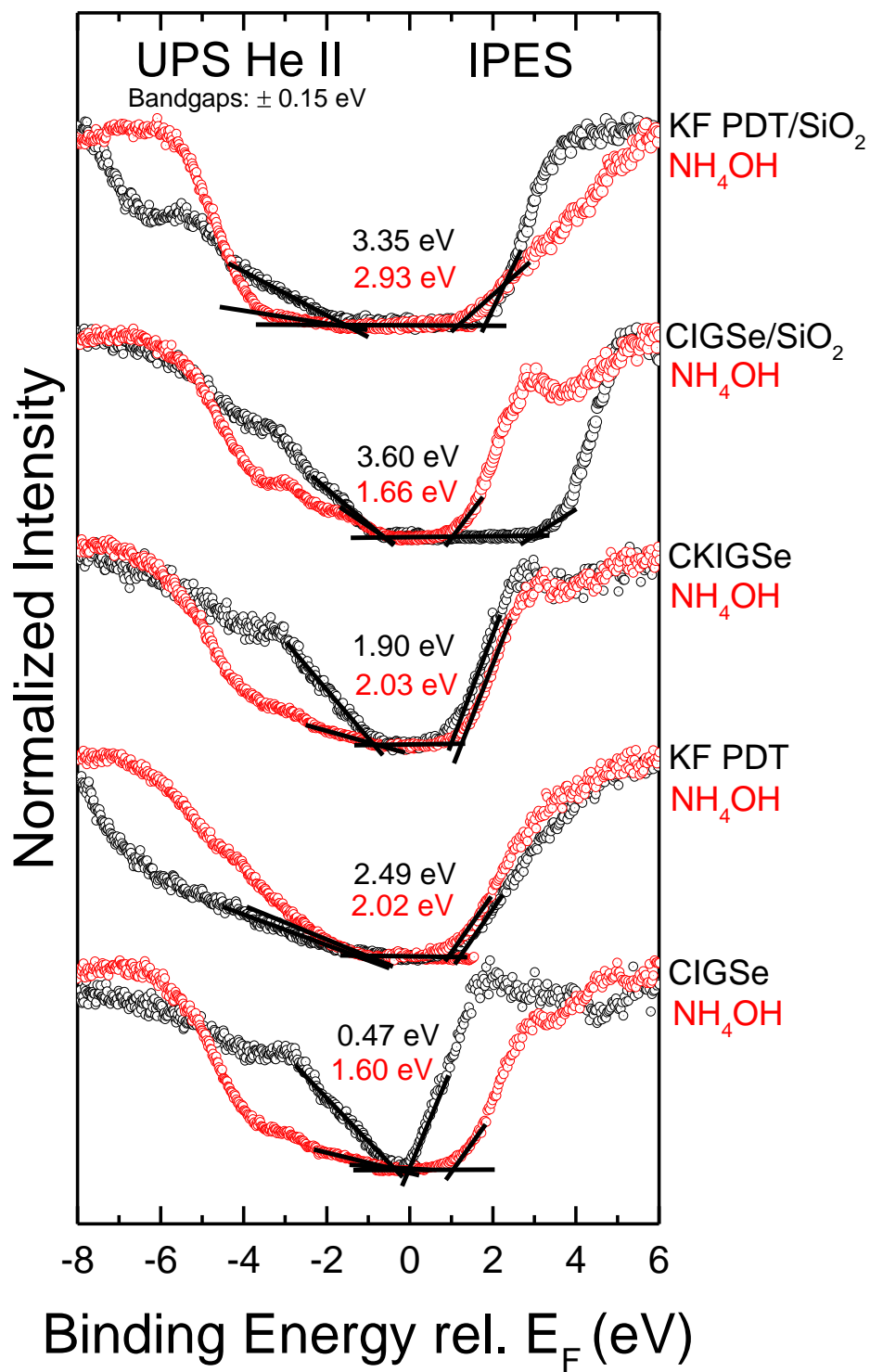


Figure 5.21: UPS (He II) and IPES spectra of all absorbers. The ion-treated surfaces are shown in black, while the rinsed surfaces are shown in red.

(VBM) do not deviate much from the “pre-rinse” VBMs. The largest change is seen for the CIGSe/SiO₂ absorber, where the pre-rinse bandgap was 3.60 ± 0.15 eV and the post-rinse 1.66 ± 0.15 eV.

5.4 – CONCLUSION

In summary, XPS, UPS, and IPES were used to investigate the chemical and electronic properties of this alkali study. We find that the Cu:In ratio is smallest for both KF PDT absorbers (in comparison to the large Cu peak seen for the bare CIGSe absorbers), suggesting that the KF PDT leads to a depletion of Cu from the surface of nominally stoichiometric films. We note that the Cu:In ratio of the bare CIGSe absorbers deposited with constant elemental flux is much larger than the three-stage coevaporated PDIL CIGSe absorbers, and thus a reduction of the Cu surface content can be more easily achieved.

In-F and Ga-F species are found on the ion-treated surfaces of both KF PDT absorbers. After the NH₄OH treatment, the Ga-F and Ga-O bonds are removed, and a Ga depletion of the surfaces is observed. In-F bonds are greatly reduced, but still present, and the contribution of In-O species is enhanced. The Ga/(In+Ga) ratio of the CIGSe, CKIGSe, and CIGSe/SiO₂ absorbers are larger than the KF PDT absorbers. The ratio decreases after the NH₄OH treatment except for the KF PDT/SiO₂ absorber where there is an increase.

Both K and F are deposited on the surfaces of the KF PDT absorbers, and K and F are also observed the surface of the CKIGSe film, but to a smaller degree. The NH₄OH treatment removes the K completely from the surface of KF PDT/SiO₂, significantly

reduces K and F on KF PDT, and slightly reduces K and F for CKIGSe. Na is present on CIGSe, KF PDT, and CKIGSe pre and post-rinse but Na is only observed for the SiO₂ absorbers after the NH₄OH rinse, suggesting that Na is deposited during the NH₄OH treatment. The Na on all the absorbers are found in an Na-O bonding environment.

UPS and IPES show that incorporation of K widens the bandgap of the CIGSe absorber, with the largest surface bandgap (among the rinsed samples) of 2.93 ± 0.15 eV found for the KF PDT/SiO₂ absorbers. In future experiments (projects), it would thus be of great interest to also determine the band alignment between such modified absorber surfaces (with K-induced bandgap widening) and both standard (CdS) and alternative [(Zn(O,S))] buffer materials to study the impact on the interfacial electronic structure.

CHAPTER SIX

ELECTRONIC STRUCTURE OF THE Zn(O,S)/CIGSe THIN-FILM SOLAR CELL INTERFACE

The majority of the following chapter has been previously published in Progress in Photovoltaics: Research and Applications and reports work performed to study the electronic properties of alternative buffer materials. Reprinted with permission from Michelle Mezher, Rebekah Garriss, Lorelle M. Mansfield, Kimberly Horsley, Lothar Weinhardt, Douglas Duncan, Monika Blum, Samantha G. Rosenberg, Marcus Bär, Kannan Ramanathan, and Clemens Heske, Electronic structure of the Zn(O,S)/CIGSe thin-film solar cell interface, Progress in Photovoltaics: Research and Applications 2016, In Print. Copyright 2016 John Wiley and Sons.

6.1 – INTRODUCTION

Cu(In,Ga)Se₂ (CIGSe) thin-film photovoltaic devices have achieved a record efficiency of 22.3% on a laboratory scale⁴. Traditionally, high-efficiency devices contain a CdS buffer layer between CIGSe absorber and transparent front electrode⁴². In contrast, the recent breakthrough was achieved with an alternative Cd-free buffer layer [Zn(O,S)], and other groups have also reported high conversion efficiencies for the Zn(O,S)/CIGSe system^{58,130–132}. Such buffers are desirable as they offer higher transparency and thus the possibility of increasing the current collection in the shorter wavelength region. For further optimizing such alternative buffer layers, understanding the interactions between the chalcopyrite absorber and the buffer layer is crucial, and several studies with this focus have already been published^{84,133–136}.

A characteristic of record CdS/CIGSe devices is the presence of a flat conduction band alignment at the buffer/absorber interface, both for CdS/CuInSe₂ and CdS/Cu(In,Ga)(S,Se)₂^{25,52,59}. In contrast, the less efficient CdS/Cu(In,Ga)S₂ system has been shown to exhibit a cliff-like conduction band offset (CBO)⁵¹. It is thus important to

understand the band alignment at the Zn(O,S)/CIGSe interface by direct and independent analysis of the valence and conduction band energies without the detrimental effects of sputter depth-profiling, and to compare its commonalities and differences with respect to the CdS-containing CIG(S)Se thin-film photovoltaic systems.

When using Zn(O,S) as a buffer material, it should be noted that ZnS and ZnO have large optical band gaps, 3.54 eV¹³⁷ and 3.3 eV¹³⁸, respectively, whereas the band gap of the Zn(O,S) alloy can show a strong bowing effect as the O:S ratio varies^{139,140}, with a minimum at 2.6 eV for a S/(S +O) ratio of 45%⁵⁷. Nevertheless, even at this minimum, Zn(O,S) still exhibits an optical band gap that is approximately 0.2 eV larger than that of CdS (2.4 eV⁴⁷), promising a higher transparency. To thus gain insights into the electronic level alignment when utilizing Zn(O,S) buffers, it is pertinent to perform a detailed experimental study; here, we present the first non-destructive analysis of the interface using XPS, UPS, and IPES, investigating samples with varying buffer layer thickness.

6.2– EXPERIMENTAL

A Zn(O,S)/CIGSe sample series was deposited at NREL, consisting of a CIGSe “bare” absorber and two Zn(O,S)/CIGSe interface samples of varying Zn(O,S) thickness. The absorbers were deposited onto a Mo-coated soda lime glass substrate using the standard three-stage process and a bulk Ga/(Ga+In) ratio of 0.3¹⁸. Our surface-sensitive XPS studies find a Ga/(Ga+In) ratio of 0.33 and 0.32 (± 0.10) for the CIGSe and thinnest buffer layer sample, respectively. The Zn(O,S) films were grown by chemical bath deposition (CBD) utilizing zinc sulfate, thiourea, ammonium hydroxide, and dimethyl sulfoxide¹⁴¹.

Auger depth profiling studies at NREL showed that the CBD process yielded Zn(O,S) films with a composition of ~25 at% S and ~20 at% O ($S/(S+O) \sim 0.56$). The CBD time was varied to control the thickness of the Zn(O,S) layer on the absorber – the “thick” Zn(O,S)/CIGSe sample was deposited by the standard 22.5 minute CBD process, whereas the “thin” Zn(O,S)/CIGSe sample was deposited by an abbreviated 5 minute CBD. Completed twin devices demonstrated an average efficiency of 17.7% (with a maximum of 17.8%). According to our XPS analysis, the thick layer is clearly a “closed” layer [Chapter 7].

XPS, UPS, and IPES were performed at UNLV to investigate all three samples. XPS measurements were taken using Mg K_{α} and Al K_{α} radiation, and He I and II irradiation were used for the UPS measurements. In this paper, only the results obtained with Mg K_{α} and He I radiation are shown (while the other results nevertheless contributed to the overall interpretation). XPS and UPS measurements were taken with a SPECS PHOIBOS 150 MCD electron analyzer, calibrated using core-level and Auger peaks of clean Ag, Cu, and Au foils (for XPS)⁷⁸, and the Fermi energy of the Au foil (for UPS and IPES). All samples were treated with a low-energy (50 eV) Ar⁺ ion treatment at a low incidence angle. This has been shown^{25,83} to be very effective in removing C and O contaminants from chalcopyrite, CdS, and ZnO surfaces without creating metallic phases commonly found when sputter-cleaning or depth-profiling such surfaces with higher ion energies. The CIGSe absorber was treated for a total of 120 min, and both Zn(O,S)/CIGSe samples were treated for 20 min each to remove (a portion of) the surface adsorbates while minimizing any potential beam damage (note that intense x-ray and electron flood gun irradiation has been shown to induce changes in the zinc hydroxide / zinc oxide ratio of

hydroxide-rich films^{142,143}). All peaks were analyzed by fitting the different spectral intensities with Voigt functions (with coupled Lorentzian and Gaussian widths) and a linear background using the Fityk peak-fitting program⁹⁰. A commercial low-energy electron gun (Staib) and a home-built Dose-type detector with a SrF₂ window and Ar:I₂ filling⁸¹ were used for IPES experiments. The valence band maximum (VBM) and conduction band minimum (CBM) were determined by linear extrapolation of the leading edge in the valence band (UPS) and conduction band (IPES) spectra⁸². The base pressure in the chamber was $<5 \times 10^{-10}$ mbar.

6.3 – RESULTS AND DISCUSSION

Figure 6.1 presents Mg K_α XPS spectra of the O 1s region of the thick and thin Zn(O,S)/CIGSe samples. The shape and broadness of the O 1s peak in both samples indicates the presence of multiple chemical species. Indeed, a fit analysis shows that a single Voigt peak does not give a satisfactory description, indicating that at least two species are present. Conversely, we find that the quality of the fit achieved with two Voigt functions for each O 1s region (with a linear background and identical Gaussian and Lorentzian widths for all the species) is already very high, and that a third component does not lead to a significant further improvement. Consequently, the residuals shown below each spectrum show a statistical distribution without any evidence for additional peaks.

Comparing the binding energies with values from literature, the two components for both samples can be assigned to ZnO and Zn(OH)₂^{111,144}. Since the Zn(O,S) is deposited onto the CIGSe via a wet-chemical deposition route, Zn-OH bonds are not

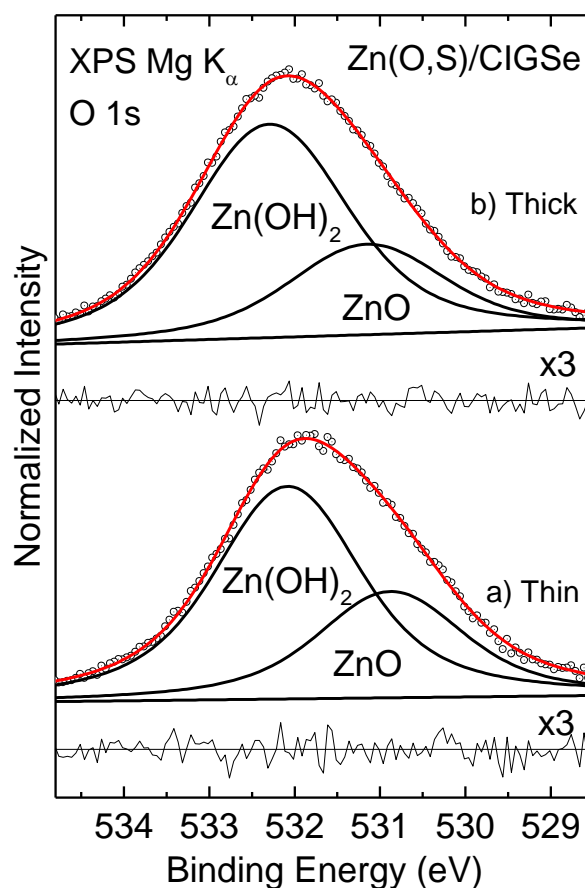


Figure 6.1: XPS detail spectra of the O 1s peak and fit (components in black, sum in red) of a) the thin (5 min) and b) the thick (22.5 min) Zn(O,S)/CIGSe samples. The magnified residual of each fit is also shown.

unexpected⁵⁸, suggesting that the dehydrogenation of the Zn(O,S) layer is incomplete for both the thin and thick Zn(O,S)/CIGSe samples^{53,139}. The possibility of a sulfate species was also taken into account since the O 1s peak location of a sulfate species and a hydroxide species are similar. However, none of our sulfur XPS spectra show any evidence for sulfates. Overall, our XPS, x-ray excited Auger electron spectroscopy and x-ray emission spectroscopy results suggest the presence of up to 4 different Zn species (associated with Zn-containing bonds similar to those in ZnO, ZnS, Zn(OH)₂, and ZnSe) [Chapter 7].

UPS and IPES spectra to analyze the valence (VB) and conduction band (CB), respectively, of the bare CIGSe absorber and the thick (22.5 min) Zn(O,S) CBD buffer layer are shown in Figure 6.2. The VBM and CBM for the bare CIGSe absorber are found at $-1.05 (\pm 0.10)$ below and $0.50 (\pm 0.15)$ eV above the Fermi energy, respectively. The thus derived electronic surface band gap of $1.55 (\pm 0.18)$ eV agrees well with previously

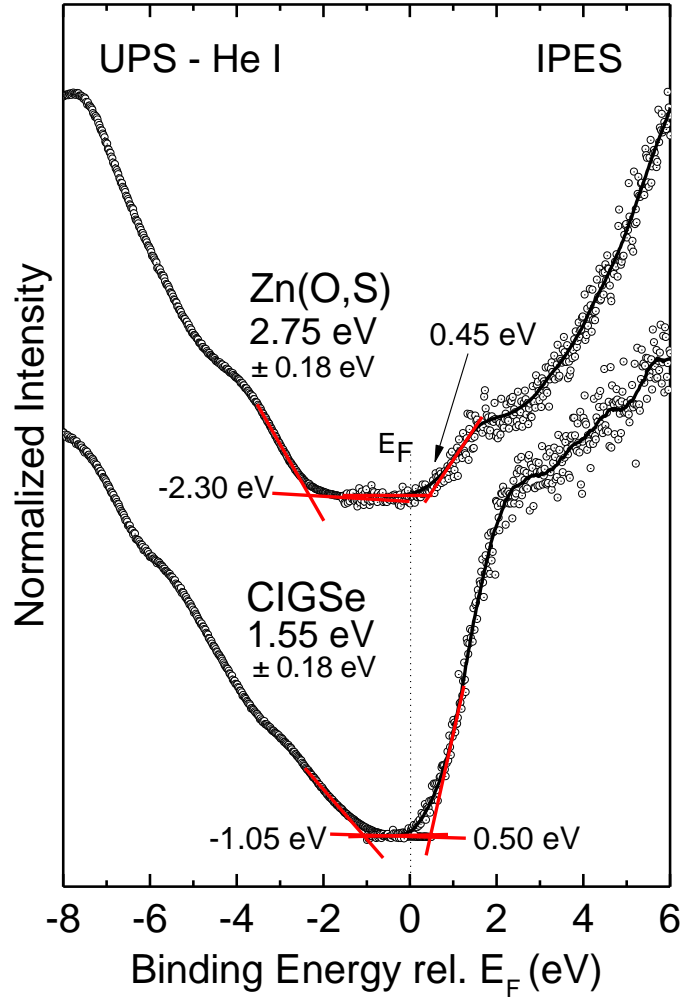


Figure 6.2: He I UPS (left) and IPES (right) spectra of the bare CIGSe absorber (bottom) and the thick Zn(O,S)/CIGSe sample (top). VBM and CBM values determined by linear extrapolations of the leading edges (red lines) are shown, together with the resulting electronic surface band gaps. Error bars are ± 0.10 and ± 0.15 eV for the VBM and CBM determination, respectively. A Savitzky-Golay-smoothed line is shown for the IPES spectra as a guide to the eye.

measured CIGSe surface band gaps of high efficiency absorbers with Cu-poor surfaces^{23,25,52,59,85,86}. The VBM and CBM of the Zn(O,S) layer are found at -2.30 (± 0.10) eV and 0.45 (± 0.15) eV, respectively, deriving an electronic surface band gap of 2.75 (± 0.18) eV. Note that the optical (bulk) band gap of a pure Zn(O,S) alloy with a S/(S+O) ratio of ~56% is expected to be ~2.6 (± 0.10) eV⁵⁷. A larger Zn(O,S) surface band gap in our case might be due to various reasons, including the presence of Zn-OH bonds (as shown by the O 1s spectra) and the above-mentioned presence of multiple Zn-containing species⁵³.

To derive a complete description of the band alignment at the interface, additional information is needed to take into account how the band bending at the absorber surface changes during the formation of the interface, as well as whether/how a band bending evolves in the buffer layer (as a function of thickness). For this purpose, the thin Zn(O,S)/CIGSe sample serves as an intermediate step in the interface formation (note that it is not possible to derive electronic structure information from an interface by sputter depth-profiling through the top layer due to the induced structural and chemical defects and compositional changes associated with preferential sputtering). Deriving the band bending changes is done by comparing the core-level peak positions of the CIGSe absorber (Se, In, Cu) to those of the thin Zn(O,S)/CIGSe sample, as listed in Table 1 (top). The observed shifts lie between 0.03 eV and 0.10 eV and indicate a very small upward shift [0.06 eV] of the absorber surface band edges as the interface starts to form. In other words: the (expected) downward band bending at the absorber surface is slightly reduced by the interface formation. This needs to be compared with the CdS/CIG(S)Se system, where we either find a negligible impact on the band edge positions^{25,52,59} or a

small additional downward shift [unpublished]. The here-observed (small) upward shift could have several origins, including a small change in the CIGSe surface dipole upon becoming an interface dipole to the Zn(O,S) layer, and a possible charge transfer across the interface to influence the space-charge region. The latter interpretation would require that the Fermi level at the interface is not pinned.

To investigate whether/how band bending evolves in the buffer layer as a function of thickness, the core-level binding energy differences between the thin and thick Zn(O,S) samples (Zn, O, and S core levels) are compared, as listed in Table 1 (bottom). As the buffer layer thickness increases, the Zn, O, and S core-level peaks from the thin Zn(O,S)/CIGSe sample also shift toward lower BE. For a quantitative analysis, we need to take into account that the buffer layer consists of multiple chemical species, as discussed above. For oxygen, we thus analyze both components (i.e., the ZnO and Zn(OH)₂ species) separately in order to avoid spurious peak shifts due to a variation in

Table 6.1: Core level peak positions of the bare absorber, the thin (5 min) Zn(O,S)/CIGSe sample, and the thick (22.5 min) Zn(O,S)/CIGSe sample, as well as their relative shifts.

Core Level	CIGSe BE (eV)	Thin 5 min Zn(O,S) BE (eV)	Shift
Se 3d	54.33	54.30	0.03
In 3d _{5/2}	444.78	444.68	0.10
Cu 2p _{3/2}	932.56	932.52	0.04
Core Level	Thin 5 min Zn(O,S) BE (eV)	Thick 22.5 min Zn(O,S) BE (eV)	Shift
S 2p _{3/2}	161.91	162.12	0.21
O 1s (Zn(OH) ₂)	532.06	532.25	0.19
O 1s (ZnO)	530.89	531.08	0.19
Zn 2p _{3/2}	1022.33	1022.41	0.08

ZnO/Zn(OH)₂ ratio. For sulfur, we expect one dominant species (ZnS), and thus the S 2p_{3/2} binding energy is taken “as derived”. For Zn, finally, we argue that there are too many different species overlapping within the Zn 2p_{3/2} peak, and thus it is not possible to separate band bending effects from variations in relative abundance of the different species. We therefore list the binding energy values in Tab. 6.1, but do not use them for the band alignment determination (hence shaded gray in Tab. 6.1). Overall, we derive a shift of 0.20 eV for the buffer layer core levels. Note that the S and O core levels all shift in unison, suggesting that these shifts are due to band bending in the buffer layer, rather than to chemical shifts due to an altered S/(S+O) or OH/(O+OH) ratio in the buffer layer itself. This interpretation is corroborated by a quantitative analysis of the OH/(O+OH) ratio, which derives values for the 5 and 22.5 min Zn(O,S) samples [Chapter 7] that are equal within the error bars of such a determination.

The full band alignment of the Zn(O,S)/CIGSe interface, including the band bending correction, is depicted in Figure 6.3. A small conduction band offset (CBO = 0.09 ± 0.20 eV) is found, indicating that the conduction band alignment at the Zn(O,S)/CIGSe interface is essentially flat (small spike), as in^{25,52,59,143}. Likewise, a considerable valence band offset (VBO = 1.15 ± 0.15 eV) is formed, creating a hole barrier and decreasing interfacial recombination. Note that the error bars were determined as a best-faith estimate of the Gaussian distribution around the derived value (they should not be misinterpreted as a “box of equal probability”).

As mentioned in the introduction, we have consistently found flat conduction alignments in optimized CIG(S)Se-based devices^{25,52,59}, with the exception of CdS/Cu(In,Ga)S₂, for which a cliff was found⁵¹. Given the fact that the O/S ratio of the

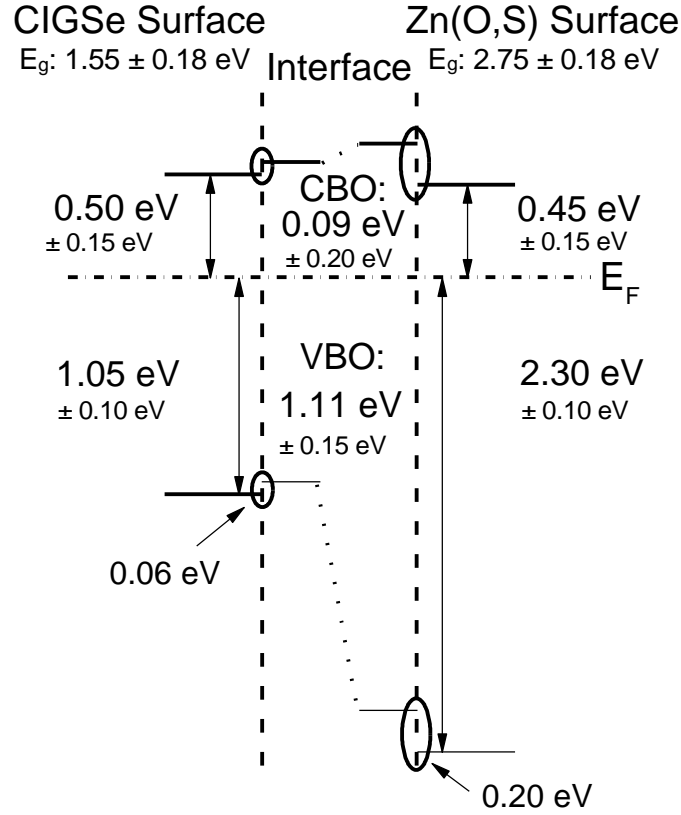


Figure 6.3: Band alignment scheme of the Zn(O,S)/CIGSe interface. The band edge positions at the CIGSe and Zn(O,S) surfaces are shown on the left and right, respectively. In the center, the band alignment at the interface is shown, taking interface-induced band bending changes at the absorber surfaces and band bending in the buffer layer into account (as indicated by the ovals).

Zn(O,S) layer gives an additional optimization parameter for this alternative buffer layer, it is not necessarily to be expected that a flat conduction band alignment is found. In particular, modeling studies have suggested that buffer/absorber interfaces are far less sensitive towards spikes than towards cliff arrangements^{68–70}. Nevertheless, empirical optimization time-and-again leads to electronic level alignments that are very close to “flat”, suggesting that such an optimized level alignment should be considered one of the primary design criteria for constructing deliberately-tailored thin film photovoltaic devices.

6.4 – CONCLUSION

The electronic structure of the Zn(O,S)/CIGSe interface was analyzed using x-ray, UV and inverse photoemission. We find evidence for multiple chemical environments of oxygen in the Zn(O,S) buffer layer, best described by ZnO and Zn(OH)₂ components. Detailed analysis of the bare CIGSe and thick Zn(O,S)/CIGSe samples, together with an optimally chosen thin Zn(O,S) intermediate sample to monitor variations of band bending due to interface formation and increasing buffer layer thickness, allowed for a comprehensive and all-experimental depiction of the electronic level alignment at the interface. We find an essentially flat conduction band alignment (small spike) and a significant valence band offset (i.e., a hole barrier). Such a structure is expected to allow for unobstructed electron transport across this interface, beneficial for high-efficiency thin film solar cells.

CHAPTER SEVEN

SOFT X-RAY SPECTROSCOPY OF A COMPLEX HETEROJUNCTION IN HIGH-EFFICIENCY THIN-FILM PHOTOVOLTAICS: INTERMIXING AND Zn SPECIATION AT THE Zn(O,S)/CIGSe INTERFACE

7.1 – INTRODUCTION

Cu(In,Ga)Se₂ (CIGSe) thin-film photovoltaic devices have recently achieved a world-record efficiency of 22.3% on a laboratory scale utilizing a Zn-based buffer layer (the 20.9% world-record cell from Solar Frontier K.K. utilized Zn(O,S) as the buffer layer)⁴. While CdS-based CIGSe devices have traditionally dominated the record efficiencies for this materials class,⁴⁵ other groups report high conversion efficiencies with a Zn(O,S) buffer as well (up to 21.0 %) ^{58,131,132,145}. An understanding of the interface formation is crucial for optimizing these buffer layers and the buffer/absorber interface. While several studies have been published showing theoretical and experimental interfacial band alignments,^{60,84,133,134,136,140} there is a need to better understand the chemical interactions at the buffer/absorber interface, as this information can aid in deliberately tailoring the electronic band alignment. We note that current state-of-the-art Zn(O,S)-based devices feature a flat conduction band alignment⁶⁰.

Previous studies have revealed a S/Se intermixing at the CdS/CIG(S)Se interface of high efficiency thin film devices with a chemical bath-deposited buffer layer^{48–50,146}. Only few studies report on intermixing at the heterojunction between Zn(O,S) and chalcopyrites^{139,147}. To gain better insights into the formation of the Zn(O,S)/CIGSe buffer layer and the chemical interactions at the interface in current state-of-the-art devices, we employ x-ray photoelectron spectroscopy (XPS), x-ray-excited Auger electron

spectroscopy (XAES), and synchrotron-based soft x-ray emission spectroscopy (XES) on Zn(O,S)/CIGSe samples with varying buffer layer thickness.

7.2– EXPERIMENTAL

The sample set was deposited at the National Renewable Energy Laboratory (NREL). It consists of a CIGSe bare absorber and three Zn(O,S)/CIGSe interface samples of varying Zn(O,S) chemical bath deposition (CBD) times¹⁴¹. The standard three-stage process, with a nominal Ga/(Ga+In) ratio of 0.3, was used to grow the CIGSe absorbers on Mo-sputtered glass¹⁸. The “thick” Zn(O,S) sample was deposited using the standard 22.5 min CBD process, and for the “thin” and “intermediate” samples, the process was interrupted after 5 and 10 min, respectively. Completed twin devices showed an average conversion efficiency of 17.7%. The CBD process yielded Zn(O,S) buffer films with a S/(S+O) ratio of ~0.56, as derived by Auger depth profiling studies conducted at NREL.

XPS and XAES were conducted at UNLV, while XES was performed at the Advanced Light Source (ALS), Lawrence Berkeley National Laboratory. XPS measurements were taken using Mg and Al K α radiation with a SPECS PHOIBOS 150 MCD electron analyzer and calibrated using the Auger and core-level peaks of clean Cu, Ag, and Au foils⁸⁰. The XES spectra were taken at the SALSA endstation¹⁰¹ on beamline 8.0.1 at the ALS, utilizing the variable line-space grating (VLS) spectrometer. The spectra were calibrated using the prominent emission features of CdS¹⁰⁸. The base pressure for the XPS and XES measurements were $<5 \times 10^{-10}$ and $<1 \times 10^{-9}$ mbar, respectively.

The samples were briefly air-exposed (less than 5 min) before being packaged in a vacuum-sealed container. At UNLV, the samples were immediately introduced into an

inert gas-filled glovebox, mounted on a sample holder, and transferred into the ultra-high vacuum system. The samples were measured “as-received” and also after a low-energy (50 eV) Ar⁺ ion treatment (two subsequent 60 min treatments for CIGSe, and three subsequent 20 min treatments for each of the 5 and 22.5 min absorbers) at low incidence angle, which has been shown to be effective in (partially) removing adsorbates from chalcopyrites, ZnO, and CdS surfaces without creating metallic phases often found with higher ion energies^{25,83}. XPS peaks were analyzed by fitting with Voigt functions, coupled Gaussian and Lorentzian widths, and a linear background using the Fityk Peak Fitting Program⁹⁰. For quantification, inelastic mean free paths (IMFPs) were determined by the QUASES software¹⁴⁸.

7.3– RESULTS AND DISCUSSION

XPS survey spectra of the bare CIGSe absorber and the 5 and 22.5 min Zn(O,S)/CIGSe samples are shown in Figure 7.1. The respective “as-received” spectra are shown in black, while the “ion-treated” spectra are shown in red. The pertinent CIGSe and Zn(O,S) photoemission and Auger lines (of Cu, In, Ga, Se, Zn, O, and S), as well as the Na lines are labeled, in addition to the adsorbate peak associated with C. For the as-received CIGSe absorber, the O 1s peak is particularly pronounced, especially when the photoionization cross section is taken into account^{149,150}. Due to the presence of this adsorbate layer, all high-binding energy peaks in the survey spectrum (e.g., Ga 2p, Cu 2p, In MNN, Zn 2p) are suppressed in intensity. The low-energy ion treatment removes the majority of the adsorbate species, as well as most of the Na surface species, and thus the surface-sensitive peaks mentioned above gain in intensity. The CIGSe absorber was

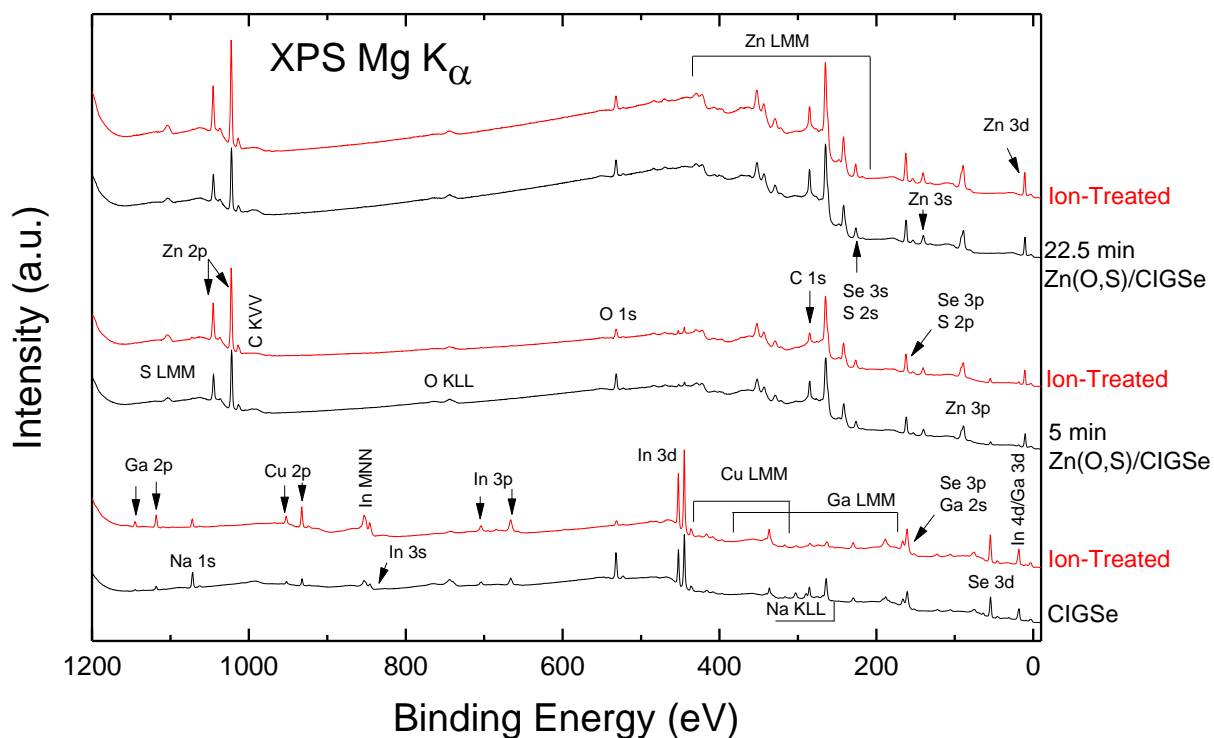


Figure 7.1: XPS survey spectra of the untreated (black) and ion-treated (red) Zn(O,S)/CIGSe sample series: CIGSe bare absorber (bottom), 5 min Zn(O,S) (center), and 22.5 min Zn(O,S) (top).

treated for a total of 120 min, and the Zn(O,S)/CIGSe samples were treated for a total of 60 min in several steps. In Fig. 7.1 and the subsequent analysis, data after the first 20 min treatment is shown/used in order to minimize ion beam influences. In fact, as will be discussed later, the two subsequent ion treatments of the Zn(O,S)/CIGSe samples induced signs of surface alteration (dehydrogenation). This indicates that Zn(O,S) is more susceptible to low-energy ion treatments (and other irradiation) than the CIGSe absorber, CdS, or ZnO^{25,83,142,143}. As the Zn(O,S) thickness is increased, Fig. 1 shows that all peaks from the CIGSe absorber surface are attenuated, as expected. Small CIGSe-related core-level peaks are detected in the spectra of the thin Zn(O,S)/CIGSe sample (e.g., the In 3d and Se 3d peaks in Fig. 1, center). In contrast, the 22.5 min Zn(O,S) sample shows no evidence of absorber-related peaks, suggesting that it is a continuous layer.

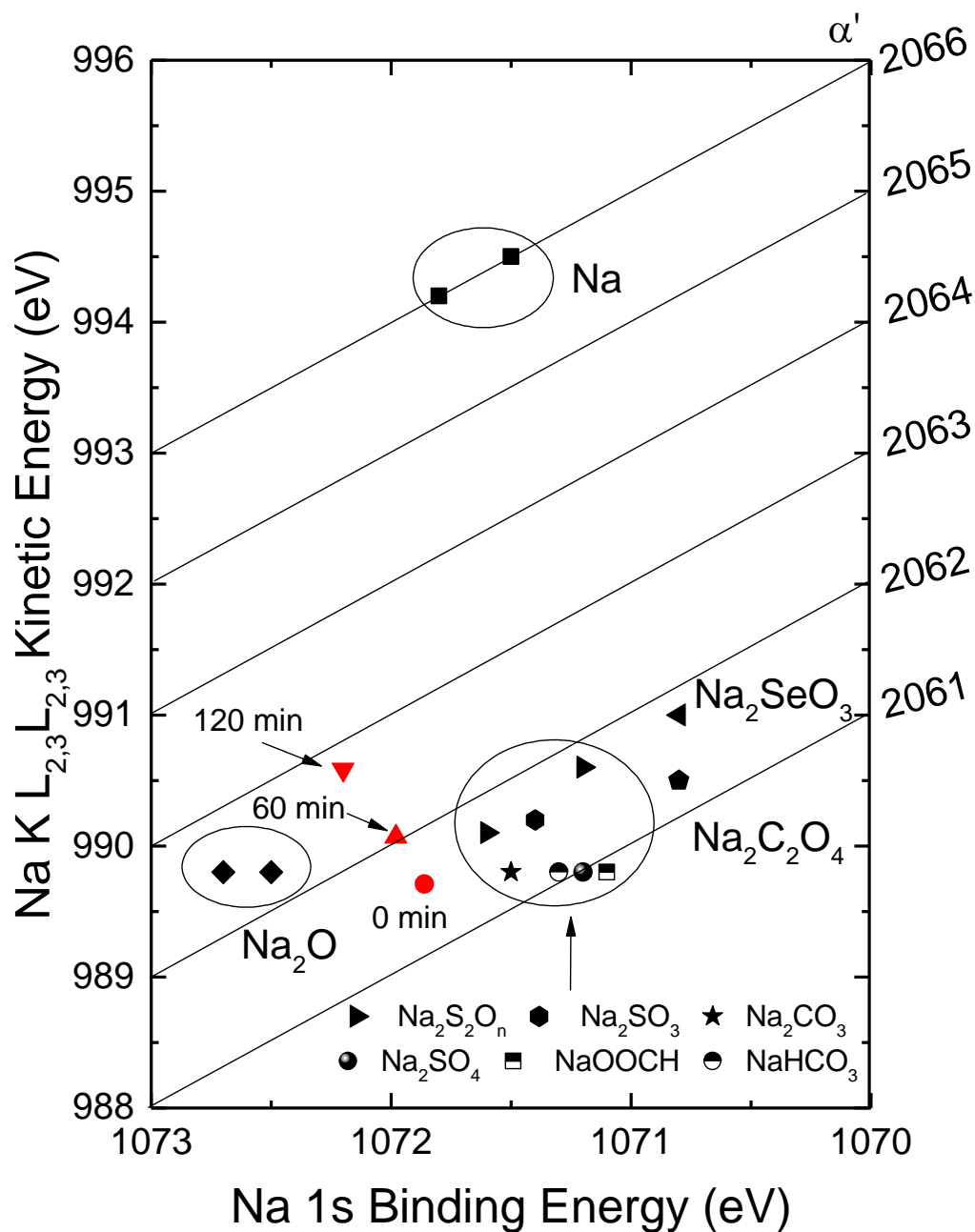


Figure 7.2: Modified Auger Parameter plot of Na 1s is shown before (red dot) and after different 50 eV Ar⁺-ion energy treatment steps (red triangles) in comparison to references (111,112) in black (error bars are ± 0.05 eV on both axes).

The Na peak intensity for the ClGSe bare absorber decreases with ion treatment, in parallel to a reduction of the oxygen and carbon signals [we note that the carbon signal for the Zn(O,S) layers is quite sizable, which we assign to an incorporation during the

CBD process]. To gain further insight into the chemical state of Na on the CIGSe surface and the cause of this intensity decrease, the modified Auger parameters α' of Na were calculated. Figure 7.2 shows the Wagner plot¹¹⁶ for the CIGSe absorber surface (red, ion-treatment times as indicated), along with relevant references (black)¹¹¹. The modified Auger parameter is calculated by summing the binding energy of the Na 1s core level and the kinetic energy of the KL_{2,3}L_{2,3} Auger peak, and information about the chemical state is gained by comparing with reference data¹¹⁶ along three axes: the Na 1s binding energy (abscissa), the Na KLL kinetic energy (ordinate), and α' (diagonal and right ordinate). The location of the CIGSe data on the Wagner plot is indicative of Na in an oxidized chemical environment. It is clearly different from metallic Na, but close to a large variety of O and/or C containing Na compounds. Thus, upon ion treatment, Na is likely to be desorbed along with the surface adsorbates. Based on earlier studies,^{35–38} this is not unexpected for air-exposed CIGSe surfaces and also assumed to happen in the chemical bath solution.

Core-level peaks from the CIGSe absorber can be detected in the spectra of the thin Zn(O,S)/CIGSe sample, indicating that the 5 min CBD of Zn(O,S) results in a layer that is inhomogeneous and/or thinner than the region from which XPS information can be derived (note that XPS signals are governed by an exponential attenuation function, not a “box” function associated with a specific information depth). The absorber peaks detected for Cu, In, and Ga are of low intensity, while, in comparison, the Se 3d peak is larger, indicating the possibility of Se diffusion into the Zn(O,S) layer, as will be discussed now. For the purpose of studying Se diffusion at this interface, we also include the Zn(O,S)/CIGSe sample of intermediate thickness (10 min CBD). Figure 7.3 shows XPS spectra of the Se 3d peak (left) and the Ga 3d/In 4d peak (right) for the CIGSe bare

absorber and the Zn(O,S)/CIGSe samples of increasing thickness. Due to their similar kinetic energies, the Se 3d, Ga 3d, and In 4d peaks are expected to have similar inelastic mean free paths (IMFPs), allowing the attenuation factors of these peaks to be compared as an initial step. The Se peak is strongly attenuated as the Zn(O,S) CBD time increases, but nevertheless it is still detectable even after the standard deposition time of 22.5 min. In contrast, the peaks of the 10 min Zn(O,S)/CIGSe and 22.5 min Zn(O,S)/CIGSe samples are extremely small (if present at all), even when magnified 100x (note that the

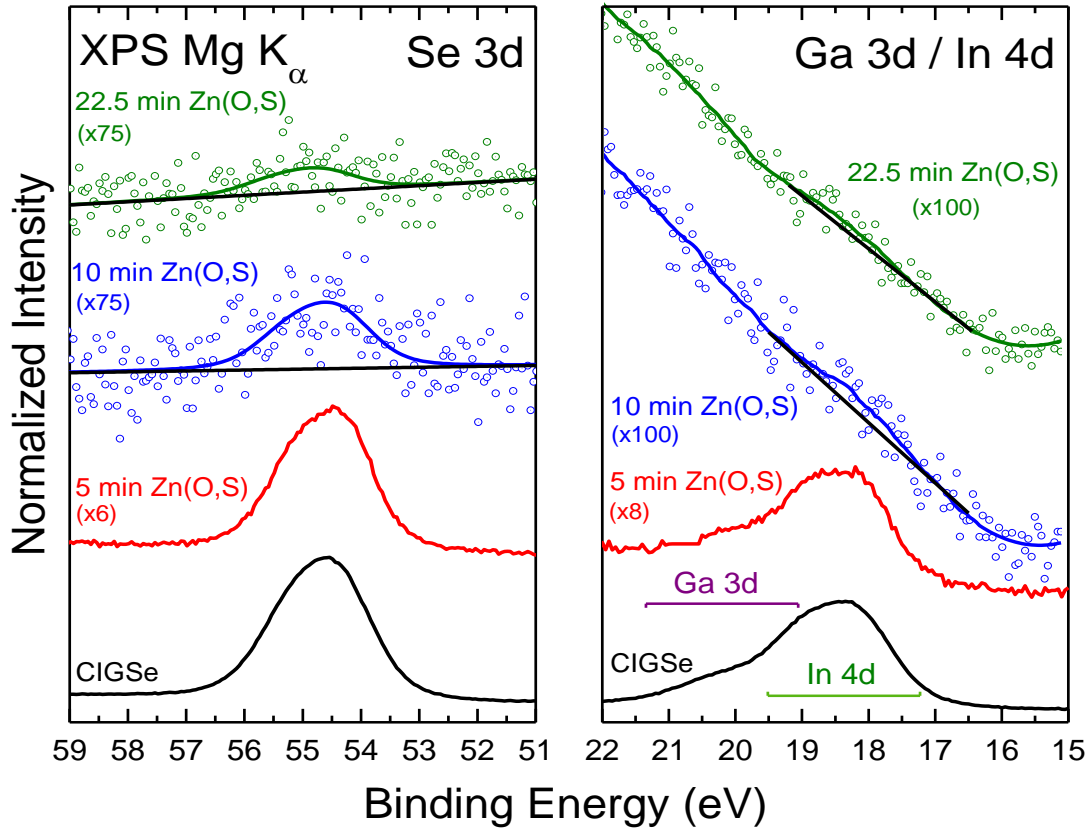


Figure 7.3: Mg K_α XPS spectra of the Se 3d peak (left) and the Ga 3d/In 4d region (right) for the CIGSe bare absorber and Zn(O,S)/CIGSe samples of varying thickness. To describe the 10 and 22.5 min spectra, the result of a fit with the CIGSe lineshape and a linear background is shown. Multiplication factors are shown in parentheses.

Ga 3d/In 4d peaks lie on the onset of the O 2s peak, at ~ 26 eV, giving rise to the steep background observed for the 10 and 22.5 min sample). The detection of a Se signal even after 22.5 min of Zn(O,S) CBD suggests an outdiffusion of Se during the CBD process, similar to the CdS/CIGSe and CdS/CIGSSe interfaces^{48–50}. All other core-level and Auger peaks (not shown) were analyzed in a similar fashion, but no peaks were visible for the 10 min and 22.5 min Zn(O,S) CBD sample (but note that these peaks might be governed by shorter attenuation lengths due to their lower kinetic energy and will be discussed in greater detail below).

In order to analyze the possibility of Se, Ga, and/or In diffusion more quantitatively, Figure 7.4 presents an “effective Zn(O,S) layer thickness” as a function of the Zn(O,S) CBD time. The nominal thickness values (determined by Scanning Electron Microscopy at NREL) are shown as black data points and a line, while the effective thicknesses derived from the Se 3d, Ga 3d, and In 4d intensity attenuation are plotted in color and labeled (red, green and pink colors: Ga 3d/In 4d, blue: Se 3d). If there is no diffusion of the element in question, the effective layer thickness should be similar to the nominal thickness, while it is expected to be lower in the case of diffusion into the buffer layer. The effective thickness derived for a given peak is calculated using

$$d_{eff} = \lambda \ln(I_0 / I). \quad (7.1)$$

The IMFP is represented by λ , I_0 is the peak intensity in the bare absorber, and I is the peak intensity in the corresponding Zn(O,S)/CIGSe sample. We find that the Se 3d-based effective layer thickness lies significantly below the nominal thickness line, even when taking the error bars into account. Thus, the attenuation of the Se signal is lower than expected, suggesting that Se is diffusing into the buffer layer during the CBD

process. In contrast, for the 5 min sample, the Ga 3d and In 4d effective thicknesses are larger and on (Ga) or very close (In) to the nominal line. For the 10 min sample, we note

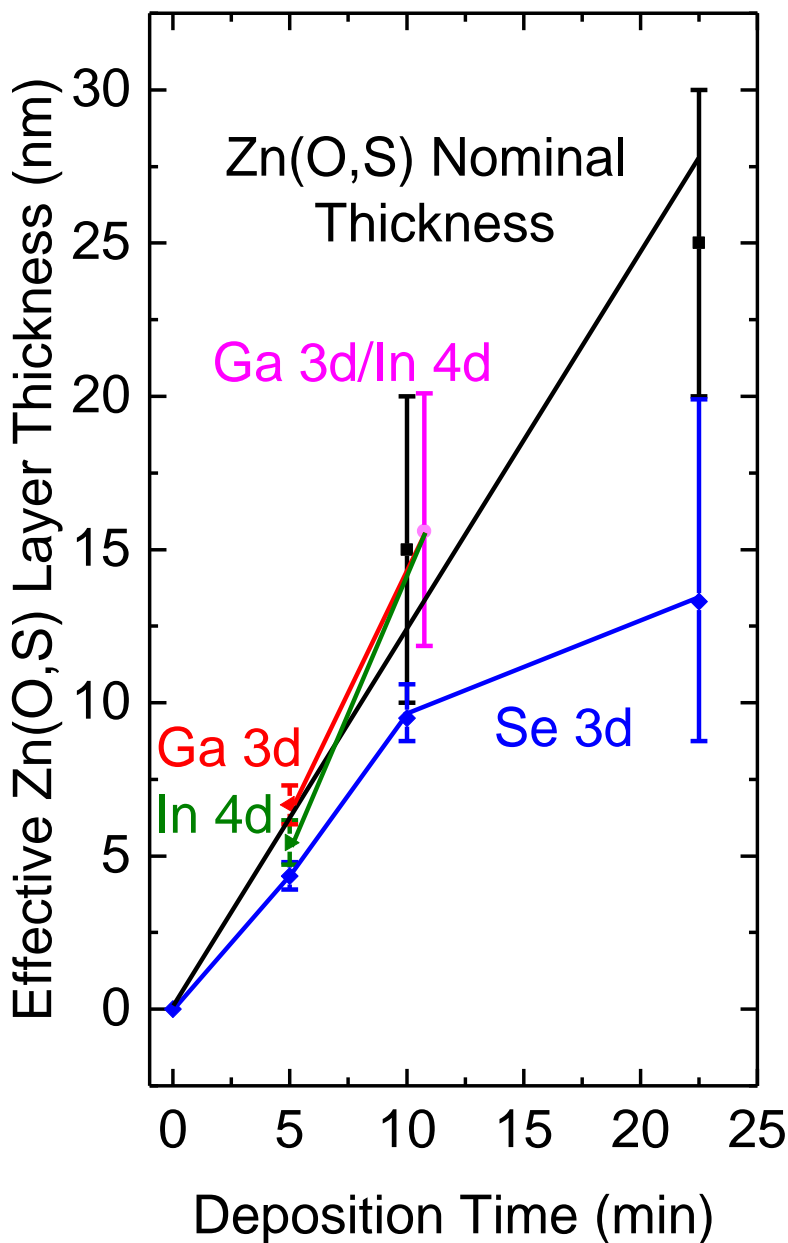


Figure 7.4: Effective Zn(O,S) layer thickness derived from Se 3d (blue), Ga 3d (red, 5 min), In 4d (green, 5 min), Ga 3d/In 4d combined (pink, 10 min) and nominal thickness (black) as a function of Zn(O,S) CBD time. The 10 min nominal thickness and Ga 3d/In 4d data were shifted slightly along the abscissa to differentiate between the data points.

that the Ga 3d/In 4d region also includes the Mg K_{β} excitation of the O 2s line, which would give rise to a satellite approximately 9 eV lower than the O 2s peak (~ 17 eV), and/or contributions from inelastically scattered Zn 3d electrons (peak at ~ 10 eV). Nevertheless, because the peak in the Ga 3d/In 4d region is clearly present for the 10 min sample, we show the effective layer thickness based on the attenuation of the combined Ga 3d/In 4d peak (pink), ignoring possible O 2s or Zn 3d are contributions (leading to a large and asymmetric error bar). The effective layer thickness is again close to the nominal thickness line, suggesting that there is no significant diffusion of In or Ga into the buffer.

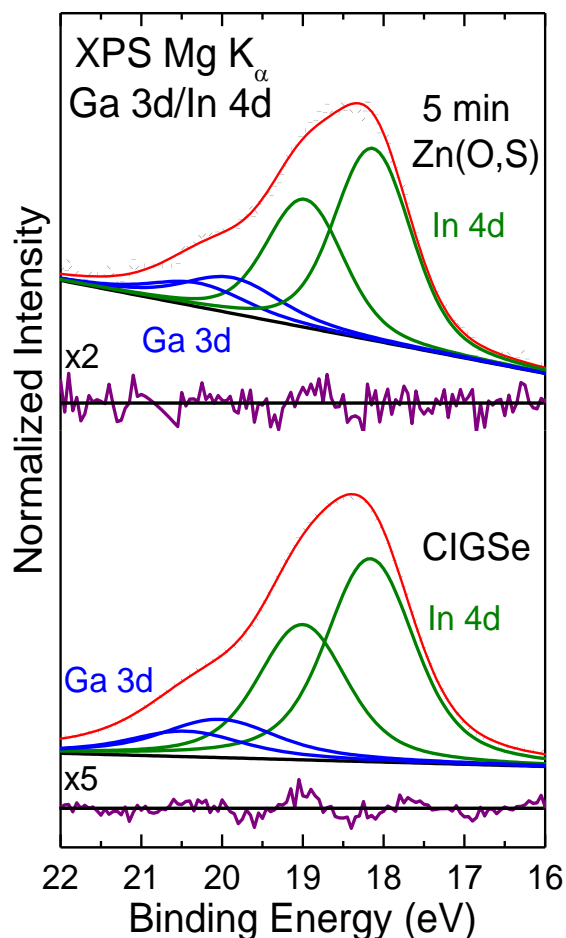


Figure 7.5: XPS detail spectra of the Ga 3d/In 4d region of the CIGSe absorber (bottom) and 5 min Zn(O,S) (top). Fit curves for In:Ga contributions to the peak are shown along with their respective residuals (purple).

For the 22.5 min sample, we argue that there is no detectable Ga 3d/In 4d peak, noting the absence of the (normally dominant) In 3d_{5/2} peak. The finding of a Se outdiffusion into the Zn(O,S) buffer layer is reminiscent of the CdS/CIGSe interface, in which a pronounced S-Se exchange at the interface is found^{48–50}. In the present case of a Zn(O,S) buffer, the diffusion of Se into the buffer layer leads us to speculate that it is most likely in a Zn-Se bonding environment.

Figure 7.5 shows fits of the Ga 3d/In 4d peaks of the bare CIGSe absorber and the 5 min Zn(O,S) sample in order to see if the Ga/(Ga+In) ratio at the absorber surface changes with the addition of the buffer layer. The peaks were fit with a linear background and Voigt profiles, using coupled Gaussian widths for all components, and coupled but separate Lorentzian widths for In and Ga, respectively. The ratios of the spin-orbit split peaks were fixed according to their multiplicity, along with their respective peak separation, 0.86 eV for In^{113,114} and 0.46 eV for Ga¹¹⁵. The data is shown with black dots, the In 4d components in green, the Ga 3d components in blue, and the resulting fit in red. The residual of the fit is shown below each spectrum (purple). We note that these shallow core levels already possess some band character, and thus the quality of the fit is very surprisingly high, especially given all the above-mentioned boundary conditions included in the fit. The surface Ga/(Ga+In) ratio for the CIGSe absorber and 5 min Zn(O,S)/CIGSe samples are 0.33 and 0.32 (± 0.10), respectively, indicating no change in the surface ratio with the addition of the buffer layer. Having thus gained a detailed description of the absorber surface, we can now take a closer look at the overlayer and its contributions to the interface formation.

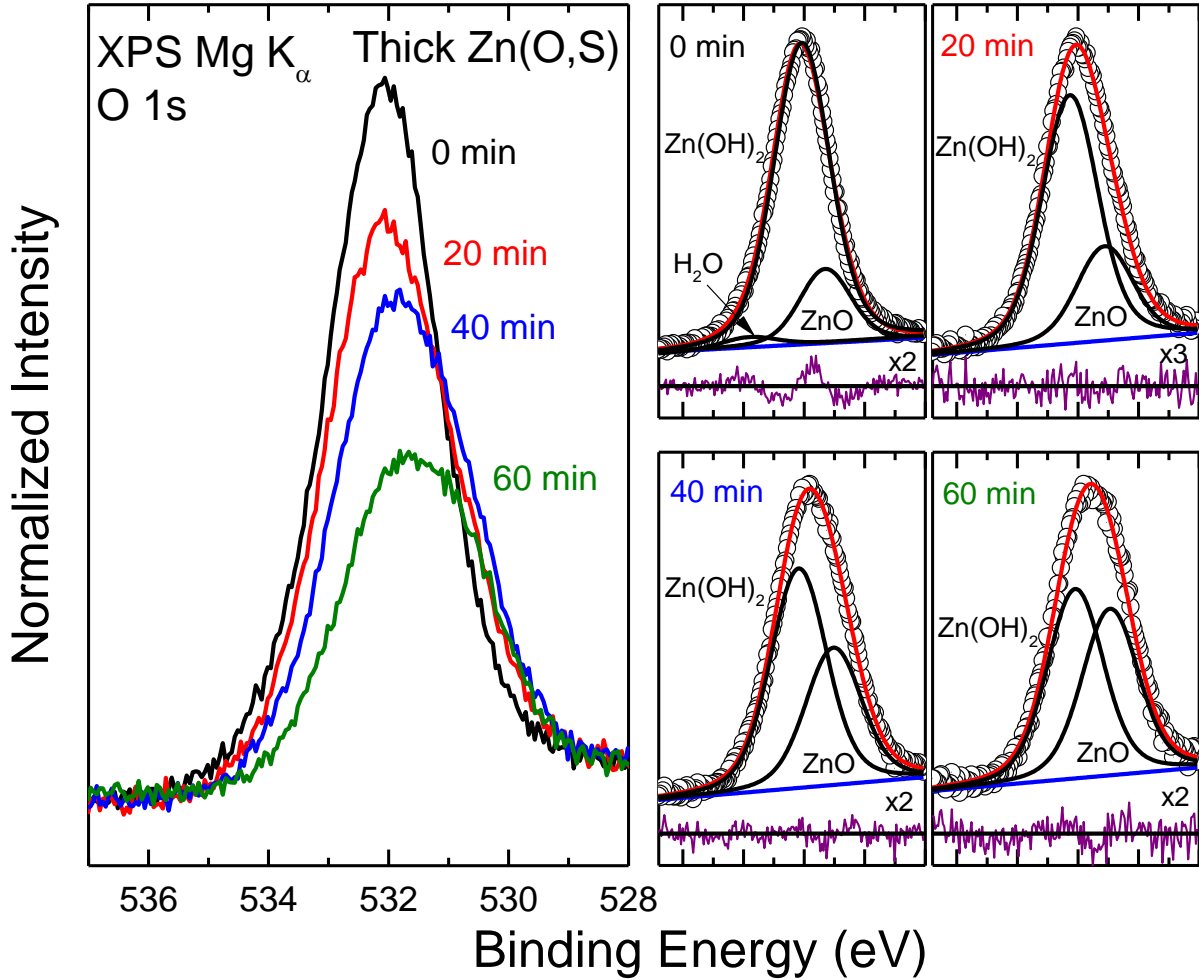


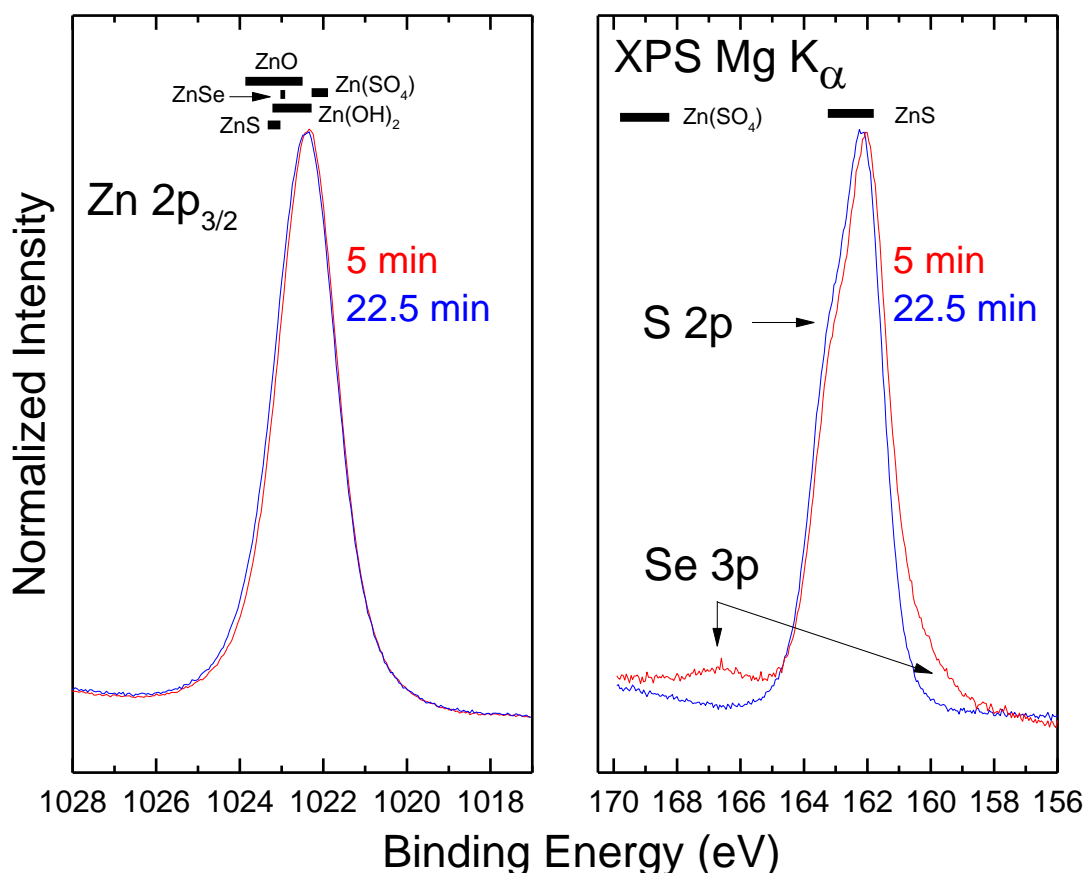
Figure 7.6: (Left) XPS spectra of the 22.5 min Zn(O,S) O 1s peak as a function of ion treatment time. (Right) Fits of the O 1s peak show a change in OH/(OH+O) ratio as a function of ion treatment time.

As mentioned previously, the 5 and 22.5 min Zn(O,S)/CIGSe samples were ion treated in three 20 min increments. Figure 7.6 (left) shows XPS spectra of the 22.5 min Zn(O,S)/CIGSe O 1s peak as a function of ion treatment time. The purpose of the low energy ion treatment is to remove surface adsorbates without creating metallic species at the surface. Indeed, we see that with the 20 min treatment, the O peak is reduced (partial removal of adsorbates) and the main peak position is identical to the untreated surface. However, with each subsequent treatment, the peak shifts toward lower BE and

the shape changes as well. This is also true for the Zn and S peaks (not shown): the untreated and 20 min treated surface peak positions are identical, and with each subsequent treatment, the peak shifts to lower BE. The broadness and shape of the O 1s peak suggest that there are multiple chemical species of O in the (untreated) Zn(O,S) film. On the right of Figure 7.6, a fit analysis of the peak (as a function of ion treatment) shows that at least three species are present at the untreated surface, and at least two O species after each treatment. The peaks were normalized to peak height in order to easily visualize changes in peak component ratios. The peaks were fit with a linear background, identical Gaussian and Lorentzian widths, and fixed positions for all species. The residuals shown below the spectra indicate that the quality of the fit is quite high for the ion-treated surfaces. In contrast, the untreated O 1s peak shows a characteristic oscillation, which can be reduced by decoupling the Lorentzian width of this fit from that of the other three spectra. We thus derive that the spectrum of the untreated surface is a convolution of at least three species. Because there is a reduction in the O 1s peak intensity with the first ion treatment step, we believe that such additional species need to be ascribed to surface adsorbates. Based on their binding energies, the three components for the untreated peak are assigned to H₂O, Zn(OH)₂, and ZnO^{111,112}. For the treated peaks, the components are assigned to Zn(OH)₂ and ZnO only. The presence of Zn(OH)₂ suggests that the dehydrogenation of the Zn(O,S) layer during deposition is incomplete, indicating that a better description of this layer would be “Zn(O,OH,S)”. Also, it cannot be ruled out that Zn(OH)₂ might be formed at the surface during the (brief) air exposure. The fits of the O 1s peaks show that, with increasing ion treatment time, the OH/(O+OH) ratio changes - a reduction in Zn(OH)₂ and an increase in ZnO suggests that

the Zn(O,S) surface is more susceptible to the low-energy ion treatment than, e.g., the ZnO surface commonly used as a window layer CIGSe devices. This beam-induced dehydrogenation is not unexpected, as similar results have been found utilizing intense x-rays and electron flood gun irradiation on Zn(OH)₂-rich samples^{142,143}. Nevertheless, we use data from the 20 min ion treatment for our analysis because this surface represents the best compromise between reduced contributions from surface adsorbates and minimal ion beam damage.

The Zn 2p_{3/2} and S 2p/Se 3p spectra for the 5 and 22.5 min Zn(O,S)/CIGSe samples are shown in Figure 7.7, along with the binding energy markers for several



Figures 7.7: XPS spectra of the Zn 2p_{3/2} peak (left) and S 2p/Se 3p peaks (right) for the 5 and 22.5 min Zn(O,S) samples. Reference peak positions (111,112) are indicated above both peaks.

references^{111,112}. Because the binding energies of the Zn references overlap (left), and because the observed peak is rather broad, it does not allow for an unambiguous assignment of the different species. This is not necessarily surprising – so far, our analysis has suggested three bonding partners for Zn, namely O and OH from the O 1s peak fit and Se from the diffusion analysis. Furthermore, bonding to sulfur is also expected for the Zn(O,S) film surfaces. The S 2p/Se 3p spectra (right) show (a) the presence of sulfur in a sulfide environment, as expected, (b) the presence of Se for the 5 min samples (as discussed above; note that the Se 3p peak is much weaker than the Se 3d peak, and hence it is not seen for the 22.5 min sample), and (c) no evidence for sulfates on the surface.

XES spectra of the S L_{2,3} and Se M_{2,3} emission as a function of Zn(O,S) CBD time, excited non-resonantly with a photon energy of 180 eV, are presented in Figure 7.8. The CIGSe spectrum shows the Se M_{2,3} emission, while the Zn(O,S)/CIGSe samples are dominated by S L_{2,3} emission. The magnification factors at the right hand side of each spectrum show that the Se M_{2,3} is significantly weaker than the S L_{2,3} emission. The intensity differences between the Se M_{2,3} and S L_{2,3} emission is due to the difference in fluorescence yield for the S 3s to S 2p transition (S L_{2,3}) and the Se 4s to Se 3p transition (Se M_{2,3}). As the Zn(O,S) layer is deposited, the characteristic spectrum of ZnS emerges. In particular, the two features at ~151.2 and ~152.4 eV (in the ZnS reference) are associated with electrons from the Zn 3d-derived band decaying into the S 2p_{1/2} and S 2p_{3/2} core holes. We do note that the Zn 3d-derived features are slightly shifted towards lower emission energies (by ~0.2 eV), indicating a different Zn chemical environment due to the presence of multiple Zn species (ZnS, ZnSe, Zn(OH)₂, and ZnO). There is no

evidence of sulfates, as seen by the lack of a dominant peak at ~ 161 eV,^{143,151} in contrast to a photoinduced sulfate formation observed for ILGAR-Zn(O,OH)/CIGSSe^{143,151}.

To gain insights into the component(s) contributing to the 5 min and 10 min spectra, the 22.5 min spectrum (i.e., the S L_{2,3} emission of the Zn(O,S) overlayer) was subtracted after normalizing all spectra to overall peak area. The resulting difference spectra are presented in Figure 7.9-a (bottom). The 5 min difference (red) and the 10 min difference (blue) both show a dip at ~ 147.5 eV and a maximum at 150 eV, which we interpret as a

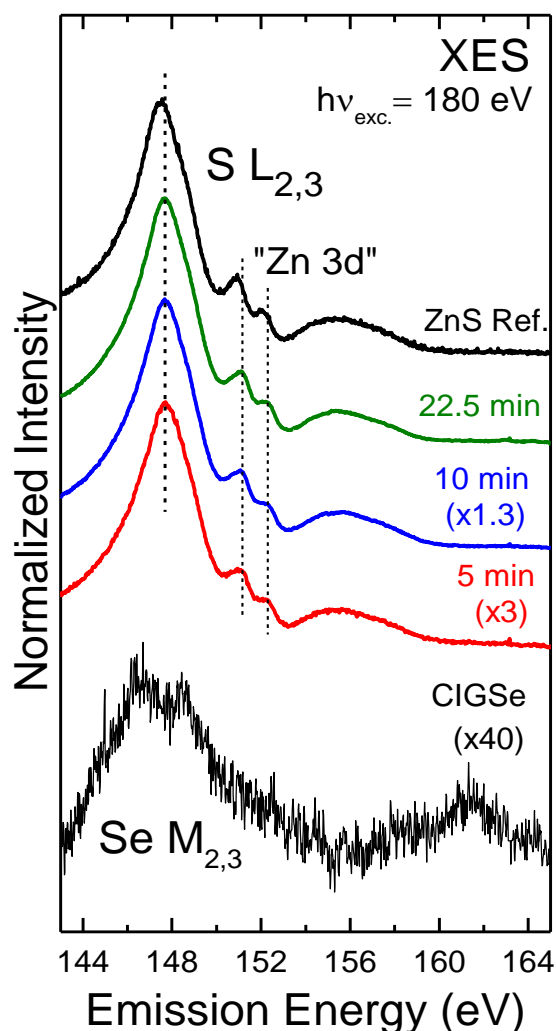


Figure 7.8: S L_{2,3} and Se M_{2,3} emission of the Zn(O,S)/CIGSe interface as a function of CBD time and a ZnS reference. Multiplication factors are shown in parentheses.

spectral-weight shift of the main S $L_{2,3}$ peak. Comparison with reference compounds (Ga_2S_3 , In_2S_3 , CuInS_2 , CuS , Cu_2S , and Zn(O,S) , Figure 7.9-b) suggests that this could be indicative for a different chemical environment of the sulfur atoms near the substrate. Furthermore, we observe a maximum at ~ 153.5 eV; at this energy, Ga_2S_3 , In_2S_3 , and CuInS_2 all exhibit additional partial density of states. A strong contribution of S-Cu bonds can, however, likely be ruled out due to the absence of any spectral difference at ~ 159 eV (i.e., the region of the Cu 3d contributions in CuInS_2 and the Cu sulfides). The

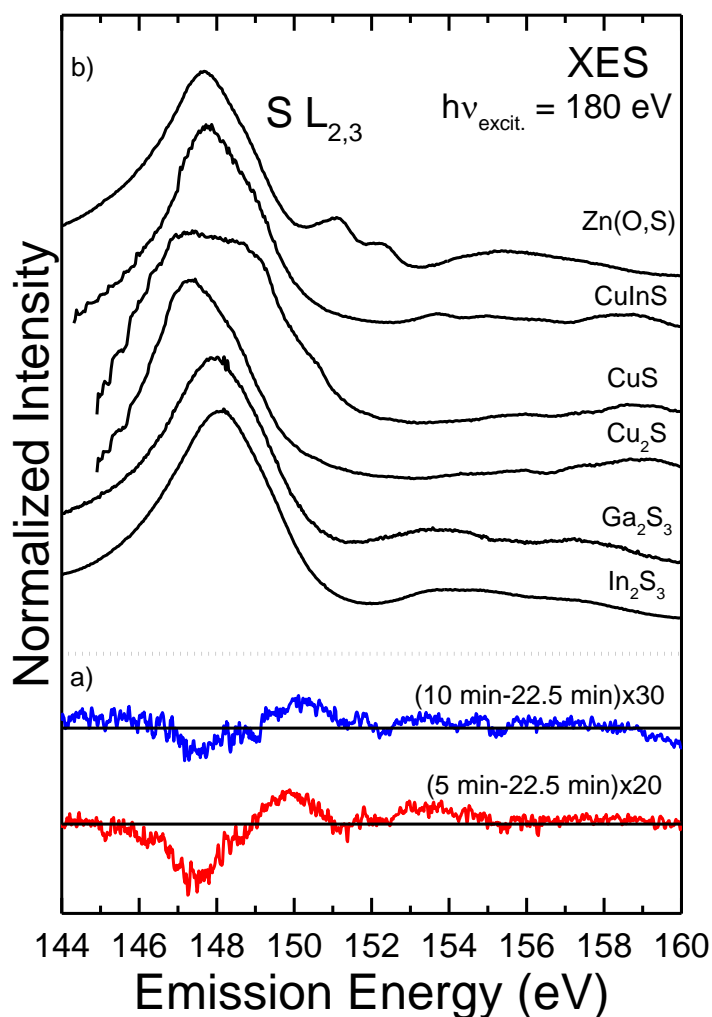


Figure 7.9: a) Difference spectra from subtracting the 22.5 min Zn(O,S) S $L_{2,3}$ emission from the 5 min (red) and 10 min (blue) spectra. b) Reference spectra for comparison.

difference spectra thus suggest that, in addition to the Zn-S bonding environment in the Zn(O,S) buffer layer, additional S chemical bonding environments are present at the interface to the CIGSe absorber, most likely in an S-In and/or S-Ga bonding environment, similar to what has been previously observed for the CdS/CIGSe interface⁴⁸.

7.4– CONCLUSION

The Zn(O,S)/CIGSe interface has been investigated using XPS, XAES, and XES to investigate the chemical structure. Detailed analysis of the bare CIGSe absorber and Zn(O,S)/CIGSe samples of varying CBD times allowed for a comprehensive analysis of the chemical interactions at this interface. We find evidence for an upward diffusion of Se into the buffer layer, most likely in a Zn-Se environment, and intermixing of S at the interface, most likely in a S-Ga and/or S-In environment. We find multiple chemical environments of Zn, best described by ZnO, Zn(OH)₂, ZnS, and ZnSe. There is no evidence for sulfates in the Zn(O,S) layer (photoinduced or otherwise), but we do find evidence for Ar⁺ ion beam-induced dehydrogenation of the Zn(O,S) layer. The resulting chemical interactions during the Zn(O,S)/CIGSe interface formation are found to be quite similar to those at the CdS/CIGSe interface^{48–50} but feature a higher degree of complexity with respect to the local chemical environment of the group II component.

CHAPTER EIGHT

SUMMARY

In this dissertation, the impact of novel deposition parameters on both industry-manufactured and lab-based chalcopyrites are investigated and presented. The two new “hot topics” of the chalcopyrite photovoltaic field include the use of KF post-deposition treatments and alternative buffer layers. To provide insight on these novel pathways to high efficiency CIGSe devices, XPS, UPS, IPES, as well as XES and XAES are utilized to investigate multiple sample sets designed to create a thorough approach that offers insight on the electronic and chemical structures of the treated absorbers and/or the absorber/buffer interface. The purpose of this is to aid in the further optimization of high efficiency CIGSe thin-film photovoltaics.

Chapters 4 and 5 explore the effects of the first “hot topic”, alkali-treatments, on CIGSe absorbers. The absorbers presented in Chapter 4 were taken from the production line of STION and the National Renewable Energy Laboratory. In general, the alkali-treatments on these absorbers are shown to partially remove surface adsorbates, change the surface Cu:In (STION and NREL), Se:In (STION and NREL), and Ga/(Ga+In) ratios (NREL). The treatments deposit K, F, and/or Na on the surface and changes to the S/Se ratios are seen for the STION absorbers. Alkali-treatments change the VBM position and large differences are found between high efficiency KF samples and low efficiency KF samples. This indicates the KF-treatment process does not affect the substrate homogeneously. While trends were similar within the STION and NREL absorber sets separately, the alkali-treatments do not affect the STION and NREL absorbers the same.

Chapter 5 investigates effects of KF treatments when incorporated utilizing

different deposition techniques and SiO₂ barriers deposited on the soda-lime glass. We find that the Cu:In ratio is smallest for both KF PDT suggesting that the KF PDT leads to a depletion of Cu from the surface of nominally stoichiometric films. Both K and F are deposited on the surfaces of the KF PDT absorbers, and K and F are also observed the surface of the CKIGSe film, but to a smaller degree. In-F and Ga-F species are found on the ion-treated surfaces of both KF PDT absorbers. After the NH₄OH treatment, the Ga-F and Ga-O bonds are removed, and a Ga depletion of the surfaces is observed. In-F bonds are greatly reduced, but still present, and the contribution of In-O species is enhanced. The NH₄OH treatment also removes the K completely from the surface of KF PDT/SiO₂, significantly reduces K and F on KF PDT, and slightly reduces K and F for CKIGSe. Na is present on CIGSe, KF PDT, and CKIGSe pre and post-rinse but Na is only observed for the SiO₂ absorbers after the NH₄OH rinse, suggesting that Na is deposited during the NH₄OH treatment. The Na on all the absorbers are found in an Na-O bonding environment. UPS and IPES show that incorporation of K widens the bandgap of the CIGSe absorber, with the largest surface bandgap (among the rinsed samples) of 2.93 ± 0.15 eV found for the KF PDT/SiO₂ absorbers.

The second “hot topic” leading to high efficiency and world-record CIGSe devices is the use of alternative buffer layers, most notable Zn(O,S), a material offering the possibility of increasing the current collection in the shorter wavelength region of the solar spectrum. To further optimize these photovoltaic devices, an understanding of the interactions between the absorber and the buffer layer is crucial and this investigation is presented in Chapters 6 and 7. Chapter 6 presents the electronic structure of the Zn(O,S)/CIGSe interface utilizing XPS to monitor variations of band bending due to

interface formation and increasing buffer layer thickness, UPS to measure the valence band maximums, and IPES to measure the conduction band minimums of the samples. The interfacial band alignment features an essentially flat conduction band offset (0.09 ± 0.20 eV) and a significant valence band offset (1.11 ± 0.15 eV) acting as a hole barrier. Such an alignment allows for unobstructed electron transport and limits the interfacial recombination, beneficial for high-efficiency thin film solar cells. In addition to the band alignment, multiple chemical environments for O are found in the Zn(O,S) buffer layer best described by ZnO and Zn(OH)₂ components, further investigated in Chapter 7.

Chapter 7 presents the chemical structure of the Zn(O,S)/CIGSe interface with evidence for the diffusion of Se upward into the buffer layer, most likely in a Zn-Se bonding environment. S also intermixes at the interface, most likely creating Ga-S and/or In-S species. With the interfacial intermixing, evidence indicates multiple bonding environments of Zn, best described by ZnO, Zn(OH)₂, ZnS, and ZnSe. Overall, the resulting chemical interactions at the Zn(O,S)/CIGSe interface are very similar to the chemical interactions at the CdS/CIGSe interface.

APPENDIX

LIST OF ABBREVIATIONS AND SYMBOLS

α'	Modified Auger Parameter
ACS	American Chemical Society
ALS	Advanced Light Source
AM 1.5	Air-mass 1.5
B	Boron
BE	Binding energy
CB	Conduction band
CBD	Chemical bath deposition
CBM	Conduction band maximum
CdS	Cadmium Sulfide
CdTe	Cadmium Telluride
CIGSe	$\text{Cu}(\text{In}_{1-x}\text{Ga}_x)\text{Se}_2$
CIGSSe	$\text{Cu}(\text{In}_{1-x}\text{Ga}_x)(\text{S},\text{Se})_2$
DI	De-ionized
E_F	Fermi level
E_g	Band gap
E_{vac}	Vacuum level
FAT	Fixed Analyzer Transmission
FWHM	Full width at half maximum
HOPE	Hands on Photovoltaic Experience
$h\nu$	Photon energy
ILGAR	Ion laser gas reaction
IMFP	Inelastic Mean Free Path
IPES	Inverse Photoemission Spectroscopy
KE	Kinetic energy
KF	Potassium Fluoride
NaF	Sodium Fluoride
NREL	National Renewable Energy Laboratory

ODC	Ordered defect compound
PDIL	Process development and integration laboratory
PDT	Post-deposition treatment
PV	Photovoltaic
PVD	Physical Vapor Deposition
Si	Silicon
SURE	Summer Undergraduate Research Experience
TCO	Transparent conductive oxide
UHV	Ultra-high Vacuum
UPS	Ultra-violet Photoelectron Spectroscopy
VB	Valence band
VBM	Valence band maximum
Φ	Work Function
XAES	X-ray Auger Electron Spectroscopy
XES	X-ray Emission Spectroscopy
XPS	X-ray Photoelectron Spectroscopy
ZnO	Zinc Oxide
Zn(OH ₂)	Zinc Hydroxide
Zn(O,S)	Zinc Oxysulfide
ZnS	Zinc Sulfide
ZnSe	Zinc Selenide

REFERENCES

- (1) This Month in Physics History
<http://www.aps.org/publications/apsnews/200904/physicshistory.cfm> (accessed Oct 21, 2015).
- (2) Green, M. A.; Emery, K.; Hishikawa, Y.; Warta, W.; Dunlop, E. D. Solar Cell Efficiency Tables (Version 46). *Prog. Photovolt. Res. Appl.* **2015**, 23 (7), 805–812.
- (3) Shay, J. L.; Wagner, S.; Kasper, H. M. Efficient CuInSe₂/CdS Solar Cells. *Appl. Phys. Lett.* **1975**, 27 (2), 89–90.
- (4) <http://www.solar-frontier.com/eng/news/2015/C051171.html> (accessed Dec 10, 2015).
- (5) Shockley, W.; Queisser, H. J. Detailed Balance Limit of Efficiency of P-n Junction Solar Cells. *J. Appl. Phys.* **1961**, 32 (3), 510–519.
- (6) Vos, A. D. Detailed Balance Limit of the Efficiency of Tandem Solar Cells. *J. Phys. Appl. Phys.* **1980**, 13 (5), 839.
- (7) Pierret, R.F. Semiconductor Device Fundamentals 2nd Edition
- (8) Repins, I.; Contreras, M. A.; Egaas, B.; DeHart, C.; Scharf, J.; Perkins, C. L.; To, B.; Noufi, R. 19.9%-Efficient ZnO/CdS/CuInGaSe₂ Solar Cell with 81.2% Fill Factor. *Prog. Photovolt. Res. Appl.* **2008**, 16 (3), 235–239.
- (9) Kaufmann, C. A.; Neisser, A.; Klenk, R.; Scheer, R. Transfer of Cu(In,Ga)Se₂ Thin Film Solar Cells to Flexible Substrates Using an in Situ Process Control. *Thin Solid Films* **2005**, 480–481, 515–519.
- (10) Chirilă, A.; Reinhard, P.; Pianezzi, F.; Bloesch, P.; Uhl, A. R.; Fella, C.; Kranz, L.; Keller, D.; Gretener, C.; Hagendorfer, H.; Jaeger, D.; Erni, R.; Nishiwaki, S.; Buecheler, S.; Tiwari, A. N. Potassium-Induced Surface Modification of Cu(In,Ga)Se₂ Thin Films for High-Efficiency Solar Cells. *Nat. Mater.* **2013**, 12 (12), 1107–1111.
- (11) Caballero, R.; Kaufmann, C. A.; Eisenbarth, T.; Unold, T.; Klenk, R.; Schock, H.-W. High Efficiency Low Temperature Grown Cu(In,Ga)Se₂ Thin Film Solar Cells on Flexible Substrates Using NaF Precursor Layers. *Prog. Photovolt. Res. Appl.* **2011**, 19 (5), 547–551.
- (12) Nishiwaki, S.; Kohara, N.; Negami, T.; Wada, T. MoSe₂ Layer Formation at Cu(In,Ga)Se₂/Mo Interfaces in High Efficiency Cu(In_{1-x}Ga_x)Se₂ Solar Cells. *Jpn. J. Appl. Phys.* **1998**, 37 (Part 2, No. 1A/B), L71–L73.
- (13) Bär, M.; Weinhardt, L.; Heske, C.; Nishiwaki, S.; Shafarman, W. N. Chemical Structures of the Cu(In,Ga)Se₂/Mo and Cu(In,Ga)(S,Se)₂/Mo Interfaces. *Phys. Rev. B* **2008**, 78 (7), 75404.
- (14) Weinhardt, L.; Blum, M.; Bär, M.; Heske, C.; Fuchs, O.; Umbach, E.; Denlinger, J. D.; Ramanathan, K.; Noufi, R. Chemical Properties of the Cu(In,Ga)Se₂/Mo/glass Interfaces in Thin Film Solar Cells. *Thin Solid Films* **2007**, 515 (15), 6119–6122.

- (15) Bär, M.; Nishiwaki, S.; Weinhardt, L.; Pookpanratana, S.; Shafarman, W. N.; Heske, C. Electronic Level Alignment at the Deeply Buried absorber/Mo Interface in Chalcopyrite-Based Thin Film Solar Cells. *Appl. Phys. Lett.* **2008**, *93* (4), 42110-042110–042113.
- (16) Pettersson, J.; Törndahl, T.; Platzer-Björkman, C.; Hultqvist, A.; Edoff, M. The Influence of Absorber Thickness on Cu(In,Ga)Se₂ Solar Cells With Different Buffer Layers. *IEEE J. Photovolt.* **2013**, *3* (4), 1376–1382.
- (17) Gloeckler, M.; Sites, J. R. Potential of Submicrometer Thickness Cu(In ,Ga)Se₂ Solar Cells. *J. Appl. Phys.* **2005**, *98*, 103703–103703.
- (18) Contreras, M. A.; Egaas, B.; Ramanathan, K.; Hiltner, J.; Swartzlander, A.; Hasoon, F.; Noufi, R. Progress toward 20% Efficiency in Cu(In,Ga)Se₂ Polycrystalline Thin-Film Solar Cells. *Prog. Photovolt. Res. Appl.* **1999**, *7* (4), 311–316.
- (19) https://www.researchgate.net/figure/277695065_fig3_Figure-75-Sketch-of-the-three-stage-process-Values-are-given-for-information (accessed May 9, 2016).
- (20) Markvart, T.; Castañer, L. *Practical Handbook of Photovoltaics: Fundamentals and Applications*; Elsevier, **2003**.
- (21) Contreras, M. A.; Tuttle, J.; Gabor, A.; Tennant, A.; Ramanathan, K.; Asher, S.; Franz, A.; Keane, J.; Wang, L.; Scofield, J.; Noufi, R. High Efficiency Cu(In,Ga)Se₂-Based Solar Cells: Processing of Novel Absorber Structures. In *IEEE Photovoltaic Specialists Conference - 1994*; Vol. 1, pp 68–75 vol.1.
- (22) Kemell, M.; Ritala, M.; Leskelä, M. Thin Film Deposition Methods for CuInSe₂ Solar Cells. *Crit. Rev. Solid State Mater. Sci.* **2005**, *30* (1), 1–31.
- (23) Bär, M.; Nishiwaki, S.; Weinhardt, L.; Pookpanratana, S.; Fuchs, O.; Blum, M.; Yang, W.; Denlinger, J. D.; Shafarman, W. N.; Heske, C. Depth-Resolved Band Gap in Cu(In,Ga)(S,Se)₂ Thin Films. *Appl. Phys. Lett.* **2008**, *93* (24), 244103-244103–3.
- (24) Schmid, D.; Ruckh, M.; Grunwald, F.; Schock, H. W. Chalcopyrite/defect Chalcopyrite Heterojunctions on the Basis of CuInSe₂. *J. Appl. Phys.* **1993**, *73* (6), 2902–2909.
- (25) Morkel, M.; Weinhardt, L.; Lohmüller, B.; Heske, C.; Umbach, E.; Riedl, W.; Zweigart, S.; Karg, F. Flat Conduction-Band Alignment at the CdS/CuInSe₂ Thin-Film Solar-Cell Heterojunction. *Appl. Phys. Lett.* **2001**, *79* (27), 4482–4484.
- (26) Siebentritt, S.; Gütay, L.; Regesch, D.; Aida, Y.; Deprédurand, V. Why Do We Make Cu(In,Ga)Se₂ Solar Cells Non-Stoichiometric? *Sol. Energy Mater. Sol. Cells* **2013**, *119*, 18–25.
- (27) Liao, D.; Rockett, A. Cu Depletion at the CuInSe₂ Surface. *Appl. Phys. Lett.* **2003**, *82* (17), 2829–2831.

- (28) Grindle, S. P.; Smith, C. W.; Mittleman, S. D. Preparation and Properties of CuInS₂ Thin Films Produced by Exposing Sputtered Cu-In Films to an H₂S Atmosphere. *Appl. Phys. Lett.* **1979**, 35 (1), 24–26.
- (29) Chu, T. L.; Chu, S. S.; Lin, S. C.; Yue, J. Large Grain Copper Indium Diselenide Films. *J. Electrochem. Soc.* **1984**, 131 (9), 2182–2185.
- (30) Hedstrom, J.; Ohlsen, H.; Bodegard, M.; Kylner, A.; Stolt, L.; Hariskos, D.; Ruckh, M.; Schock, H. W. ZnO/CdS/Cu(In,Ga)Se₂ Thin Film Solar Cells with Improved Performance. In , *Conference Record of the Twenty Third IEEE Photovoltaic Specialists Conference*, **1993**; pp 364–371.
- (31) Kim, M. S.; Yun, J. H.; Yoon, K. H.; Ahn, B. T. Fabrication of Flexible CIGS Solar Cell on Stainless Steel Substrate by Co-Evaporation Process. *Solid State Phenom.* **2007**, 124–126, 73–76.
- (32) Kronik, L.; Cahen, D.; Schock, H. W. Effects of Sodium on Polycrystalline Cu(In,Ga)Se₂ and Its Solar Cell Performance. *Adv. Mater.* **1998**, 10 (1), 31–36.
- (33) Niles, D. W.; Al-Jassim, M.; Ramanathan, K. Direct Observation of Na and O Impurities at Grain Surfaces of CuInSe₂ Thin Films. *J. Vac. Sci. Technol. A* **1999**, 17 (1), 291–296.
- (34) Contreras, M. A.; Egaas, B.; Dippo, P.; Webb, J.; Granata, J.; Ramanathan, K.; Asher, S.; Swartzlander, A.; Noufi, R. On the Role of Na and Modifications to Cu(In,Ga)Se₂ Absorber Materials Using Thin-MF (M=Na, K, Cs) Precursor Layers *Conference Record of the Twenty-Sixth IEEE Photovoltaic Specialists Conference*, **1997**; pp 359–362.
- (35) Heske, C.; Eich, D.; Fink, R.; Umbach, E.; Kakar, S.; van Buuren, T.; Bostedt, C.; Terminello, L. J.; Grush, M. M.; Callcott, T. A.; Himpsel, F. J.; Ederer, D. L.; Perera, R. C. C.; Riedl, W.; Karg, F. Localization of Na Impurities at the Buried CdS/Cu(In,Ga)Se₂ Heterojunction. *Appl. Phys. Lett.* **1999**, 75 (14), 2082–2084.
- (36) Heske, C.; Eich, D.; Groh, U.; Fink, R.; Umbach, E.; van Buuren, T.; Bostedt, C.; Franco, N.; Terminello, L. .; Grush, M. .; Callcott, T. .; Himpsel, F. .; Ederer, D. .; Perera, R. C. .; Riedl, W.; Karg, F. Self-Limitation of Na Content at the CdS/Cu(In,Ga)Se₂ Solar Cell Heterojunction. *Thin Solid Films* **2000**, 361–362, 360–363.
- (37) Heske, C.; Richter, G.; Chen, Z.; Fink, R.; Umbach, E.; Riedl, W.; Karg, F. Influence of Na and H₂O on the Surface Properties of Cu(In,Ga)Se₂ Thin Films. *J. Appl. Phys.* **1997**, 82 (5), 2411–2420.
- (38) Heske, C.; Fink, R.; Umbach, E.; Riedl, W.; Karg, F. Na-induced Effects on the Electronic Structure and Composition of Cu(In,Ga)Se₂ Thin-film Surfaces. *Appl. Phys. Lett.* **1996**, 68 (24), 3431–3433.
- (39) Heske, C.; Eich, D.; Fink, R.; Umbach, E.; van Buuren, T.; Bostedt, C.; Kakar, S.; Terminello, L. J.; Grush, M. M.; Callcott, T. A.; Himpsel, F. J.; Ederer, D. L.; Perera, R. C. C.; Riedl, W.; Karg, F. Semi-Quantitative and Non-Destructive

- Analysis of Impurities at a Buried Interface: Na and the CdS/Cu(In,Ga)Se₂ Heterojunction. *Surf. Interface Anal.* **2000**, 30 (1), 459–463.
- (40) Ümsür, B.; Calvet, W.; Steigert, A.; Lauermann, I.; Gorgoi, M.; Prietzel, K.; Greiner, D.; Kaufmann, C. A.; Unold, T.; Lux-Steiner, M. Investigation of the Potassium Fluoride Post Deposition Treatment on the CIGSe/CdS Interface Using Hard X-Ray Photoemission Spectroscopy – a Comparative Study. *Phys. Chem. Chem. Phys.* **2016**, 18, 14129–14138.
- (41) Handick, E.; Reinhard, P.; Alsmeier, J.-H.; Köhler, L.; Pianezzi, F.; Krause, S.; Gorgoi, M.; Ikenaga, E.; Koch, N.; Wilks, R. G.; Buecheler, S.; Tiwari, A. N.; Bär, M. Potassium Postdeposition Treatment-Induced Band Gap Widening at Cu(In,Ga)Se₂ Surfaces--Reason for Performance Leap? *ACS Appl. Mater. Interfaces* **2015**, 7 (49), 27414–27420.
- (42) Jackson, P.; Hariskos, D.; Wuerz, R.; Kiowski, O.; Bauer, A.; Friedlmeier, T. M.; Powalla, M. Properties of Cu(In,Ga)Se₂ Solar Cells with New Record Efficiencies up to 21.7%. *Phys. Status Solidi RRL – Rapid Res. Lett.* **2015**, 9 (1), 28–31.
- (43) Pistor, P.; Greiner, D.; Kaufmann, C. A.; Brunken, S.; Gorgoi, M.; Steigert, A.; Calvet, W.; Lauermann, I.; Klenk, R.; Unold, T.; Lux-Steiner, M.-C. Experimental Indication for Band Gap Widening of Chalcopyrite Solar Cell Absorbers after Potassium Fluoride Treatment. *Appl. Phys. Lett.* **2014**, 105 (6), 63901.
- (44) Goto, H.; Hashimoto, Y.; Ito, K. Efficient Thin Film Solar Cell Consisting of TCO/CdS/CuInS₂/CuGaS₂ Structure. *Thin Solid Films* **2004**, 451–452, 552–555.
- (45) Green, M. A.; Emery, K.; Hishikawa, Y.; Warta, W.; Dunlop, E. D. Solar Cell Efficiency Tables (Version 47). *Prog. Photovolt. Res. Appl.* **2016**, 24 (1), 3–11.
- (46) Hariskos, D.; Powalla, M.; Chevaldonnet, N.; Lincot, D.; Schindler, A.; Dimmler, B. Chemical Bath Deposition of CdS Buffer Layer: Prospects of Increasing Materials Yield and Reducing Waste. *Thin Solid Films* **2001**, 387 (1–2), 179–181.
- (47) Melo, O. de; Hernández, L.; Zelaya-Angel, O.; Lozada-Morales, R.; Becerril, M.; Vasco, E. Low Resistivity Cubic Phase CdS Films by Chemical Bath Deposition Technique. *Appl. Phys. Lett.* **1994**, 65 (10), 1278–1280.
- (48) Pookpanratana, S.; Repins, I.; Bär, M.; Weinhardt, L.; Zhang, Y.; Félix, R.; Blum, M.; Yang, W.; Heske, C. CdS/Cu(In,Ga)Se₂ Interface Formation in High-Efficiency Thin Film Solar Cells. *Appl. Phys. Lett.* **2010**, 97 (7), 74101–74101–74103.
- (49) Heske, C.; Eich, D.; Fink, R.; Umbach, E.; van Buuren, T.; Bostedt, C.; Terminello, L. J.; Kakar, S.; Grush, M. M.; Callcott, T. A.; Himpfel, F. J.; Ederer, D. L.; Perera, R. C. C.; Riedl, W.; Karg, F. Observation of Intermixing at the Buried CdS/Cu(In,Ga)Se₂ Thin Film Solar Cell Heterojunction. *Appl. Phys. Lett.* **1999**, 74 (10), 1451–1453.
- (50) Weinhardt, L.; Bär, M.; Pookpanratana, S.; Morkel, M.; Niesen, T. P.; Karg, F.; Ramanathan, K.; Contreras, M. A.; Noufi, R.; Umbach, E.; Heske, C. Sulfur

- Gradient-Driven Se Diffusion at the CdS/CuIn(S,Se)₂ Solar Cell Interface. *Appl. Phys. Lett.* **2010**, 96 (18), 182102–182102–182103.
- (51) Weinhardt, L.; Fuchs, O.; Groß, D.; Storch, G.; Umbach, E.; Dhere, N. G.; Kadam, A. A.; Kulkarni, S. S.; Heske, C. Band Alignment at the CdS/Cu(In,Ga)S₂ Interface in Thin-Film Solar Cells. *Appl. Phys. Lett.* **2005**, 86 (6), 62109–062109–3.
 - (52) Weinhardt, L.; Fuchs, O.; Gross, D.; Storch, G.; Dhere, N. G.; Kadam, A. A.; Kulkarni, S. S.; Visbeck, S.; Niesen, T. P.; Karg, F.; Heske, C.; Umbach, E. Comparison of Band Alignments at Various CdS/Cu(In,Ga)(S,Se)₂ Inter-Faces in Thin Film Solar Cells. In *Conference Record of the 2006 IEEE 4th World Conference on Photovoltaic Energy Conversion*; 2006; Vol. 1, pp 412–415.
 - (53) Weinhardt, L.; Bär, M.; Muffler, H.-J.; Fischer, C.-H.; Lux-Steiner, M. C.; Niesen, T. P.; Karg, F.; Gleim, T.; Heske, C.; Umbach, E. Impact of Cd²⁺-Treatment on the Band Alignment at the ILGAR-ZnO/CuIn(S,Se)₂ Heterojunction. *Thin Solid Films* **2003**, 431–432, 272–276.
 - (54) Nakamura, M.; Yoneyama, N.; Horiguchi, K.; Iwata, Y.; Yamaguchi, K.; Sugimoto, H.; Kato, T. Recent R and D Progress in Solar Frontier's Small-Sized Cu(InGa)(SeS)₂ Solar Cells. In *2014 IEEE 40th Photovoltaic Specialist Conference (PVSC)*; **2014**; pp 0107–0110.
 - (55) Bernard, J. E.; Zunger, A. Electronic Structure of ZnS, ZnSe, ZnTe, and Their Pseudobinary Alloys. *Phys. Rev. B* **1987**, 36 (6), 3199–3228.
 - (56) Ashrafi, A.; Jagadish, C. Review of Zincblende ZnO: Stability of Metastable ZnO Phases. *J. Appl. Phys.* **2007**, 102 (7), 71101.
 - (57) Meyer, B. K.; Polity, A.; Farangis, B.; He, Y.; Hasselkamp, D.; Krämer, T.; Wang, C. Structural Properties and Bandgap Bowing of ZnO_{1-x}S_x Thin Films Deposited by Reactive Sputtering. *Appl. Phys. Lett.* **2004**, 85 (21), 4929–4931.
 - (58) Hariskos, D.; Menner, R.; Jackson, P.; Paetel, S.; Witte, W.; Wischmann, W.; Powalla, M.; Bürkert, L.; Kolb, T.; Oertel, M.; Dimmler, B.; Fuchs, B. New Reaction Kinetics for a High-Rate Chemical Bath Deposition of the Zn(S,O) Buffer Layer for Cu(In,Ga)Se₂-Based Solar Cells. *Prog. Photovolt. Res. Appl.* **2012**, 20 (5), 534–542.
 - (59) Weinhardt, L.; Morkel, M.; Gleim, T.; Zweigart, S.; Niesen, T. P.; Karg, F.; Heske, C.; Umbach, E. Band Alignment at the CdS/CuIn(S,Se)₂ Heterojunction in Thin Film Solar Cells. *Proc. 17th Eur. Photovolt. Sol. Energy Conf.* **2001**, 1261.
 - (60) Mezher, M.; Garris, R.; Mansfield, L. M.; Horsley, K.; Weinhardt, L.; Duncan, D. A.; Blum, M.; Rosenberg, S. G.; Bär, M.; Ramanathan, K.; Heske, C. Electronic Structure of the Zn(O,S)/Cu(In,Ga)Se₂ Thin-Film Solar Cell Interface. *Prog. Photovolt. Res. Appl.* **2016**, In Print.
 - (61) Rothwarf, A. CuInSe₂/Cd(Zn)S Solar Cell Modeling and Analysis. *Sol. Cells* **1986**, 16, 567–590.
 - (62) Swank, RK. Surface Properties of II-VI Compounds Phys. **1967**; Rev. 153, 844.

- (63) Romeo, N. Solar Cells Made by Chalcopyrite Materials. *Jpn. J. Appl. Phys.* **1980**, 19 (S3), 5.
- (64) Turowski, M.; Kelly, M. K.; Margaritondo, G.; Tomlinson, R. D. Direct Confirmation of the Conduction-band Lineup in the CuInSe₂-CdS Heterojunction Solar Cell. *Appl. Phys. Lett.* **1984**, 44 (8), 768–770.
- (65) Turowski, M.; Margaritondo, G.; Kelly, M. K.; Tomlinson, R. D. Photoemission Studies of CuInSe₂ and CuGaSe₂ and of their Interfaces with Si and Ge. *Phys. Rev. B* **1985**, 31 (2), 1022–1027.
- (66) Nelson, A. J.; Gebhard, S.; Rockett, A.; Colavita, E.; Engelhardt, M.; Höchst, H. Synchrotron-Radiation Photoemission Study of CdS/CuInSe₂ Heterojunction Formation. *Phys. Rev. B* **1990**, 42 (12), 7518–7523.
- (67) Löher, T.; Jaegermann W.; Pettenkofer.; Formation and Electronic Properties of the CdS/CuInSe₂ (011) Heterointerface studied by Synchrotron-induced Photoemission. *J. Appl. Phys.* **1995**, 77, 731.
- (68) Liu, X.; Sites, J. R. Calculated Effect of Conduction-band Offset on CuInSe₂ Solar-cell Performance. *AIP Conference Proceedings*; **1996**; Vol. 353, pp 444–452.
- (69) Wei, S.-H.; Zunger, A. Band Offsets at the CdS/CuInSe₂ Heterojunction. *Appl. Phys. Lett.* **1993**, 63 (18), 2549–2551.
- (70) Niemegeers, A.; Burgelman, M.; Vos, A. D. On the CdS/CuInSe₂ Conduction Band Discontinuity. *Appl. Phys. Lett.* **1995**, 67 (6), 843–845.
- (71) Niemegeers, A.; Burgelman, M.; Herberholz, R.; Rau, U.; Hariskos, D.; Schock, H.-W. Model for Electronic Transport in Cu(In,Ga)Se₂ Solar Cells. *Prog. Photovolt. Res. Appl.* **1998**, 6 (6), 407–421.
- (72) Ellmer, K.; Klein, A.; Rech, B. *Transparent Conductive Zinc Oxide: Basics and Applications in Thin Film Solar Cells*; Springer Science & Business Media, **2007**.
- (73) Scheer, R.; Messmann-Vera, L.; Klenk, R.; Schock, H.-W. On the Role of Non-Doped ZnO in CIGSe Solar Cells. *Prog. Photovolt. Res. Appl.* **2012**, 20 (6), 619–624.
- (74) Jiang, M.; Tang, K.; Yan, X. Characterization of Intrinsic ZnO Thin Film Deposited by Sputtering and Its Effects on CuIn_{1-x}Ga_xSe₂ Solar Cells. *J. Photonics Energy* **2012**, 2 (1), 028502–1.
- (75) Shafarman, W. N.; Stolt, L. Cu(InGa)Se₂ Solar Cells. In *Handbook of Photovoltaic Science and Engineering*; Luque, A., Hegedus, S., Eds.; John Wiley & Sons, Ltd, **2003**; pp 567–616.
- (76) A new world record for solar cell efficiency <http://phys.org/news/2013-01-world-solar-cell-efficiency.html> (accessed May 10, 2016).
- (77) Hüfner, S. *Photoelectron Spectroscopy - Principles and Applications*; Springer Science & Business Media, **2013**.
- (78) Briggs, D.; Seah, M. P. *Practical Surface Analysis, Auger and X-Ray Photoelectron Spectroscopy*; Wiley, **1990**.

- (79) Feibelman, P. J.; Eastman, D. E. Photoemission spectroscopy—Correspondence between Quantum Theory and Experimental Phenomenology. *Phys. Rev. B* **1974**, *10* (12), 4932–4947.
- (80) Seah, M. P. Summary of ISO/TC 201 Standard: VII ISO 15472 : 2001—surface Chemical Analysis—x-Ray Photoelectron Spectrometers—calibration of Energy Scales. *Surf. Interface Anal.* **2001**, *31* (8), 721–723.
- (81) Denninger, G.; Dose, V.; Scheidt, H. A VUV Isochromat Spectrometer for Surface Analysis. *Appl. Phys.* **1979**, *18* (4), 375–380.
- (82) Gleim, T.; Heske, C.; Umbach, E.; Schumacher, C.; Gundel, S.; Faschinger, W.; Fleszar, A.; Ammon, C.; Probst, M.; Steinrück, H.-P. Formation of the ZnSe/(Te)/GaAs(1 0 0) Heterojunction. *Surf. Sci.* **2003**, *531* (1), 77–85.
- (83) Weinhardt, L.; Heske, C.; Umbach, E.; Niesen, T. P.; Visbeck, S.; Karg, F. Band Alignment at the I-ZnO/CdS Interface in Cu(In,Ga)(S,Se)₂ Thin-Film Solar Cells. *Appl. Phys. Lett.* **2004**, *84* (16), 3175–3177.
- (84) Bär, M.; Ennaoui, A.; Klaer, J.; Sáez-Araoz, R.; Kropp, T.; Weinhardt, L.; Heske, C.; Schock, H.-W.; Fischer, C.-H.; Lux-Steiner, M. C. The Electronic Structure of the [Zn(S,O)/ZnS]/CuInS₂ Heterointerface – Impact of Post-Annealing. *Chem. Phys. Lett.* **2006**, *433* (1–3), 71–74.
- (85) Bär, M.; Repins, I.; Contreras, M. A.; Weinhardt, L.; Noufi, R.; Heske, C. Chemical and Electronic Surface Structure of 20%-Efficient Cu(In,Ga)Se₂ Thin Film Solar Cell Absorbers. *Appl. Phys. Lett.* **2009**, *95* (5), 52106–052106–3.
- (86) Horsley, K.; Pookpanratana, S.; Krause, S.; Hofmann, T.; Blum, M.; Weinhardt, L.; Bar, M.; George, K.; Van Duren, J.; Jackrel, D.; Heske, C. Electronic and Chemical Properties of Non-Vacuum Deposited Chalcopyrite Solar Cells; IEEE, **2011**; pp 000374–000378.
- (87) Caroli, C.; Lederer-Rozenblatt, D.; Roulet, B.; Saint-James, D. Inelastic Effects in Photoemission: Microscopic Formulation and Qualitative Discussion. *Phys. Rev. B* **1973**, *8* (10), 4552–4569.
- (88) Seah, M. P.; Dench, W. A. Quantitative Electron Spectroscopy of Surfaces: A Standard Data Base for Electron Inelastic Mean Free Paths in Solids. *Surf. Interface Anal.* **1979**, *1* (1), 2–11.
- (89) Seah, M. P. An Accurate and Simple Universal Curve for the Energy-Dependent Electron Inelastic Mean Free Path. *Surf. Interface Anal.* **2012**, *44* (4), 497–503.
- (90) Wojdyr, M. Fityk: A General-Purpose Peak Fitting Program. *J. Appl. Crystallogr.* **2010**, *43* (5–1), 1126–1128.
- (91) Repoux, M. Comparison of Background Removal Methods for XPS. *Surf. Interface Anal.* **1992**, *18* (7), 567–570.
- (92) Shirley, D.A.; High-Resolution X-Ray Photoemission Spectrum of the Valence Bands of Gold. *Phys. Rev. B*; **1972**; *5*, 4709.

- (93) Doniach, S.; Šunjić, M. Many-Electron Singularity in X-Ray Photoemission and X-Ray Line Spectra from Metals. *J. Phys. C Solid State Phys.* **1970**, 3 (2), 285.
- (94) Weinhardt, L.; Fuchs, O.; Batchelor, D.; Bär, M.; Blum, M.; Denlinger, J. D.; Yang, W.; Schöll, A.; Reinert, F.; Umbach, E.; Heske, C. Electron-Hole Correlation Effects in Core-Level Spectroscopy Probed by the Resonant Inelastic Soft X-Ray
- (95) CXRO X-Ray Interactions With Matter http://henke.lbl.gov/optical_constants/
- (96) Attwood, David. Soft X-Rays and Extreme Ultraviolet Radiation: Principles and Applications. Cambridge University Press, **2013**.
- (97) *Comparison of Auger Yield and Fluorescence Yield as a Function of Atomic Number.*; 2007
https://commons.wikimedia.org/wiki/File:Auger_xray_wiki_in_png_format.png
(accessed Apr 18, 2016)
- (98) Salem, S. I.; Panossian, S. L.; Krause, R. A. Experimental K and L Relative X-Ray Emission Ratess. *At. Data Nucl. Data Tables* **1974**, 14 (2), 91–109.
- (99) Beamline 8.0.1 <https://www-als.lbl.gov/index.php/ring-leaders/115-801.html>
(accessed Apr 11, 2016).
- (100) Perera, R. C. C.; Shuh, D. K.; Hudson, E. A.; Yurkas, J.; Callcott, T. A.; Jia, J.; Ellis, A. W.; Himpfel, F. J.; Carlisle, J. A.; Ederer, D. L.; Stohr, J.; Samant, M. G.; Terminello, L. J. First Experimental Results from the IBM/Penn/Tulane/LBL Undulator Beamline at the ALS. *Rev. Sci. Instrum.* **1995**, 66 (2), 1394.
- (101) Blum, M.; Weinhardt, L.; Fuchs, O.; Bär, M.; Zhang, Y.; Weigand, M.; Krause, S.; Pookpanratana, S.; Hofmann, T.; Yang, W.; Denlinger, J. D.; Umbach, E.; Heske, C. Solid and Liquid Spectroscopic Analysis (SALSA)--a Soft X-Ray Spectroscopy Endstation with a Novel Flow-through Liquid Cell. *Rev. Sci. Instrum.* **2009**, 80 (12), 123102.
- (102) Fuchs, O.; Weinhardt, L.; Blum, M.; Weigand, M.; Umbach, E.; Bär, M.; Heske, C.; Denlinger, J.; Chuang, Y.-D.; McKinney, W.; Hussain, Z.; Gullikson, E.; Jones, M.; Batson, P.; Nelles, B.; Follath, R. High-Resolution, High-Transmission Soft X-Ray Spectrometer for the Study of Biological Samples. *Rev. Sci. Instrum.* **2009**, 80.
- (103) Green, M. A.; Emery, K.; Hishikawa, Y.; Warta, W. Solar Cell Efficiency Tables (Version 33). *Prog. Photovolt. Res. Appl.* **2009**, 17 (1), 85–94.
- (104) ZSW sets 21.7% CIGS cell record | PV-Tech http://www.pv-tech.org/news/zsw_sets_21.7_cigs_cell_record (accessed Feb 4, 2015).
- (105) Global Solar Energy - <http://www.globalsolar.com/company/technology> (accessed Mar 7, 2016).
- (106) Stion - <http://www.stion.com/technology/gen-1/> (accessed Mar 7, 2016).
- (107) MiaSolé - <http://miasole.com/products/>.
- (108) Weinhardt, L.; Fuchs, O.; Fleszar, A.; Bär, M.; Blum, M.; Weigand, M.; Denlinger, J. D.; Yang, W.; Hanke, W.; Umbach, E.; Heske, C. Resonant Inelastic Soft X-Ray

- Scattering of CdS: A Two-Dimensional Electronic Structure Map Approach. *Phys. Rev. B* **2009**, 79 (16), 165305.
- (109) Gleim, T.; Heske, C.; Umbach, E.; Schumacher, C.; Faschinger, W.; Ammon, C.; Probst, M.; Steinrück, H.-P. Reduction of the ZnSe/GaAs(100) Valence Band Offset by a Te Interlayer. *Appl. Phys. Lett.* **2001**, 78 (13), 1867–1869.
- (110) Schmid, D.; Ruckh, M.; Schock, H. W. Photoemission Studies on Cu(In, Ga)Se₂ Thin Films and Related Binary Selenides. *Appl. Surf. Sci.* **1996**, 103 (4), 409–429.
- (111) Moulder, J. F. *Handbook of X-Ray Photoelectron Spectroscopy: A Reference Book of Standard Spectra for Identification and Interpretation of XPS Data*; Physical Electronics Division, Perkin-Elmer Corporation, **1992**.
- (112) NIST X-ray Photoelectron Spectroscopy (XPS) Database Main Search Menu http://srdata.nist.gov/xps/main_search_menu.aspx (accessed Jan 13, 2016).
- (113) Gebhardt, R. K.; Sloboshanin, S.; Schaefer, J. A.; Chassé, T. Arsenic Interlayers at the Sn/InP(001) Interface. *Appl. Surf. Sci.* **1999**, 142 (1–4), 94–98.
- (114) Cherkashinin, G.; Krischok, S.; Himmerlich, M.; Ambacher, O.; Schaefer, J. A. Electronic Properties of C 60 /InP(001) Heterostructures. *J. Phys. Condens. Matter* **2006**, 18 (43), 9841.
- (115) Beach, R. A.; Piquette, E. C.; McGill, T. C. XPS Study of Oxygen Adsorption on (3x3) Reconstructed MBE Grown GaN Surfaces. *MRS Internet J. Nitride Semicond. Res.* **1999**, 4 (S1), Art. No. G6.26.
- (116) Moretti, G. Auger Parameter and Wagner Plot in the Characterization of Chemical States by X-Ray Photoelectron Spectroscopy: A Review. *J. Electron Spectrosc. Relat. Phenom.* **1998**, 95 (2–3), 95–144.
- (117) Mansfield, L. M.; Noufi, R.; Muzzillo, C. P.; DeHart, C.; Bowers, K.; To, B.; Pankow, J. W.; Reedy, R. C.; Ramanathan, K. Enhanced Performance in Cu(In,Ga)Se Solar Cells Fabricated by the Two-Step Selenization Process With a Potassium Fluoride Postdeposition Treatment. *IEEE J. Photovolt.* **2014**, 4 (6), 1650–1654.
- (118) Muzzillo, C. P.; Mansfield, L. M.; Ramanathan, K.; Anderson, T. J. Properties of Cu_{1-x}K_xInSe₂ Alloys. *J. Mater. Sci.* **2016**, 51 (14), 6812–6823.
- (119) Ishizuka, S.; Yamada, A.; Fons, P. J.; Shibata, H.; Niki, S. Interfacial Alkali Diffusion Control in Chalcopyrite Thin-Film Solar Cells. *ACS Appl. Mater. Interfaces* **2014**, 6 (16), 14123–14130.
- (120) Salomé, P. M. P.; Rodriguez-Alvarez, H.; Sadewasser, S. Incorporation of Alkali Metals in Chalcogenide Solar Cells. *Sol. Energy Mater. Sol. Cells* **2015**, 143, 9–20.
- (121) Theelen, M.; Hans, V.; Barreau, N.; Steijvers, H.; Vroon, Z.; Zeman, M. The Impact of Alkali Elements on the Degradation of CIGS Solar Cells. *Prog. Photovolt. Res. Appl.* **2015**, 23 (5), 537–545.

- (122) Yoon, J.-H.; Seong, T.-Y.; Jeong, J. Effect of a Mo Back Contact on Na Diffusion in CIGS Thin Film Solar Cells. *Prog. Photovolt. Res. Appl.* **2013**, *21* (1), 58–63.
- (123) Zellner, M. B.; Birkmire, R. W.; Eser, E.; Shafarman, W. N.; Chen, J. G. Determination of Activation Barriers for the Diffusion of Sodium through CIGS Thin-Film Solar Cells. *Prog. Photovolt. Res. Appl.* **2003**, *11* (8), 543–548.
- (124) Scofield, J. H.; Asher, S.; Albin, D.; Tuttle, J.; Contreras, M.; Niles, D.; Reedy, R.; Tennant, A.; Noufi, R. Sodium Diffusion, Selenization, and Microstructural Effects Associated with Various Molybdenum Back Contact Layers for CIS-Based Solar Cells. **1994**; *IEEE First World Conference on Photovoltaic Energy Conversion*, Vol. 1, pp 164–167.
- (125) Schmid, D.; Ruckh, M.; Grunwald, F.; Schock, H. W. Chalcopyrite/defect Chalcopyrite Heterojunctions on the Basis of CuInSe₂. *J. Appl. Phys.* **1993**, *73* (6), 2902–2909.
- (126) Hamilton, J. P.; Hrdina, K. E. Diffusion Barriers for Photovoltaic Devices by Leaching. Patent WO2013082343 A1, June 6, 2013.
- (127) Herz, K.; Eicke, A.; Kessler, F.; Wächter, R.; Powalla, M. Diffusion Barriers for CIGS Solar Cells on Metallic Substrates. *Thin Solid Films* **2003**, *431–432*, 392–397.
- (128) Weinhardt, L.; Fuchs, O.; Groß, D.; Umbach, E.; Heske, C.; Dhere, N. G.; Kadam, A. A.; Kulkarni, S. S. Surface Modifications of Cu(In,Ga)S₂ Thin Film Solar Cell Absorbers by KCN and H₂O₂/H₂SO₄ Treatments. *J. Appl. Phys.* **2006**, *100* (2), 24907-024907–4.
- (129) Brown, M. A.; Faubel, M.; Winter, B. X-Ray Photo- and Resonant Auger-Electron Spectroscopy Studies of Liquid Water and Aqueous Solutions. *Annu. Rep. Sect. C Phys. Chem.* **2009**, *105*, 174.
- (130) ZSW raises efficiency of cadmium-free CIGS solar cells to record 21% http://www.semiconductor-today.com/news_items/2015/feb/zsw_250215.shtml (accessed Apr 15, 2015).
- (131) Contreras, M. A.; Nakada, T.; Hongo, M.; Pudov, A. O.; Sites, J. R. ZnO/ZnS(O,OH)/Cu(In,Ga)Se₂/Mo Solar Cell with 18.6% Efficiency. In *Proceedings of 3rd World Conference on Photovoltaic Energy Conversion, 2003*; **2003**; Vol. 1, p 570–573 Vol.1.
- (132) Klenk, R.; Steigert, A.; Rissom, T.; Greiner, D.; Kaufmann, C. A.; Unold, T.; Lux-Steiner, M. C. Junction Formation by Zn(O,S) Sputtering Yields CIGSe-Based Cells with Efficiencies Exceeding 18%. *Prog. Photovolt. Res. Appl.* **2014**, *22* (2), 161–165.
- (133) Grimm, A.; Just, J.; Kieven, D.; Lauermann, I.; Palm, J.; Neisser, A.; Rissom, T.; Klenk, R. Sputtered Zn(O,S) for Junction Formation in Chalcopyrite-Based Thin Film Solar Cells. *Phys. Status Solidi RRL – Rapid Res. Lett.* **2010**, *4* (5–6), 109–111.

- (134) Kieven, D.; Grimm, A.; Lauermann, I.; Lux-Steiner, M. C.; Palm, J.; Niesen, T.; Klenk, R. Band Alignment at Sputtered $\text{ZnS}_x\text{O}_{1-x}/\text{Cu}(\text{In,Ga})(\text{Se,S})_2$ Heterojunctions. *Phys. Status Solidi RRL – Rapid Res. Lett.* **2012**, 6 (7), 294–296.
- (135) Pankow, J. W.; Steirer, K. X.; Mansfield, L. M.; Garriss, R. L.; Ramanathan, K.; Teeter, G. R. Band Alignment of CBD Deposited $\text{Zn}(\text{O,S})/\text{Cu}(\text{In}_{1-x}\text{Ga}_x)\text{Se}_2$ Interface. *Photovoltaic Specialist Conference (PVSC), 2014 IEEE 40th*; **2014**; pp 1670–1673.
- (136) Terada, N.; Widodo, R. T.; Itoh, K.; Kong, S. H.; Kashiwabara, H.; Okuda, T.; Obara, K.; Niki, S.; Sakurai, K.; Yamada, A.; Ishizuka, S. Characterization of Interface Nature and Band Alignment in CBD- $\text{CdS}/\text{Cu}(\text{In,Ga})\text{Se}_2$ Bi-Layer Structure by Photoemission and Inverse Photoemission Spectroscopy. *Thin Solid Films* **2005**, 480–481, 183–187.
- (137) Hervé, P.; Vandamme, L. K. J. General Relation between Refractive Index and Energy Gap in Semiconductors. *Infrared Phys. Technol.* **1994**, 35 (4), 609–615.
- (138) Srikant, V.; Clarke, D. R. On the Optical Band Gap of Zinc Oxide. *J. Appl. Phys.* **1998**, 83 (10), 5447–5451.
- (139) Eicke, A.; Ciba, T.; Hariskos, D.; Menner, R.; Tschamber, C.; Witte, W. Depth Profiling with SNMS and SIMS of $\text{Zn}(\text{O,S})$ Buffer Layers for $\text{Cu}(\text{In,Ga})\text{Se}_2$ Thin-Film Solar Cells. *Surf. Interface Anal.* **2013**, 45 (13), 1811–1820.
- (140) Platzer-Björkman, C.; Törndahl, T.; Abou-Ras, D.; Malmström, J.; Kessler, J.; Stolt, L. $\text{Zn}(\text{O,S})$ Buffer Layers by Atomic Layer Deposition in $\text{Cu}(\text{In,Ga})\text{Se}_2$ Based Thin Film Solar Cells: Band Alignment and Sulfur Gradient. *J. Appl. Phys.* **2006**, 100 (4), 044506–044509.
- (141) Ramanathan, K.; Mann, J.; Glynn, S.; Christensen, S.; Pankow, J.; Li, J.; Scharf, J.; Mansfield, L.; Contreras, M.; Noufi, R. A Comparative Study of $\text{Zn}(\text{O,S})$ Buffer Layers and CIGS Solar Cells Fabricated by CBD, ALD, and Sputtering. In *2012 38th IEEE Photovoltaic Specialists Conference (PVSC)*; **2012**; pp 001677–001681.
- (142) Duchoslav, J.; Steinberger, R.; Arndt, M.; Stifter, D. XPS Study of Zinc Hydroxide as a Potential Corrosion Product of Zinc: Rapid X-Ray Induced Conversion into Zinc Oxide. *Corros. Sci.* **2014**, 82, 356–361.
- (143) Reichardt, J.; Bär, M.; Grimm, A.; Kötschau, I.; Lauermann, I.; Sokoll, S.; Lux-Steiner, M. C.; Fischer, C.-H.; Heske, C.; Weinhardt, L.; Fuchs, O.; Jung, C.; Gudat, W.; Niesen, T. P.; Karg, F. Inducing and Monitoring Photoelectrochemical Reactions at Surfaces and Buried Interfaces in $\text{Cu}(\text{In,Ga})(\text{S,Se})_2$ Thin-Film Solar Cells. *Appl. Phys. Lett.* **2005**, 86 (17), 172102–172102–172103.
- (144) Deroubaix, G.; Marcus, P. X-Ray Photoelectron Spectroscopy Analysis of Copper and Zinc Oxides and Sulphides. *Surf. Interface Anal.* **1992**, 18 (1), 39–46.

- (145) Friedlmeier, T. M.; Jackson, P.; Bauer, A.; Hariskos, D.; Kiowski, O.; Wuerz, R.; Powalla, M. Improved Photocurrent in Cu(In,Ga)Se₂ Solar Cells: From 20.8% to 21.7%. *IEEE J. Photovolt.* **2015**, 5 (5), 1487–1491.
- (146) Heske, C. Spectroscopic Investigation of Buried Interfaces and Liquids with Soft X-Rays. *Appl. Phys. Mater. Sci. Process.* **2004**, 78 (6), 829–835.
- (147) Bär, M.; Ennaoui, A.; Klaer, J.; Kropp, T.; Sáez-Araoz, R.; Lehmann, S.; Grimm, A.; Lauermann, I.; Loreck, C.; Sokoll, S.; Schock, H.-W.; Fischer, C.-H.; Lux-Steiner, M. C.; Jung, C. Intermixing at the Heterointerface between ZnS/Zn(S,O) Bilayer Buffer and CuInS₂ Thin Film Solar Cell Absorber. *J. Appl. Phys.* **2006**, 100 (6), 64911.
- (148) QUASES-IMFP-TPP2M program based on: Tanuma, S.; Powell, C.J.; Penn, D.R. Calculations of Electron Inelastic Mean Free Paths. V. Data for 14 Organic Compounds Over the 50-2000 eV range. *Surf. Interface Anal.* **1994**, 21, 165-176.
- (149) Scofield, J. H. Hartree-Slater Subshell Photoionization Cross-Sections at 1254 and 1487 eV. *J. Electron Spectrosc. Relat. Phenom.* **1976**, 8 (2), 129–137.
- (150) Yeh, J. J.; Lindau, I. Atomic Subshell Photoionization Cross Sections and Asymmetry Parameters: $1 \leq Z \leq 103$. *At. Data Nucl. Data Tables* **1985**, 32 (1), 1–155.
- (151) Duncan, D. A.; Kephart, J. M.; Horsley, K.; Blum, M.; Mezher, M.; Weinhardt, L.; Häming, M.; Wilks, R. G.; Hofmann, T.; Yang, W.; Bär, M.; Sampath, W. S.; Heske, C. Characterization of Sulfur Bonding in CdS:O Buffer Layers for CdTe-Based Thin-Film Solar Cells. *ACS Appl. Mater. Interfaces* **2015**, 7 (30), 16382–16386.

CURRICULUM VITAE

Graduate College
University of Nevada, Las Vegas

Michelle Mezher
Degree:
Bachelor of Arts, Chemistry, 2012
University of San Diego

Special Honors and Awards:

1. **Mountain Mines Scholarship**, award from UNLV Department of Chemistry and Biochemistry, 2015-2016
2. **Nowak Notre Dame Scholarship**, award from UNLV Department of Chemistry and Biochemistry, 2015-2016
3. **Hands On Photovoltaics Experience (HOPE)** – National Renewable Energy Lab – 2014 (participant)
4. **QUANTSOL International Summer School on Photovoltaics and New Concepts of Quantum Solar Energy Conversion** – Helmholtz-Zentrum Berlin für Materialien und Energie, Hirschegg, Austria, 2013 (participant)
5. **UNLV Middle Eastern Scholarship**, Fall 2013
6. **DAAD RISE Professional Scholarship** (Deutscher Akademischer Austausch Dienst (German Academic Exchange Service) Research Internships in Science and Engineering) Helmholtz-Zentrum Berlin für Materialien und Energie, 2013
7. **American Chemical Society- Division of Colloid and Surface Chemistry- Student Poster Award 1st Place**, Spring Conference San Diego, 2012
8. **SURE (Summer Undergraduate Research Experience) Award**, University of San Diego, 2011
9. **Circle of Excellence Scholar**, award from University of San Diego, 2008-2012
10. **Provost Scholar**, award from University of San Diego, 2008-2012
11. **Academic Competiveness Award**, award from University of San Diego, 2008-2012

Publications:

1. **M. Mezher**, R. Garris, L. M. Mansfield, D. Hauschild, M. Blum, K. Horsley, D. A. Duncan, W. Yang, M. Bär, L. Weinhardt, K. Ramanathan, and C. Heske, "Soft x-ray spectroscopy of a complex heterojunction in high-efficiency thin-film photovoltaics: intermixing and Zn speciation at the Zn(O,S)/CIGSe interface" Submitted to ACS Appl. Mater. Interfaces.
2. D.A. Duncan, R. Mendelsberg, **M. Mezher**, K. Horsley, S. G. Rosenberg, M. Blum, G. Xiong, L. Weinhardt, M. Gloeckler, and C. Heske, "A New Look at the Electronic Structure of Transparent Conductive Oxides – A Case Study of the Interface between Zinc Magnesium Oxide and Cadmium Telluride" Submitted to Advanced Materials Interfaces.
3. **M. Mezher**, R. Garris, L.M. Mansfield, K. Horsley, L. Weinhardt, D.A. Duncan, M. Blum, S.G. Rosenberg, M. Bär, Kannan Ramanathan, and Clemens Heske, "Electronic Structure of the Zn(O,S)/Cu(In,Ga)Se₂ Thin-Film Solar Cell Interface" Progress in Photovoltaics: Research and Applications In Print, 2016.
4. D.A. Duncan, J.M. Kephart, K. Horsley, M. Blum, **M. Mezher**, L. Weinhardt, M. Häming, R.G. Wilks, T. Hofmann, W. Yang, M. Bär, W.S. Sampath, and C. Heske, "Characterization of sulfur bonding in CdS:O buffer layers for CdTe-based thin-film solar cells" ACS Appl Mater Interfaces **7**, 16382-6 (2015)
5. L. Benz, A. Park, J. R. Corey, **M. P. Mezher**, V. C. Park, "A fundamental investigation of the interaction of petroleum-relevant organosulfur compounds with TiO₂(110)", Langmuir, 128, 10209, 2012.

Oral Presentations (presenter indicated with*):

1. **M. Mezher***, M. Blum, M. Bär, L. Weinhardt, R.G. Wilks, M. Häming, S.G. Rosenberg, W. Yang, R. Garris, L. Mansfield, K. Ramanathan, and C. Heske, "Chemical and Electronic Structure of the Zn(O,S)/Cu(In,Ga)Se₂ Interface" Materials Research Society Spring Meeting, San Francisco, CA 2015.
2. S G. Rosenberg*, **M. Mezher**, K. Horsley, D.A. Hanks, M. Blum, M. Baer, W. Yang, R. Wilks, D. Kreikemeyer-Lorenzo, L. Weinhardt, J. Lee, W. Shafarman, R. Birkmire, K. Ramanathan, and C. Heske, "Chemical Structure and Electronic Level Alignment at the (Ag,Cu)(In,Ga)Se₂/Mo Thin-Film Solar Cell Interface" Materials Research Society Spring Meeting, San Francisco, CA 2015.

3. **M. Mezher***, M. Blum, K. Horsley, D. Hanks, M. Weir, T. Hofmann, M. Bär, L. Weinhardt, and C. Heske, "Chemical and Electronic Structure of In-Terminated Cu(In,Ga)Se₂ Thin Film Surfaces" Materials Research Society Spring Meeting, San Francisco, CA 2013.

Poster Presentations:

1. **M. Mezher***, K. Horsley*, R. Garris, L.M. Mansfield, M. Blum, D.A. Duncan, W. Yang, M. Bar, L. Weinhardt, R. Wieting, K. Ramanathan, C. Heske, "Chemical and Electronic Analysis of Cu(In,Ga)Se₂ Thin-Film Photovoltaic Materials" DOE SunShot Thin-Film Workshop, Denver, CO, August 2015
2. **M. Mezher*** K. Horsley, R. Garris, L.M. Mansfield, M. Blum, D.A. Duncan, W. Yang, M. Bar, L. Weinhardt, R. Wieting, K. Ramanathan, C. Heske, "Chemical and Electronic Analysis of Cu(In,Ga)Se₂ Thin-Film Photovoltaic Materials", Hands on Photovoltaic Experience (HOPE), Denver, CO, July 2014.
3. K. Horsley*, **M. Mezher**, D. Hanks, M. G. Weir, T. Hofmann, W. Yang, R. G. Wilks, M. Haeming, M. Blum, M. Baer, L. Weinhardt, K. Ramanathan, M. Contreras, R. Noufi, C. Heske, "Surface Spectroscopy for Chemical and Electronic Analysis of Thin-film Photovoltaic Materials", Presented at the 2nd DOE Thin-Film Workshop Poster Session at NREL, Golden CO, October 2013.
4. A. Park*, **M. Mezher***, and L. Benz, "A fundamental investigation of the interaction of petroleum-relevant organosulfur compounds with TiO₂(110)" American Chemical Society- Division of Colloid and Surface Chemistry, Spring 2012.
5. **M. Mezher*** and D. Devine, "Correlation of Variation of Brightness to the Formation of Planetary Disks" Creative Collaborations, University of San Diego, Spring 2011

Dissertation Title:

Novel Pathways to High-Efficiency Chalcopyrite Photovoltaic Devices:
A Spectroscopic Investigation of Alternative Buffer Layers and Alkali-Treated Absorbers

Dissertation Examination Committee:

Chairperson, Clemens Heske, Dr. rer. nat.
Committee Member, David Hatchett, Ph. D.
Committee Member, Kathy Robins, Ph. D.
Graduate Faculty Representative, Shubhra Bansal, Ph. D.